MEASURING LATERAL GROUND MOVEMENT WITH SYNTHETIC APERTURE RADAR DIFFERENTIAL INTERFEROMETRY: TECHNIQUE AND VALIDATION

SHILADITYA SIRCAR

NOTE TO USERS

Measuring Lateral Ground Movement With Synthetic Aperture Radar Differential Interferometry: Technique and Validation

By

© **Shiladitya Sircar**, B.Eng

A thesis submitted to the School of Graduate Studies

in partial fulfillment of the requirements for the degree of

Master of Engineering

Faculty of Engineering and Applied Science
Department of Electrical and Computer Engineering
Memorial University of Newfoundland

August 2004

St. John's Newfoundland Canada

Your file Votre référence
ISBN: 0-494-02377-5
Our file Notre référence
ISBN: 0-494-02377-5

Abstract

Research under the framework of natural hazards monitoring with Interferometric Synthetic Aperture Radar (InSAR) has gained eminence in the last 10 years with advances in satellite imaging systems. Ground movement is known to be a form of natural hazard, which threatens the integrity of buried infrastructure as either massive instantaneous movement or visually imperceptible, slow incremental movement over a long period. Both types of movement can lead to serious damage. InSAR techniques have been well investigated for measuring ground subsidence, the vertical component of ground movement. If it is incorrectly assumed that the lateral movement component is zero, subsidence movement derived from one satellite look direction will contain errors. The research presented here has resulted in the derivation of a technique by which both vertical and lateral ground movement components can be estimated. Adopting the suggested technique for routine InSAR analysis in certain instances will provide the ability to derive more accurate subsidence estimates compared to the standard single look technique.

Acknowledgements

With a deep sense of gratitude, I wish to express my sincere thanks to my supervisors, Mr. Desmond Power, Dr. Charles Randell and Dr. Eric Gill for their help. It is through immense patience, understanding and encouragement that this work stands complete. I would also especially like to convey my sincere gratitude to Mr. Desmond Power, my thesis supervisor, whose guidance for this work requires no elaboration. His company and assurance at the time of crisis will be remembered. His valuable suggestions as final words during the course of work are greatly appreciated.

I am deeply indebted and grateful to National Research Council of Canada (NSERC) for funding my graduate work (through grants to Dr. Randell and Dr. Gill) and for the facilities at C-CORE that were available during the course of this research. I would like to express my gratitude to the remote sensing team at C-CORE, especially to Dr. James Youden for his suggestions during the course of this work.

Finally, I owe it to my dear family for their support, patience, encouragement and blessing when I am thousands of miles away from them.

Table of Contents

List of Figures

Chapter 1

Chapter 2

Chapter 3

Chapter 4

Appendix A

List of Tables

Nomenclature

Acronyms	Definitions
SAR	Synthetic Aperture Radar
LOS	Line of Sight
InSAR	Interferometric SAR
DInSAR	Differential Interferometric SAR
GPS	Global Positioning System
SLC	Single Look Complex
DEM	Digital Elevation Model
Pixel	Picture Element

Variables	Definitions
r	Distance between the sensor and the target
r_0	Distance between the sensor and the target (the initial position)
l_{sa}	The radar scan range on ground (synthetic aperture)
λ	Wavelength of the system C-Band = 5.6 cm
L	Antenna length
v_0	Constant velocity of the SAR antenna
δ_{az}	Spatial resolution in the azimuthal direction
$\varphi(x)$	Received echoes resulting after a distance r
$\varphi(t)$	Time independent phase term
k	Propagation constant
t_{max}	The illumination time of a point target
θ_{sa}	The change in look angle due to length l_{sa}
B_{az}	Bandwidth of the signal in azimuth
$Z(x,y)$	SAR pixel
$I(x,y)$	The intensity of the pixel
α_{ra}	Angular resolution
B	Orbit baseline
R_1	Sensor to target distance
R_2	Sensor to target distance (at another time or separated by baseline)
S_1	Sensor (receive antenna)
S_2	Sensor (transmit antenna)
δ_h	Horizontal separation from reference path
δ_v	Vertical separation from reference path

Z_{int}	Interferogram pixel
ρ	Slant range
$\Delta\rho$	Slant Range Change (SRC)
B_h	Horizontal baseline
Z_a	Altitude of a point on ground
γ	Coherence of two SAR Images
$\gamma_{temporal}$	Temporal decorrelation coefficient
$\gamma_{spatial}$	Spatial decorrelation coefficient
σ_z	Error in elevation estimates
B_{cr}	Critical baseline
$\vec{D}$	Descending pass SRC vector (A pixel from differential interferogram obtained from descending pass)
$\vec{A}$	Ascending pass SRC Vector (A pixel from differential interferogram obtained from ascending pass)
$\vec{B}$	Actual movement of ground Real ground movement vector representation
θ_d	Satellite look angle descending pass
θ_a	Satellite look angle ascending pass
φ_d	Satellite trajectory inclination of descending pass with geographic North-South
φ_a	Satellite trajectory inclination of ascending pass with geographic North-South
ΔY	Measured East-West movement
ΔX	Measured North-South movement
ΔZ	Measured subsidence movement
ρ_d	Slant Range Change SRC descending
ρ_a	Slant Range Change (SRC) ascending

Chapter 1

Introduction

The financial and communal impact of a catastrophe instantiated by geophysical activity is significant. Landslides, subsidence, earthquakes and volcanoes endlessly impact on lives and damage expensive infrastructure every year [1]. Geophysical processes that drive these geohazards are all known to produce some kind of ground deformation [2]. This deformation of the ground in turn either damages or destroys capital infrastructure over or buried under these areas. As population increases each year, infrastructural development in hazardous areas is becoming common and the threats posed by these hazards are growing. Not all geophysical hazards are directed towards the uncertainty of crustal activity of the Earth. Earthquakes and volcanoes are probably the most devastating ones compared to other geophysical hazards that surface due to man made activities [1].

Landslides and subsidence are a common consequence of ground instability. Infrastructure built on unstable ground can be subjected to damage [1]. The collapse of natural or man-made cavities may produces ground movement; these are common with excess withdrawal of ground water, mineral extraction, oil production from oil wells, underground storage and engineering works that encompass deep excavations. These forms of deformation can either occur instantaneously resulting in massive failures or over long periods of gradual movement causing incremental damage. Gentle subsidence bowls develop almost imperceptibly slowly to a point where massive failure damages the regional infrastructure [3]. The effects of these damages have direct impact on the local economy. A means to detect the ground movement and prevent these damages would be a tremendous benefit to society.

Slope inclinometers, accelerometers, strain gauges, Global Positioning Systems (GPS) and theodolite surveys are the techniques currently in place to monitor the range of ground movement activity [4]. Geologists have relied on level meters and theodolite and electronic distance measurement (EDM) systems to acquire accurate coordinate and change in coordinate positions for monitoring ground deformation. GPS based monitoring has been adopted in several places and is fully operational for ground activity monitoring. These techniques often require regular site visits to place sensors for measurements and primarily rely on human invention [5]. Satellite-based remote sensing technology is gaining

acceptance in performing these surveys. Satellites often have a larger coverage and can be used to continually monitor an entire area at regular intervals. Synthetic Aperture Radar (SAR) mounted on a satellite can acquire data remotely and provide valuable information that can be used to detect and measure ground deformation to accuracies similar to the best traditional surveying methods [2]. Table 1-1 lists common ground deformation monitoring techniques and lists their relative accuracies.

Measuring Method	Typical Range	Observation Variable	Typical precision
GPS	Variable (< 20km)	$\Delta x, \Delta y, \Delta z$	5-10mm +1-2ppm
Elect. Dist. Meas. (EDM)	Variable (1-14km)	Δ distance	1-5mm + 1-5ppm
Wire Extensometer	<10-80m	Δ distance	0.3mm/30m
Surveying Triangulation	<300-1000m	$\Delta x, \Delta y, \Delta z$	5-10mm
Surveying Traverses	Variable	$\Delta x, \Delta y, \Delta z$	5-10mm
Geometrical Leveling	Variable	Δz	2-5mm/km
Ariel Photogrammetry	Ideally <100m	$\Delta x, \Delta y, \Delta z$	10cm
Terrestrial Photogrammetry	H_{flight} < 500m	$\Delta x, \Delta y, \Delta z$	20mm from 100m

Table 1-1: Accuracies of commonly used ground deformation measuring instruments [6]. Note 1 ppm means one part per million or 1 additional millimeter per kilometer of measured line.

This thesis focuses on a microwave remote sensing technique, referred to as Interferometric Synthetic Aperture Radar (InSAR), for detecting and measuring ground movement. SAR interferometry is a phase-based technique, which uses a coherent imaging system to extract topographical or deformation

maps from image pairs. This technique was primarily introduced to produce Digital Elevation Model (DEM) subsidence maps of deforming areas.

Acquiring and processing two or more single SAR images with known image acquisition geometry creates InSAR-derived deformation maps. These are often referred to as interferograms. Assuming the ground surface has changed during the acquisition of the two images, a comparison of image points from one image to the other will show slight phase changes due to displacement. Through a process called interferometric processing, topographic signals can be eliminated and thus the residual interferogram will provide a one-dimensional ground deformation map as perceived by the satellite. Figure 1-1 qualitatively illustrates the described technique.

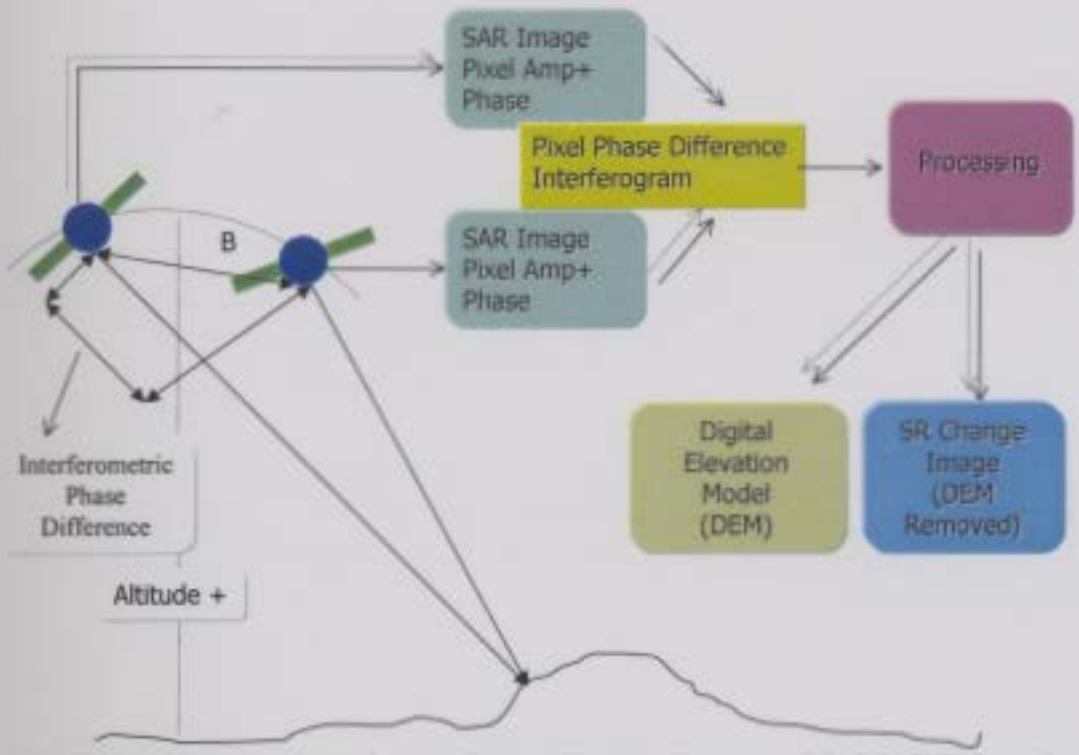

Figure 1-1: Illustration of InSAR for producing Digital Elevation Model (DEM) and ground displacement map or Slant Range (SR) change. B is the separation of the satellite orbits.

A literature review on InSAR ground movement monitoring (see chapter 2) reveals that most researchers have used terrain geometry (e.g., down slope) to make an assumption on the direction of the ground movement or, in the case of flat terrain, have assumed subsidence movement only [2]. While there has been research on fusing two satellite look directions for glacier movements, there has not been any work on fusing multiple look directions to generate three-dimensional movement in the absence of terrain trends. In the case where the terrain is flat and ground movement in the satellite look direction is significant, neglecting the lateral ground movement component could lead to significant errors in calculating the subsidence component. Consequently, deriving a technique to correct this problem in estimating both subsidence and lateral ground movement components will lead to more accurate movement measurements. In some cases, the estimation of the lateral ground movement is necessary to determine effects on buried infrastructure, including pipelines, foundations, wells, etc. In fact most regions that are undergoing subsidence are subjected to some sort of lateral movement. For example, an area in Southern California in the San Joaquin Valley is known to be subsiding [5]. The subsidence rate in the region is almost alarming and the region is also undergoing lateral movement due to such high subsidence rates. The work presented in [5] has estimated annual subsidence rates in North Belridge oil fields. Figure 1-2 is a photograph obtained of infrastructure damage in the

region of interest in North Belridge Oil Fields showing pipeline ruptured due to excessive ground movement. Careful observance of the picture reveals that the bend in the pipe appears to be due to lateral movement, not just subsidence. This region will be used as a test site for the research presented here.

Figure 1-2: Damages due to ground movement.[5]

Motivated by the urgency of an accurate remote sensing technique to monitor ground deformation in both the lateral and vertical directions, this thesis presents a technique using interferometry with data from satellite SAR. The technique can be used to improve the accuracy over single-pair subsidence estimates by fusing two non-parallel pass image pairs and measuring the lateral movement and subsidence. It is shown that, with other assumptions, three dimensional movement estimates can be derived from only two satellite look

directions by combining the look geometry with a constrained least squares estimation technique. Measuring and detecting these movements from SAR images will prove an invaluable tool for monitoring and detecting ground failures.

Chapter 2

Background Information

This chapter presents a literature review on SAR and SAR interferometric techniques for various remote sensing applications. It opens with the fundamental principles of SAR systems, introducing the key concepts that are requisite for processing raw SAR images. InSAR is discussed in detail to build up the concepts that are required for differential Interferometric SAR (DInSAR). A self-contained background of SAR, InSAR and DInSAR as a remote sensing technique will introduce the readers towards the problem objectively.

2.1 Synthetic Aperture Radar (SAR)

Conventional radars use time separation in round-trip delay of the target echoes to form an imprint of the backscattered signals [7]. The time separation of the back-scattered echoes generally form one imaging dimension of the radar while the radar's antenna aperture forms the second dimension. An illustration

of this is shown in Figure 2-1 for a conventional ground-based scanning radar in which the antenna aperture is placed transverse to the direction of propagation. The dimension formed by the time domain propagation is called the "range" while the dimension formed by the antenna aperture is called the "azimuth" direction. Moving or spinning (beam steering) the antenna transverse to the main direction of propagation forms the azimuth dimension.

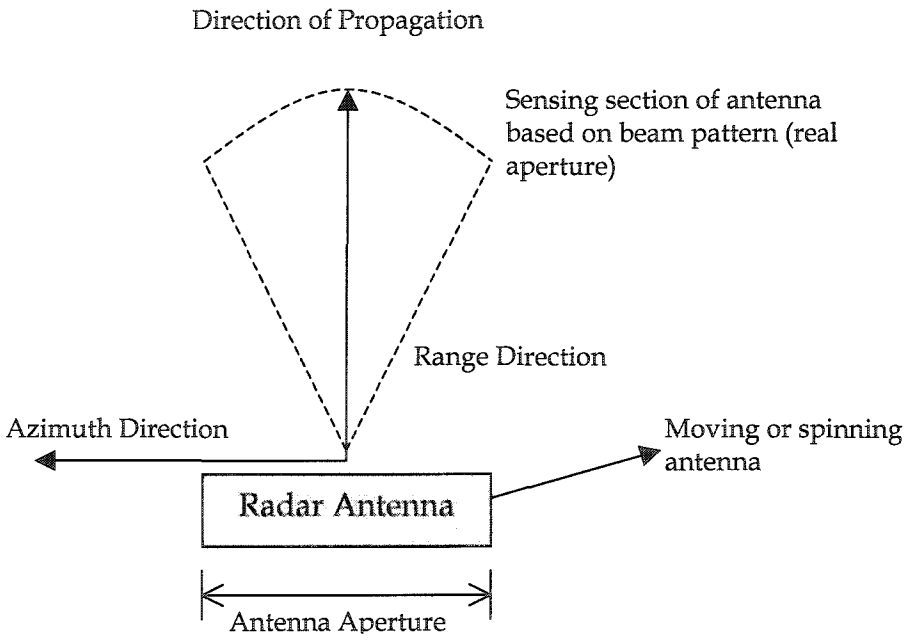

Figure 2-1: 2-Dimensional imaging geometry of real aperture radar

Real aperture radar forms its imaging "resolution" solely on the beam pattern of the real aperture of the antenna. Synthetic aperture radar is a modified version of real aperture radar. SAR combines the motion of the radar antenna to form a much bigger "synthetic aperture" that provides a much finer

azimuthal resolution than that of the real aperture alone. That is, instead of having an antenna with a large physical aperture to produce a desired resolution, SAR uses the antenna movement to synthesize a larger aperture. SAR is a coherent radar technique, which preserves both the amplitude and phase of the return signal thereby recording a measure of the target's aggregate reflection coefficient into each single imaged pixel [8,9]

2.1.1 SAR Imaging Geometry

The SAR imaging geometry as shown in Figure 2-2 graphically illustrates a satellite SAR antenna illuminating a surface strip (footprint) to one side of the nadir (directly below the flight path of the instrument) track. Side looking is necessary for SAR since it can eliminate any right-left ambiguity from symmetric equidistant points on the ground [8,9]. As the platform moves in its orbit, a continuous strip of swath width is mapped in the along-track direction of the satellite. The transmitted wave hits the target surface first at near range of the SAR illumination footprint and the separation of the backscattered signal along the swath width near range to far range is determined by the cross track resolution. The pulse width determines this cross-track or range resolution [8,9].

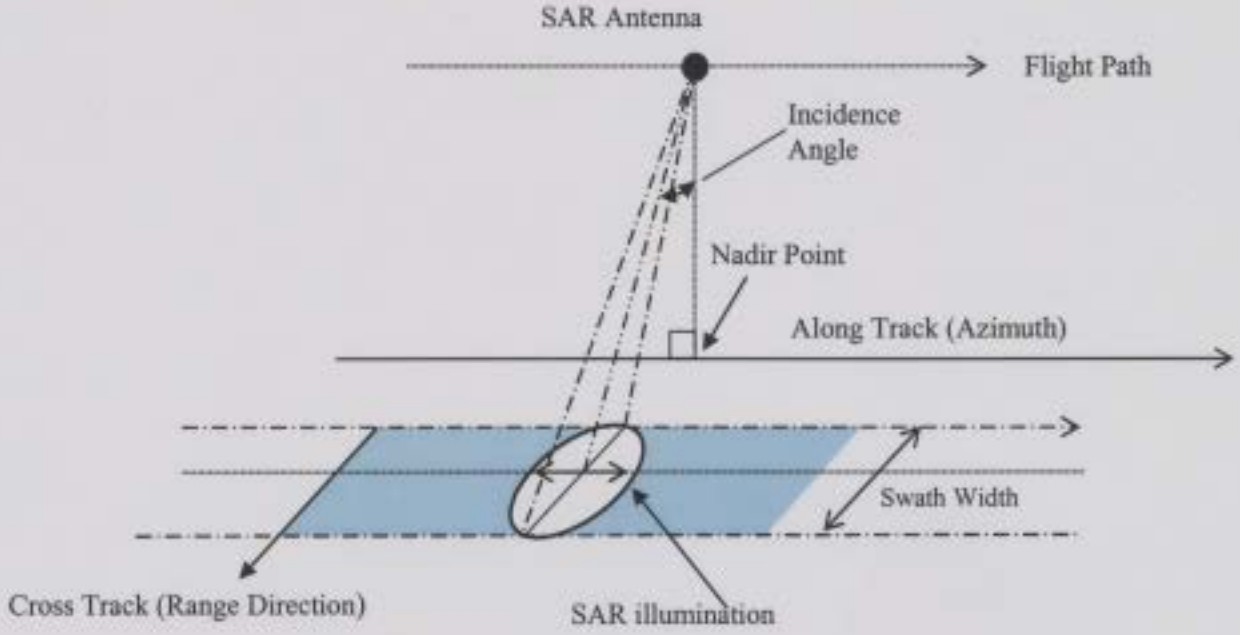

Figure 2-2: SAR imaging geometry illustration of a side looking SAR (redrawn from [10])

An image is formed from the echoes which are sensed coherently in the across track (range) and along track (azimuth from synthetic aperture) directions [11,12].

2.1.2 SAR Raw Image Acquisition

In raw SAR data, a single point target on the ground will have many return imprints on the acquired image. This means that, based on the target's shape, multiple pixels on the image will be affected. The objective of the raw SAR data processing step is to obtain a focused, single look complex (SLC) image, which consists of the entire received signal distributed over an illumination time, on one point at time $t = 0$ [10]. Consider Figure 2-3 which

illustrates the illumination of a point target and its multiple echo imprints on the obtained data. From Figure 2-3, x_1 is the distance traveled by the flying antenna from position $x = x_0 = 0$ with r_0 the distance from the first position at which P is illuminated by the antenna beam. The new distance r_1 is when the antenna is at position $x = x_1$.

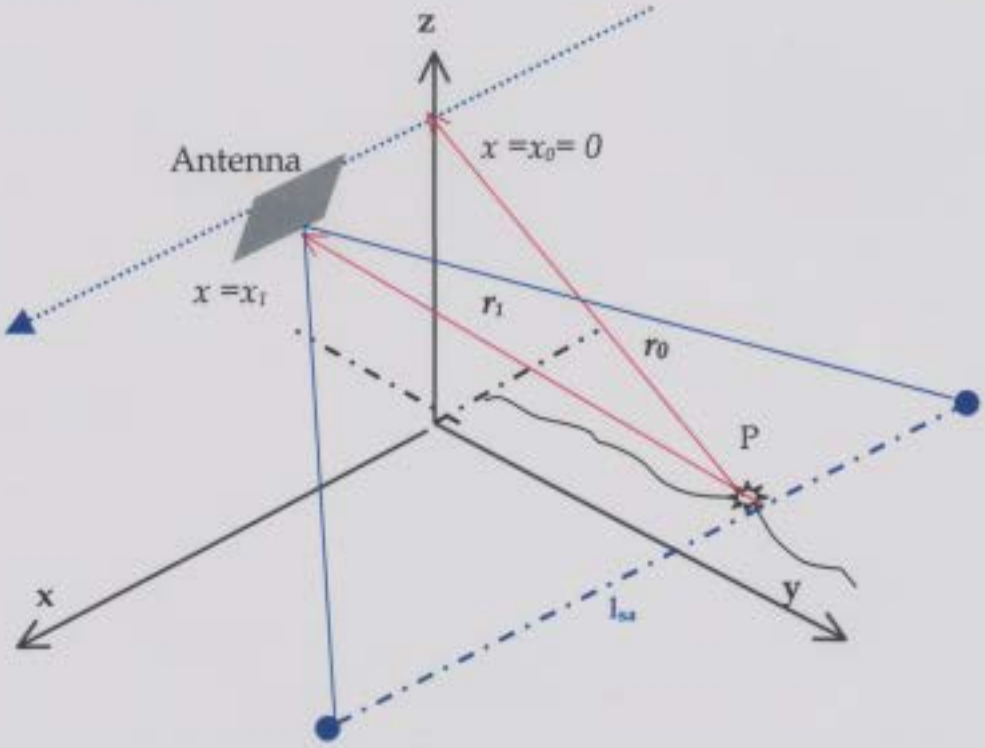

Figure 2-3: SAR antenna movement along the x -axis, radar pulses to the ground along the y -axis, time instant between position $x = 0$ to $x = x_1$ [10]

From this it is possible to express the distance between the sensor and the target when the former is at position $x = x_1$ as [10]:

$$r_1 = \sqrt{x_1^2 + r_0^2} \tag{2-1}$$

The radar footprint on ground is usually much smaller than the target distance

($x_1 << r_0$). Consequently, the square root approximation is followed by the binomial approximation [11,12]:

$$r_1 = r_0\sqrt{1+\frac{x_1^2}{r_0^2}} \approx r_0 + \frac{x_1^2}{2r_0} \tag{2-2}$$

Thus, for a wavelength λ_0, the phase $\varphi(x)$ (as a function of distance x along the azimuthal path), of the received echoes resulting after a distance r_1 is [11,12]:

$$\varphi(x) = 2\left(\frac{2\pi}{\lambda_0}\right)\left(r_0 + \frac{x_1^2}{2r_0}\right) = \frac{2\pi x_1^2}{\lambda_0 r_0} + \frac{4\pi r_0}{\lambda_0} = \frac{2\pi x_1^2}{\lambda_0 r_0} + const, \tag{2-3}$$

where the factor of 2 in equation (2-3) accounts for the two-way travel path from antenna to target and back to antenna.

Assuming constant sensor velocity v and neglecting the constant time independent phase term in equation (2-3), a quadratic phase behavior in time is obtained as [13]:

$$\varphi(t) = kt^2, \tag{2-4}$$

where $k = \frac{2\pi v_0^2}{\lambda_0 r_0}$ and v_0 is a constant sensor velocity. Thus with this relation the received azimuth frequency can be expressed as: [11,12]

$$f(t) = \frac{1}{2\pi}\frac{\partial\varphi(t)}{\partial t} = \frac{kt}{\pi} \tag{2-5}$$

Equation (2-5) is also called the Doppler effect and is only valid as long as x_1 is very small compared to r_0; otherwise, higher order terms in equation (2-2) have

to be considered. The Doppler ambiguity can be estimated by the blind de-convolution technique as suggested in [14]. That paper also suggests a technique for efficient focusing of SAR data.

To derive the expression of signal bandwidth in the azimuthal direction, consider the illumination time of a point target as defined by the extension of the antenna footprint in azimuth. This time duration is equal to the length of the synthetic aperture and is determined as in [13,15] (see Figure 2-3) :

$$t_{\max} = \frac{l_{sa}}{v} = \frac{\theta_{sa} r_0}{v} \tag{2-6}$$

where l_{sa} is the radar scan range on ground (synthetic aperture)

r_0 is the initial distance at $x = 0$ as shown in Figure 2-3

θ_{sa} is the change in look angle due to length l_{sa}

v is the velocity of the platform.

The bandwidth of the signal in azimuth is given as: [15]

$$B_{az} = f(-\frac{t_{\max}}{2}) - f(+\frac{t_{\max}}{2}) = \frac{2v\theta_{sa}}{\lambda_0} \tag{2-7}$$

The angular resolution α_{ra} with antenna length L in the azimuth direction can be represented as [13,15]:

$$\alpha_{ra} = \frac{\lambda_0}{L} \tag{2-8}$$

This is the minimum angular separation between two objects at the same distance that can be distinguished by the radar.

The spatial resolution in the azimuth direction for a given range r_0 is: [13,15]

$$\delta_{az} = \alpha_{ra} r_0 = \frac{\lambda_0 r_0}{L} \tag{2-9}$$

This means that azimuth resolution will decrease with the increase in r_0. A space-borne system of orbital height 800 km with L = 15 m would have a resolution of 3 km. However, for a SAR system the angular resolution α_{sa} of the synthetic aperture of length l_{sa} can be determined as: [13,15]

$$\alpha_{sa} = \frac{\lambda_0}{2 l_{sa}} \tag{2-10}$$

The factor (1/2) in equation (2-10) is due to the synthetic aperture formation. The length of the synthetic aperture is the length of the traversed path from which a target is illuminated and can be expressed as: [13,15]

$$l_{sa} = \alpha_{sa} r_0 = \frac{\lambda_0 r_0}{L} \tag{2-11}$$

For a fixed range on a single strip of ground imaged with a SAR system, θ_{sa} and α_{sa} are the same quantities. Thus, the achieved azimuthal spatial resolution can now be expressed as: [13,15]

$$\delta_{az} = \alpha_{sa} r_0 = \frac{L}{2} \tag{2-12}$$

Equation (2-12) shows the independence of range distance and the azimuthal resolution is determined only by the size of the real antenna. Appendix C further illustrates key concepts on raw SAR processing steps.

2.1.3 SAR Imaging Geometry and Terrain Relief

Along the range direction, SAR measures the distance from targets to the sensor. This distance, also referred to as slant range, can be converted to ground distance using simple transformations. The latter distance is referred to as ground range. The terrain relief gets distorted in SAR images after the ground range transformation, and this entirely depends on the SAR look angle [16]. These distortions can be broadly classified as follows:

Foreshortening Effects - For terrain that faces towards the SAR sensor whose slope is less than the radar incident (Figure 2-4), the slopes appear shorter than they actually are when observed in the map projection. The opposite happens for terrain facing away from the SAR sensor to apparently lengthen the slope in the SAR image. The amount of shortening or lengthening is determined by the incidence angle of the SAR beam relative to the slope [16]. Foreshortened areas appear bright (or dark on lengthened slopes) on SAR images since the reflected signal from terrain slope gets compressed in less pixel area on the image. Which means that the backscattered energy is a function of the local slope.

Shadowing Effects - If terrain facing away from a SAR sensor has a slope greater than the radar incident angle (Figure 2-4) then the area is not imaged by the radar. The incident angle and the back slope of the terrain determine this formation of a radar shadow [16].

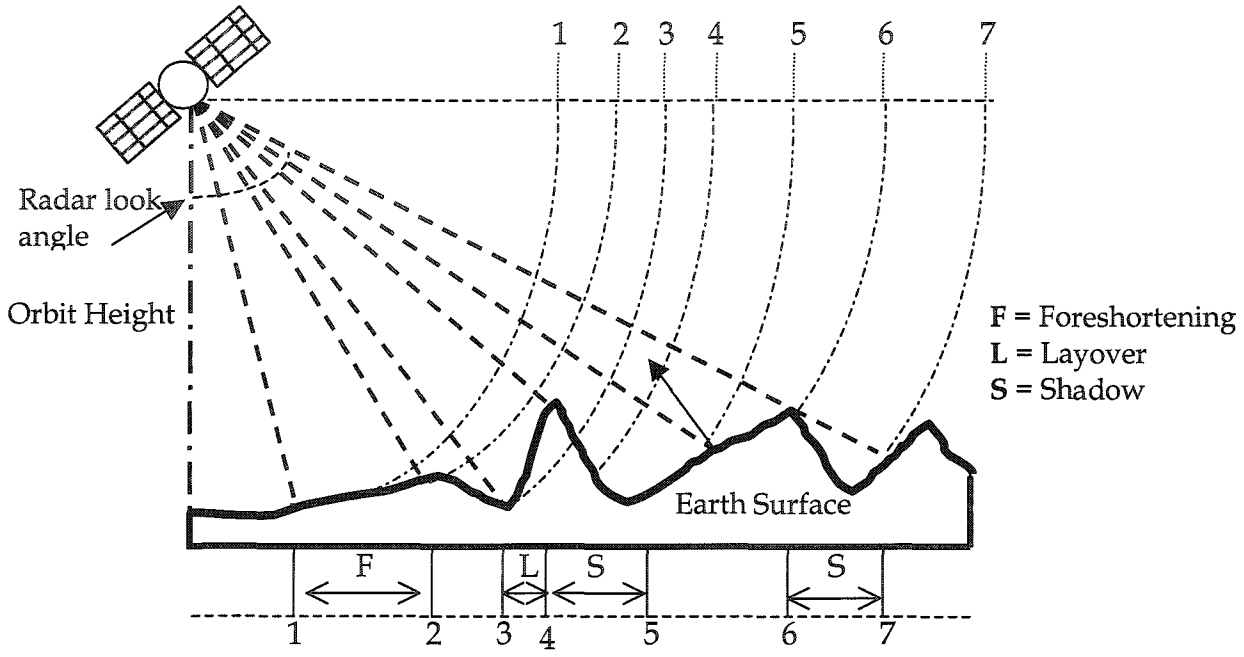

Figure 2-4: Terrain relief affecting SAR images. Slant range image shows the terrain as perceived by the SAR due to foreshortening, shadowing and layover distortions. [16]

Layover Effects - For terrain that faces towards the SAR sensor whose slope is greater than the radar incident angle, the top of the slope will appear closer than the bottom of the slope in SAR images [16]. This distortion is called layover, which means the top of the slope is laid over the bottom. Figure 2-5 illustrates this distortion effect on SAR images. Note the regions that are dark in the image and appear closer than the base of the slope.

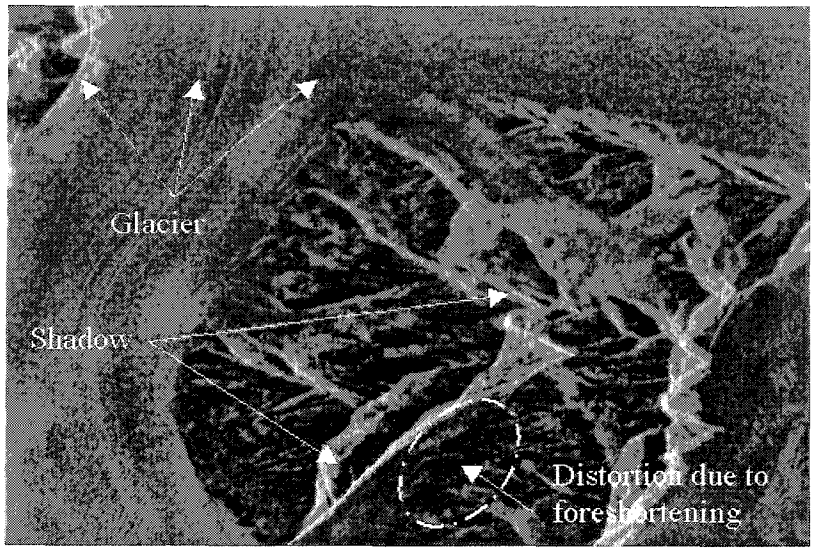

Figure 2-5: Image of Greenland (October 2002, ENVISAT) showing terrain relief and its impact on the SAR image [Courtesy C-CORE].

2.1.4 SAR Images

Each pixel (picture element) of a SAR image is a complex number and can be represented in magnitude and phase form as shown in Figure 2-6. The intensity of each pixel in the image represents the measured backscatter of the area. Bright areas on the image occur where a large proportion of the signal gets reflected back, while dark areas are where little energy is reflected back and a large part of the signal either gets absorbed or reflected away from the radar. In standard polar notation each SAR pixel can be represented as:

$$Z(x,y) = I(x,y)e^{j\phi(x,y)}, \tag{2-13}$$

Where Z is the complex value of the pixel

I is the intensity of the pixel

ϕ is the phase of the pixel

x, y are the image coordinate

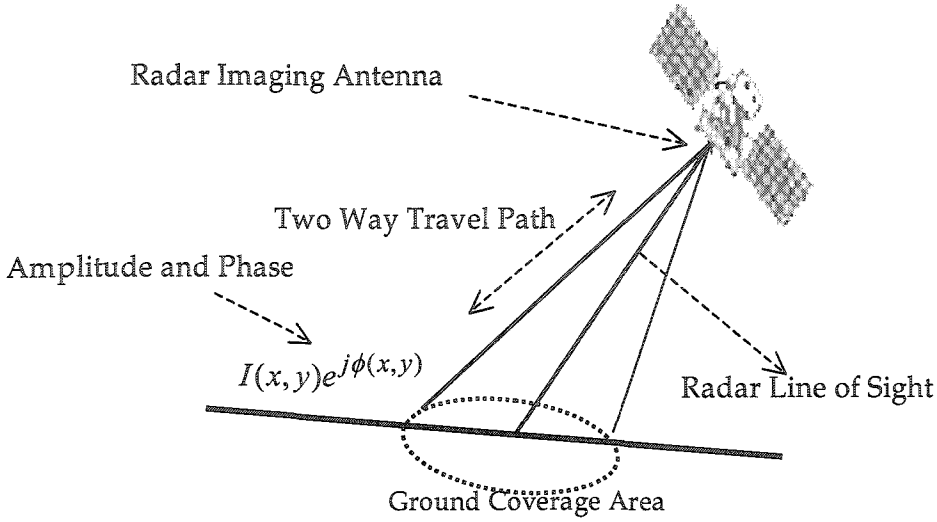

Figure 2-6: SAR imaging system with $I(x,y)e^{j\phi(x,y)}$ a SAR pixel (complex number)

The intensity and the phase terms in equation (2-13) are usually independent of each other.

2.2 Review of SAR/InSAR Development and Applications

Over the years, various possibilities for remote sensing with SAR have been demonstrated. Retrieval of imaged surface parameters has been the subject of many studies. In all of these studies, the areas of primary focus were on expressing backscattering coefficients and the parameters of phase difference statistics in terms of surface parameters such as height, correlation lengths and dielectric constants. These studies have enabled researchers to model and classify surfaces obtained from SAR images.

InSAR was first introduced for topographic mapping (sometimes referred to as relief maps) by Zebker and Goldstein [17] and its usefulness for accurate terrain mapping has been validated. Two complex SAR images of the ground under observation with similar viewing geometry will correlate with each other if obtained back to back. This correlated image pair is also referred to as coherence image [18]. Interferometry takes advantage of the coherence images and the created phase interferograms from these images to precisely measure terrain heights [17,19].

Land cover classification of terrain parameters has been extensively studied by a number of researchers. The primary focus in most of these studies was land-use mapping, where separation of forests and open fields was investigated. Some of the various applications for land classification from SAR images that have been investigated are canopy closure in dense forests, crop signature, barren land identification and agricultural crop heights [20,21,22]. Studies by Baronti [21] with C-band SAR shows the possibility of discriminating herbaceous crops and bare soil. Paloscia [23] investigated the possibility of extracting soil moisture content and hydrological parameters from SAR images. These techniques with SAR data open a range of possibilities to remotely observe crop watering cycle and soil moisture retention capabilities of different agricultural sites.

Zebker and Goldstein demonstrated capabilities of topographic mapping by InSAR observations using two L-band radar systems and verified results with data from the United States Geological Survey (USGS) [17, 24]. This success stimulated growing interest in InSAR terrain elevation and surface movement studies. A technique to detect surface motion was presented by Gabriel, Goldstein and Zebker [19]. Seasat images were used for this study and a great focus on surface change and parallax caused by topography is discussed.

A team of Italian researchers led by Prati and Rocca analyzed the limits and achievable resolution of elevation maps from stereo SAR images. Their main focus was on altimetric resolution with respect to satellite displacement in the cross-track direction [25]. They concluded that the maximum allowable displacement is limited by speckle noise (an artifact of a coherent imaging radar) and showed that achievable vertical resolution is better than slant range resolution times the cosine of off-nadir angle for about 99% of the image points. Speckle noise appears as random noise that can be visually observed as grains within a single SAR image. The phenomenon of speckle is common to all coherent radar systems. This type of noise can be reduced by an averaging technique called multi-looking [26, 27]. In the 1990's, there were several papers published mainly on InSAR error analysis techniques. These studies were on error sources and ways to mitigate errors [25,26,27]. A team of researchers [28] showed the effectiveness of SAR in areas of high seismic activities. Their main

focus was on the areas of seismic faults and ways to determine time-scale changes of the ground under observation .

To measure and detect subtle changes of the land under observation, an accurate baseline model is required. The InSAR baseline is the separation of the two orbits for the interferometric pair. The larger the separation of the two orbits, the larger are the errors associated with differential interferometric data. It is required to have a minimum separation to measure very small-scale movement. Li and Goldstein [29] reported the relation between InSAR correlation and topographic surfaces for the investigation of InSAR baseline models. Another study [30] showed that it is possible to develop very accurate topographic maps by eliminating errors due to shadowing and overlays in SAR image scenes by combining ascending and descending orbit data. In 1994, Gatelli et al. [31] reported further findings on mitigating errors for accurate topographic models. They describe the effects of terrain slopes in the imaged scene [31]. They suggested that, in the presence of a terrain slope, image one will be different from image two based on the acquisition geometry. This difference in the obtained data produces a shift in the range spectra of the interferometric couple. This effect, known as wave-number shift, has to be taken into account in order to avoid interferogram decorrelation associated with the geometry. The technique suggested to correct this decorrelation effect is to filter the image pairs with several wave-number filters [31]. These wave-number filters can be

developed from the knowledge of the local interferogram fringe frequency analysis.

SAR interferometry was successful in providing insight about the Landers earthquake by analyzing coseismical surface displacement gradients using SAR interferometry. It has been shown [32] that it is possible to measure slip distribution in earthquake belts. Various other earthquake studies with SAR interferometry indicated a promising future for this technique. Massonnet et al. [32] showed that fault lines could be detected with InSAR data and in particular the effects of the Landers earthquake could be measured by identifying fault lines from SAR images.

Various glacier studies show that ice velocity and melt rate of glaciers (in Greenland) could be measured using InSAR. In most of these studies (for example, [33]) the glacial movement was known or assumed for analysis. Using the same idea to detect changes from time series SAR data, various ground movement detections and measurements were carried out. It was shown that one-dimensional ice sheet movement can be detected and measured by InSAR [33]. To measure small-scale surface movement, a good topographic model of the same area is required. This can be used as the base reference model of the terrain under investigation and any change to that can be recorded as movement.

Various InSAR application projects for monitoring surface deformation proved the effectiveness of precisely measuring ground movement using SAR

images. A study was conducted in 1995 [26] to measure ground movement activity in Thuringia, Germany, an active mining area for uranium. A technique called Differential Interferometry or (DInSAR) was used to monitor movement in this region [26]. A set of corner reflectors (CR) was used to obtain a satisfactory coherence level in the successive image pairs for DInSAR. The CR's usually are the brightest objects in any SAR scene. With the knowledge of the imaging geometry and relative shift in the CR positions, a one-dimensional displacement measurement is possible. Other studies of subsidence monitoring in mining areas using a combined InSAR and GPS approach have been conducted [34,35]. These studies address the mitigation on mining disasters due to subsidence and collapse of underground mines, and demonstrated that by exploiting InSAR and global positioning system (GPS) data and fusing them together could obtain more accurate estimate of moving areas than either of the techniques alone. Traditionally monitoring these surface movements has been done using GPS surveys. However, GPS is limited in spatial coverage by the number of accurately placed receivers. InSAR under favorable condition is able to provide estimates of surface deformation due to these subsidences over the entire imaged scene.

Numerous studies have been carried out within this framework of natural hazards monitoring caused by ground movement, mainly subsidence. Slope

stability, landslide assessment and land-subsidence studies due to man-made disruption are the most researched areas with InSAR and DInSAR [9, 17, 19, 24, 28, 32, 33, 35].

Satellite remote sensing is still an evolving field; InSAR applications are not suitable for all areas. Areas with dense vegetation suffer from temporal decorrelation since in those regions InSAR image pairs become incoherent due to vegetation growth. Another source of errors would be uncertainty in satellite orbit. In the following section, an in-depth discussion of SAR interferometry is intended to lead the reader to the understanding that, even with these limitations, InSAR still remains an effective and accurate geodetic measurement method to monitor, measure, detect and anticipate surface movements remotely.

2.3 SAR Interferometry

To understand satellite interferometry one may consider the principles of a simple interferometer used in physics laboratories. The simplest interferometer is a two-sensor Michelson Interferometer, which can be used to measure path length differences as shown in Figure 2-7. The operation of the interferometer relies on two electromagnetic field sensors, S_1 and S_2 separated by a known distance called the baseline B. The two paths, P_1 and P_2, start at sensors S_1 and S_2, respectively, and end at the target t. A sinusoidal signal is generated at

sensor S_1 and the echo is received at both the sensors. If the triangle whose sides are P_1, P_2 and B are not isosceles then the reflected signal received at S_1 and S_2 will be out of phase. This phase difference $\phi = 2 \cdot \frac{2\pi}{\lambda}(P_2 - P_1)$ is used to compute the path length differences between P_1 and P_2. Obviously, the phase difference ϕ is directly proportional to path length difference $(P_2 - P_1)$ [36]. The sensors can both transmit and receive signals, which implies the effective path traveled by the signal is twice and hence a factor of 2 is observed in the phase difference equation. For a simple interferometer with one sensor acting as the transmitter and the other sensor acting as the receiver the phase difference can be related as $\phi = \frac{2\pi}{\lambda}(P_2 - P_1)$.

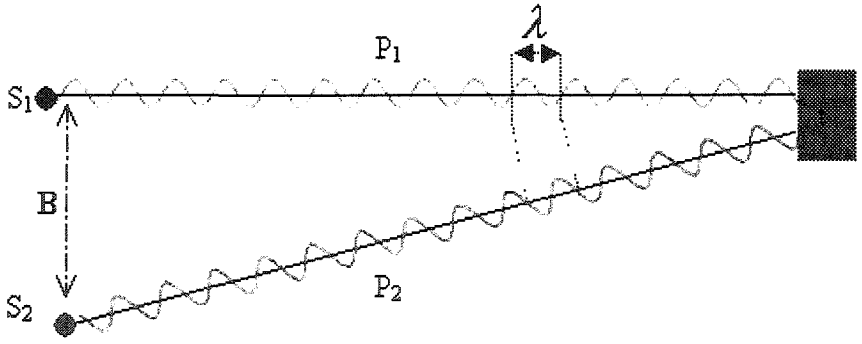

Figure 2-7: A simple interferometer geometry illustrated. λ is the wavelength, $P_1$and P_2 are the sensor to target distances, s_1 and s_2 are the sensors and B is the baseline.

InSAR uses the same principle to measure path length differences mapped to phase difference in estimating terrain height. With this information,

displacement of surfaces along the InSAR look direction can be detected and measured.

2.4 SAR Interferometry Data Acquisition Techniques

There are three primary ways that interferometric data can be acquired using onboard SAR sensors. A significant amount of research has been conducted in this area to identify which of these methods are suitable for various applications. There is information available on these methods elsewhere in the literature [9,11, 24, 29]. The basic principles of all these methods are given below.

2.4.1 Across-track Interferometry

In across-track interferometry two SAR sensors are mounted on a moving platform and are always perpendicular to the flight path. This technique is mostly used when SAR sensors are onboard an aircraft. The geometry used for phase to path variation is obtained from the aircraft flight plan. Consider Figure 2-8, which illustrates the basic geometry. The two sensors S_1 and S_2 are separated by a baseline B looking towards a point on the ground.

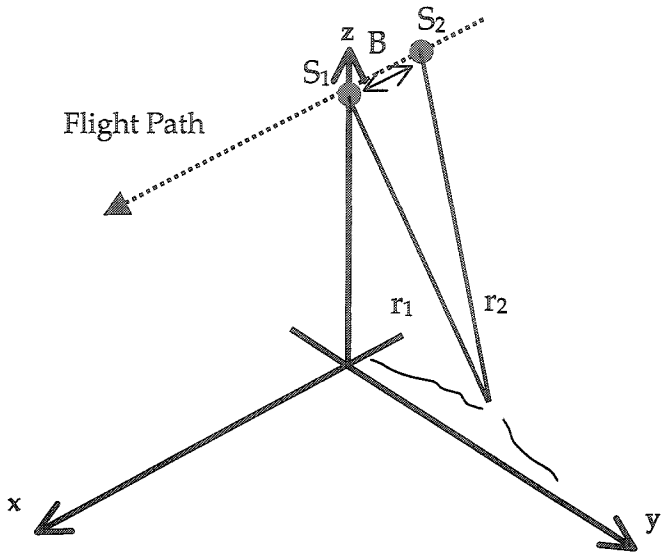

Figure 2-8: Across-track interferometry. S_1 and S_2 are the SAR sensors, r_1 and r_2 are the path lengths, B is the baseline [11]

The main disadvantage of this technique is that the aircraft roll is often difficult to account for and gets mixed with the terrain's natural slope.

2.4.2 Along-Track Interferometry

Along-track interferometry is similar to across-track interferometry and requires that both sensors be placed on the moving platform as shown in Figure 2-9. The difference in this case is that the flying antenna is mounted parallel to the flight path. This technique has been used to measure the velocity of targets since the flying path and look direction are on the same axis [24]. The measured phase difference between corresponding signals obtained from the two sensors accounts for the velocity of the target. Research has shown that this technique is

successful in obtaining ocean currents and moving targets such as glaciers and ice-sheets [24].

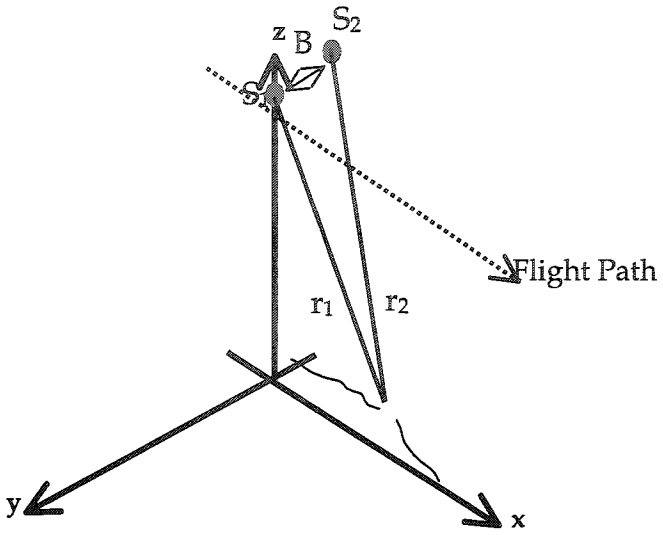

Figure 2-9: Along-track interferometry. S_1 and S_2 are the SAR sensors; r_1 and r_2 are the path lengths; B is the baseline [11]

2.4.3 Repeat-Pass Interferometry

In repeat-pass interferometry, a single SAR sensor, which is flown over the same region twice, is used. Since this technique requires only a single SAR antenna to be mounted onboard, it is suitable for satellites which have precisely known flight paths. The difference in satellite position for the consecutive passes forms the baseline. Consider Figure 2-10, which illustrates repeat-pass interferometry. The two observations from S_1 and S_2 at two different times are not the antenna phase center locations but points on the reference paths, which govern the cycle of phase difference along the swath. The horizontal separation

δ_h and the vertical separation δ_v of the reference paths, assuming the reference paths to be parallel, give the interferometric baseline. However, the actual separation is not always known; for example, there may be an uncertainty in the satellite orbit estimation. Therefore, the baseline should be estimated from the correlation between the two complex images obtained from S_1 and S_2. From the image acquisition geometry as shown in Figure 2-10, the difference $\rho - \rho_1$ in slant range, is as follows [11]:

$$\delta_r = \rho - \rho_1 = \frac{a\delta_h - (H-h)\delta_v}{\frac{\rho+\rho_1}{2}} - \frac{B^2}{2\left(\frac{\rho+\rho_1}{2}\right)} \qquad (2\text{-}14)$$

$$\text{where } B = \sqrt{\delta_h^2 + \delta_v^2}$$

All the variables in equation (2-14) are known from the geometry (indicated in Figure 2-10) and thus the path length difference to phase difference becomes $\phi = \frac{4\pi}{\lambda}\delta_r$ for the repeat-pass interferometry process. Table 2-1 lists some recently and previously available interferometric satellites used for remote sensing; all of them operate in repeat-pass mode.

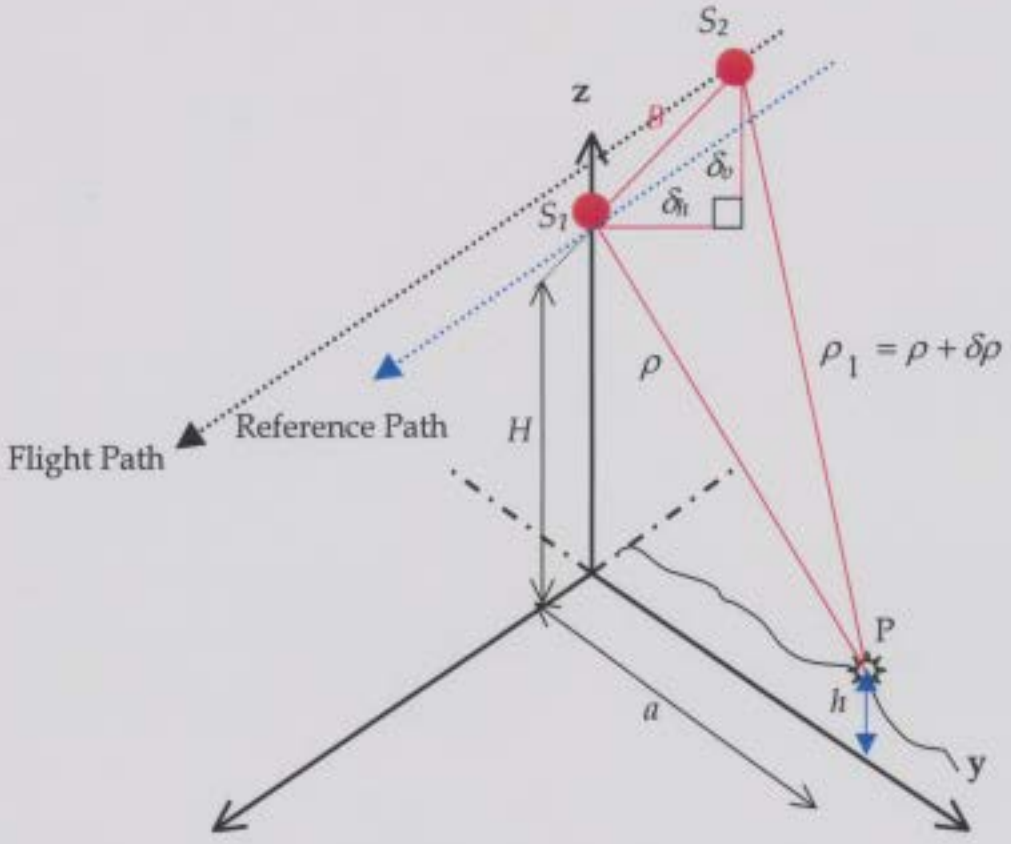

Figure 2-10: Repeat-pass interferometry. S_1 and S_2 are the SAR sensors, ρ and ρ_1 are path lengths with $\delta\rho$ as the absolute difference, B is the baseline. H is how far the orbit is from ground, a is the ground range, P is the target point on ground and h is the elevation of P, δ_h and δ_v are the components of B [11]

Satellite	Agency/ Country	Year Launched	Frequency Band (GHz)	Altitude (km)	Repetition Period (Days)	Incidence Angle	Swath Width (km)	Ground Resolution (m)
Seasat	NASA/USA	1978	L (1.3)	800	3	23°	100	23
ERS-1	ESA	1991	C (5.3)	785	3,35,168	23°	100	25
JERS-1	NASDA/ Japan	1992	L (1.2)	565	44	35°	75	30
SIR-C	NASA/USA DASA/ Germany ASI/Italy	1994	X (9.7), C (5.3) L (1.3)	225	Variable	15°-55°	15-90	10-200
ERS-2	ESA	1995	C (5.3)	785	35	23°	100	25
RADARSAT	CSA/Canada	1995	C (5.3)	792	24	20° - 50°	50-500	8-100
ENVISAT	ESA	2002	C (5.4)	800	35	15° - 45°		28-150

Table 2-1: List of remote sensing satellites capable of interferometry

2.5 SAR Interferometric Images

An interferogram is derived from the mathematical product of two complex co-registered SAR images; shown as an illustration in Figure 2-11.

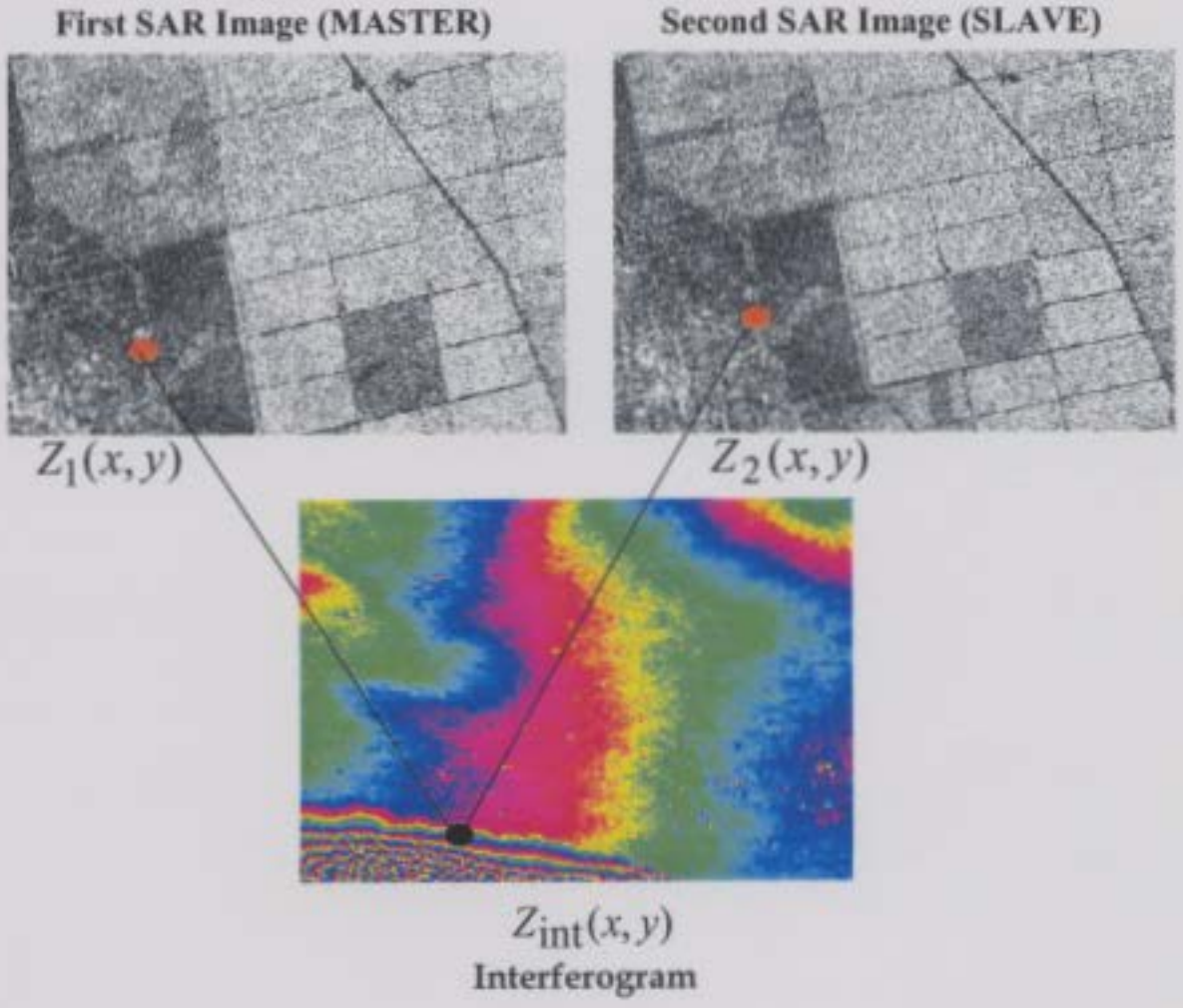

Figure 2-11: SAR master/slave pair with an interferogram. $Z_1(x,y)$ is in the master SAR image, $Z_2(x,y)$ is in the slave SAR image and $Z_{\text{int}}(x,y)$ is in the interferogram used to illustrate the concept. Every color cycle represents half wavelength shift of the propagation path.

The SAR images (master/slave) in Figure 2-11 may be represented as a complex matrix Z with x rows and y columns. Then Z_{int}, the interferometric image, is mathematically defined as [38]:

$$Z_{\text{int}} = Z_1(x,y)Z_2^*(x,y) \tag{2-15}$$

$$= I_1(x,y)I_2(x,y)e^{j(\phi_1(x,y)-\phi_2(x,y))} \tag{2-16}$$

$$= I_{\text{int}}(x,y)e^{j\phi_{\text{int}}(x,y)} \tag{2-17}$$

Where Z_{int} is a pixel on the interferogram,

$Z_1(x,y)$ is the pixel on the master SAR image,

$Z_2(x,y)$ is the pixel on the slave SAR image,

I_{int} is the intensity of the interferometric pair and

$\phi_{\text{int}}(x,y)$ is the interferometric phase with pixel coordinates x and y.

The operation of producing an interferogram requires that the obtained interferometric pair (master and slave image) be registered on either the master or slave image's grid (i.e. a pixel on both images should be the same geographical location). The registration of the two images has to be sub-pixel level accurate in order to obtain the proper interferometric patterns (interferometric fringes or fringes) [37,38]. The interferometric phase information is the most important for surface movement detection analysis or for generating a terrain map, otherwise known as a digital elevation model (DEM). A DEM of the area shown in Figure 2-11 can be found in Figure B-3, Appendix B.

2.6 Unwrapping of Interferometric Phases

In an interferogram, the measured phase will show an ambiguity of many cycles. To rectify this, it is necessary to add the correct integer number of phase

cycles to each of these measurements to "unwrap" the phase and remove the ambiguities. The measured phase from the interferogram $\phi_{\text{int}}(x,y)$ is continuous, and is wrapped modulo 2π, i.e. the original phase is wrapped to the base band of $(-\pi,\pi)$. Let the wrapped phase be defined as $\phi_{\text{int}}^{W}(x,y)$ where W symbolizes wrapped phases. The calculation of $\phi_{\text{int}}(x,y)$, which is the true phase, requires an integer multiple $k(x, y)$ of 2π to be added to the wrapped phase $\phi_{\text{int}}^{W}(x,y)$. The problem in solving this 2π ambiguity is defined as phase unwrapping and can be expressed as follows [11]:

$$\phi_{\text{int}}^{W}(x,y) = \phi_{\text{int}}(x,y) + 2k(x,y)\pi, \tag{2-18}$$

where $k(x, y)$ is a 2-D array of integers such that $-\pi < \phi_{\text{int}}^{W}(x,y) \le \pi$.

2.7 Fringe Patterns in Interferometric SAR Images

The phase patterns of an interferogram are sometimes referred to as interferometric fringes since they form edge-like patterns over the image. The fringes are observed in the interferogram as principle values of the measured phases on the interval $(-\pi,\pi)$. The modulo 2π unwrapping operation as discussed above may cause sudden discontinuities in the phases on this interval. To avoid such discontinuities and to be able to generate high quality fringe

images, it is important that the interferometric pairs be highly correlated. In other words, the coherence between the interferometric pair should be high [37].

Visible observation of an interferogram or fringe image gives valuable information about the nature of the terrain. High-density interferometric fringes suggest rapid variation of terrain altitude. Each 2π fringe cycle represents a specific elevation interval for all fringes in the interferogram. This interval is known as the altitude of ambiguity. Continuous closed fringe lines suggest areas of high phase-field consistency. The expression for roundtrip range variation as detailed in Figure 2-10, corresponds to altitude ambiguity $h(a)$, tied to wrapped phase, is as follows:

$$h(a) = \frac{(\rho + \Delta\rho)\lambda \tan\vartheta}{2\delta_h}, \text{ where} \tag{2-19}$$

$\rho, \Delta\rho$ are the range and range difference,

λ is the wavelength,

ϑ is the look angle (in the range direction),

δ_h is the horizontal component of the baseline.

The altitude ambiguity reflects the variation in terrain altitude corresponding to a 2π phase change [9].

It is well known that the interferometric phase is composed of the phase due to the real topography, phase due to the flat earth (reference phase) and phase due to the possible deformation of topography. In the raw interferogram, they are entangled into each other. The flat-earth phase caused by the reference

ellipsoid world geodetic system 1984 (WGS84) for the interferometric processing requires correction. For a certain (line, pixel) in the master image with corresponding coordinate (x, y, z) of the master/slave image pair, the same point on the reference ellipsoid is identified. The reference phase is then computed in a number of such points distributed over the total image. Next a 2-D polynomial is estimated, fitting these observations. A polynomial of degree 5 normally is sufficient to model the reference phase for a full scene and can be used to remove the flat-earth phases. This process is also referred to as the flattening of interferograms. After removing the flat earth phase components, the resultant phases reflect topography and change in topography (if at all present).

2.8 Coherence of SAR Images

Similar patterns of observed radar backscatter is a somewhat loose definition of coherence [38, 39]. Radar echoes are said to be coherent if the measurable quantities, both amplitude and phase are consistent. Two coherent echoes will be correlated with each other if they undergo the same interaction between a scatterer or a set of scatterers [39]. The coherence γ between two SAR images Z_1 and Z_2 is often defined as a complex correlation [38, 39] and is given by

$$\gamma = \frac{E[Z_1 Z_2^*]}{\sqrt{E[|Z_1|^2]E[|Z_2|^2]}}, \tag{2-20}$$

where $E[\ldots]$ is the expected value or mean value and can be calculated as the sampled average of the image scenes. Thus, sampled coherence is given by

$$\gamma = \frac{\Sigma_n Z_1 Z_2^*}{\sqrt{\Sigma_n |Z_1|^2 \Sigma_n |Z_2|^2}} \tag{2-21}$$

where Σ_n denotes summation over n pixels. This means coherence is a measure of statistical confidence in two SAR images. The standard deviation of the coherence estimator is proportional to $\frac{1}{\sqrt{n}}$ [38, 39].

In practice, coherence is often estimated by combining several adjacent pixels to limit statistical error propagation. From the above equation, the numerator is a sum of two vectors pointing in different directions, while the denominator is the square root of the sum of their individual squared moduli. This will induce an unwanted effect due to interferometric phase change ϕ_{int} and must be removed for accurate coherence estimation. To compensate for this in the coherence estimation, the vectors in the numerator must be de-skewed before summing [39]:

$$\gamma = \frac{\Sigma_n Z_1 Z_2^* e^{-j\phi_{\text{int}}}}{\sqrt{\Sigma_n |Z_1|^2 \Sigma_n |Z_2|^2}}, \tag{2-22}$$

A useful parameter can be estimated based on the coherence γ between a SAR interferometric pair. Signal to noise ratio determines effective signal power or usable signal power over noise power and in this case is a measure of quality between two SAR images. Here the signal is defined as the measured or observed phases in the interferometric pair. The expression that can be used to measure the induced phase noise over the fringe pattern of the interferogram is given by [39]:

$$SNR = \frac{|\gamma|}{1-|\gamma|} \quad . \tag{2-23}$$

2.9 Sources of Phase Noise in SAR Interferometry

Coherence γ is a quantitative measure that gives information about the usefulness of the SAR interferogram. High coherence is essential in the interferograms for accurate digital elevation model (DEM) generation and any other interferometric analysis involving SAR imagery. In repeat-pass interferometry, since the individual images of an image pair are not acquired at the same time, coherence can sometimes reveal information about changes in the imaged area between the two passes. The absolute value of coherence ranges between 0 (incoherence) to 1 (absolute coherence). The degree of coherence significantly influences the accuracy of phase differences and hence height measurements [40]. For repeat-pass interferometry, assuming there are no

volume scattering sources, such that all scattering happens at the surface, and neglecting errors in the SAR imaging process, the sources for coherence degradation can be classified as temporal decorrelation, baseline decorrelation and rotational decorrelation. Discussion below illustrates each of these decorrelation effects and their symptoms on SAR images.

Temporal Decorrelation

Temporal decorrelation often arises due to the physical changes in the imaged area between the two observations. The repeat times for various InSAR-capable satellites (Table 2-1) are from 24 hours to several months. Any change of the imaged terrain during this interval will influence the correlation of the image pair. These changes could be due to snowfall, vegetation growth, rain and melting of ice. The existing literature [39] suggests that the ground resolution-cell be modeled as a random set of point scatterers. Then temporal decorrelation can be thought of as changes in the positions of these scatterers between two observations. If it is assumed that changes in the position of these scatterers are independent of their initial position and their horizontal and vertical positions can be characterized by the independent Gaussian probability distributions, then the temporal correlation coefficient $\gamma_{temporal}$ can be written as [39]:

$$\gamma_{temporal} = e^{-\frac{1}{2}(\frac{4\pi}{\lambda})^2(\sigma_x^2 \sin^2\vartheta + \sigma_z^2 \cos^2\vartheta)}, \qquad (2\text{-}24)$$

where

σ_x root mean squared movement across track direction

σ_z root mean squared movement in the vertical direction

Baseline Decorrelation

In the previous sections the importance of the baseline in the quality of InSAR measurement from repeat-pass interferometry was discussed. Precise knowledge of the repeat orbit and the reference orbit is essential for quality InSAR products (interferogram, slant range change, DEM). For DEM, baselines that are too short can degrade the sensitivity to signal phase difference and are undetectable in extreme conditions, whereas baselines that are too long may induce additional noise due to spatial decorrelation and may corrupt the phase signal [29]. The theory relating to spatial baseline decorrelation has been extensively detailed in the literature [29, 41]. In reference to Figure 2-10, the relation between loss in correlation and increasing baseline are approximately linear and can be expressed as:

$$\gamma_{spatial} = 1 - \frac{2|B|R_a \cos^2 \vartheta}{\lambda \rho}, \tag{2-25}$$

where $\gamma_{spatial}$ is the spatial correlation coefficient,

B is the baseline,

R_a is the along track resolution,

ϑ is the look angle,

ρ is the slant range

and λ is the radar wavelength.

From the above equation, for a given wavelength λ and slant range ρ being constant, and assuming negligible variation in look angle ϑ, $\gamma_{spatial}$ is approximately linearly related to the baseline B. The value of B for which the spatial correlation coefficient $\gamma_{spatial}$ reduces to zero is defined as the critical baseline B_{cr}. This results in the backscatter of each pixel of the interferometric pair becoming completely uncorrelated. This can be easily shown using the equation above relating $\gamma_{spatial}$ and B_{cr} in the horizontal direction as follows [41].

$$\gamma_{spatial} = 0 \tag{2-26}$$

when

$$\frac{2B_{cr}R_a \cos^2 \vartheta}{\lambda \rho} = 1, \tag{2-27}$$

thus,

$$B_{cr} = \frac{\lambda \rho}{2R_a \cos^2 \vartheta}, \tag{2-28}$$

As an example, it may be noted that the critical baseline for ERS-1 and ERS-2 is approximately 1100 m [41]. Intense topographic variation can reduce the largest attainable baseline for topographic mapping. For a good quality DEM using ERS-1/2, it was estimated that the optimum baseline is around 200 m. Recent studies

in baseline estimation and decorrelation effects show that, by using spectral filters during range compression in the SAR data processing step, spatial decorrelation can be reduced [31]. This research publication introduces the concept of a tunable interferometric SAR (T-InSAR), which reduces loss of coherence due to large baselines.

Decorrelation due to Rotation

The rotation decorrelation effect is due to non-uniform illumination of the same scene in repeat-pass interferometry. It is not possible to illuminate the same patch of surface from two different angles and expect a fully correlated image pair. Literature suggests that, in repeat-pass interferometry, this effect can be mitigated if the two orbits are near-parallel [39]. Research and simulation suggest that rotational correlation coefficient $\gamma_{rotational}$ drops to zero at about 2.8° of orbital separation at L-band and about 0.7° at C-band [39].

Using all the decorrelation parameters listed above, the observed correlation coefficient can be obtained as the summation of all individual correlation coefficients. That is,

$$\gamma_{total} = \gamma_{temporal} \cdot \gamma_{spatial} \cdot \gamma_{rotational} . \qquad (2\text{-}29)$$

Knowing the SAR imaging geometry and SNR it is possible to estimate γ_{total} and then obtain a sense of the value of $\gamma_{temporal}$. This information is extremely important for any land surface change analysis with InSAR [39].

2.10 Principles of Extracting Topography from SAR Interferometry

To detect changes of a surface under investigation or to measure surface changes with centimeter accuracy, it is important to have a priori information (i.e. hilly, flat, rocky, vegetation, etc.) about the terrain. For detection and measurement of sub-centimeter level ground movement, an accurate DEM is required unless a zero baseline interferometric pair is made available. In the previous sections, the relation between topographic elevation and interferogram phases was quantitatively illustrated. This section will illustrate the viewing geometry for interferometric SAR in order to derive the fundamental equations for generating a DEM. It is almost impossible to obtain a zero baseline interferometric pair. A DEM under these conditions will enable differential interferometric processing to detect and measure ground movement. The technique in which two or more SAR interferometric pairs are combined together for ground movement analysis is known as differential interferometry (D-InSAR).

2.11 Equations for Deriving Topography from SAR Images

Consider Figure 2-12, which gives the same spatial configuration as Figure 2-10, illustrating repeat-pass interferometry viewing geometry. The SAR sensors S_1 and S_2 both illuminate the same patch on the ground and obtain images at two different times as a repeat-pass pair. In a right-handed coordinate system, the ground elevation at every point is a function of the range axis coordinate y and is denoted by $h(x,y)$. The separation of S_1 and S_2 is shown as B, which is the interferometric baseline and α is the angle of B with the horizontal plane. The distance between S_1 and a point P on the ground is shown as ρ and the distance between S_2 and that same point P on the ground is shown as $\rho + \delta\rho$. Angle ϑ denotes the SAR look angle of the imaging point P on the ground with respect to S_1. On each pass, the SAR onboard single antenna acts as both transmitter and receiver. Thus, for each observation the total distance measured will be double the path length. The elevation $h(x,y)$ of a point P on the ground can be written as [17, 19, 41, 42]:

$$h(x, y) = H - \rho \cos\vartheta \tag{2-30}$$

Using the law of cosines:

$$(\rho + \delta\rho)^2 = \rho^2 + B^2 - 2\rho B \cos(\frac{\pi}{2} - \vartheta + \alpha) \tag{2-31}$$

$$= \rho^2 + B^2 + 2\rho B \sin(\alpha - \vartheta) \tag{2-32}$$

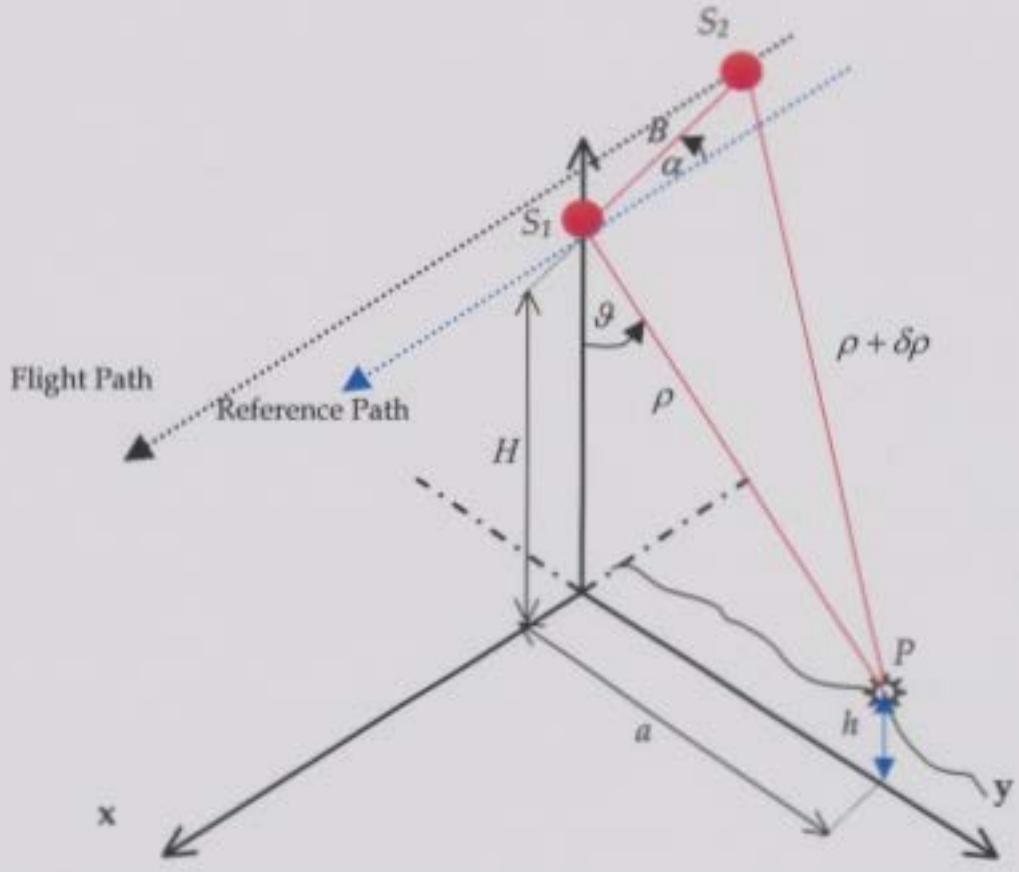

Figure 2-12: Repeat-pass geometry. S_1 and S_2 are the SAR sensors (antenna), ρ and $\delta\rho$ are the path lengths and variation of the path length and B is the baseline. H is how far the orbit is from the ground, a is the ground range, P is the target point on the ground and z is the elevation of P.

After expanding the right hand side and rearranging the equation:

$$\rho = \frac{\delta\rho^2 - B^2}{2B\sin(\alpha - \vartheta) - 2\delta\rho} \tag{2-33}$$

where $\delta\rho$ is the difference in range between the two passes. The phase difference, ϕ earlier defined as $\phi_{int}(x, y)$ is between S_1 and S_2 is directly proportional to the range difference as perceived by the two sensors and can be written as

$$\delta\rho = \frac{\lambda\phi}{4\pi} \,. \tag{2-34}$$

Combining equations (2-30), (2-32), (2-33) and (2-34) surface elevation can be written in terms of known or observed system parameters [17, 19, 41, 42]:

$$h(x,y) = H - \frac{\left[\left(\frac{\lambda\phi}{4\pi}\right)^2 - B^2\right]\cos\vartheta}{2B\sin(\alpha-\vartheta) - 2\left(\frac{\lambda\phi}{4\pi}\right)}. \tag{2-35}$$

Thus, an equation to generate the DEM from an interferometric pair is derived. The measured phase ϕ denoted in equation (2-34) is the principal value of the phase and is wrapped around ($-\pi$ π). The wrapped interferometric fringes will have discontinuities. Each interferometric fringe is interpreted as a constant separation of elevation increments δz from point to point as $h(x,y)$. In other words they represent height contours. As the real observed phases are wrapped around 2π, the phase must be unwrapped. The importance of coherence as detailed qualitatively in the previous section can now be mathematically expressed with the error in elevation estimates as follows (see, for example, [38]):

$$\sigma_h = \frac{\lambda\phi\sin\vartheta}{2\pi B}\sqrt{\frac{1-|\gamma|}{2|\gamma|}} \tag{2-36}$$

where γ is the coherence and σ_h is the expected error in elevation.

An interesting observation can be made after rearranging equation (2-34) as

$$\phi = \frac{4\pi}{\lambda}\delta\rho, \tag{2-37}$$

In this form, it is justified to say that the difference in phase measurement depends only on the imaging geometry and not on the scattering mechanism. Rearranging equation (2-33) so that the range change $\delta\rho$ is expressed in terms of the imaging geometry gives

$$\delta\rho = \frac{B^2}{2\rho} + B\sin(\alpha - \vartheta) - \frac{\delta\rho^2}{2\rho}. \tag{2-38}$$

The terms $\frac{\delta\rho^2}{2\rho}$ and $\frac{B^2}{2\rho}$ can be dropped since $2\rho >> \delta\rho^2$ and $2\rho >> B$. Consequently, the equation (2-38) can rewritten as

$$\delta\rho \approx B\sin(\alpha - \vartheta). \tag{2-39}$$

This is a valid assumption since the baseline B and change in slant range $\delta\rho^2$ are very small compared to two times the distance from a space borne radar to the Earth's surface, which is 2ρ. Next consider two interferograms (4 images, 2 interferometric pairs) acquired over the same area for a DInSAR pair, whose measured phase differences are ϕ_1 and ϕ_2 with B_1 and B_2 as their baselines. If it is considered that the look angle ϑ remains the same for the DInSAR pair, then the ratio of the phase differences only depends on the ratio of their baseline as:

$$\phi_1 = \left(\frac{4\pi}{\lambda}\right)\delta\rho_1 = \left(\frac{4\pi}{\lambda}\right)\left[B_1\sin(\alpha - \vartheta)\right], \tag{2-40}$$

$$\phi_2 = \left(\frac{4\pi}{\lambda}\right)\delta\rho_2 = \left(\frac{4\pi}{\lambda}\right)\left[B_2 \sin(\alpha - \vartheta)\right], \tag{2-41}$$

$$\frac{\phi_1}{\phi_2} = \frac{B_1}{B_2} \tag{2-42}$$

Equation (2-42) suggests that, if two interferograms were obtained from two independent SAR sources but using the same reference geometry, then one interferogram can be scaled by the ratio of their baselines and then subtracted from the other to yield displacement in the satellite line of sight (LOS) [48].

The sensitivity of phase change with respect to height change in a differential pair can be shown by first differentiating the phase equation to get

$$d\phi = -\frac{4\pi}{\lambda} B \cos(\alpha - \vartheta) d\vartheta \tag{2-43}$$

and then differentiating equation (2-30) with respect to ϑ and rearranging results as

$$d\vartheta = \frac{dh}{\rho \sin\vartheta}. \tag{2-44}$$

Combining equations (2-43) and (2-44)

$$d\phi = -\frac{4\pi}{\lambda} B \cos(\alpha - \vartheta) \frac{dh}{\rho \sin\vartheta} \tag{2-45}$$

Rearranging equation (2-45), reveals the dependence of phase change with respect to topographic elevation as [11, 17]

$$\frac{d\phi}{dh} = -\frac{4\pi}{\lambda} B \frac{\cos(\alpha - \vartheta)}{\rho \sin\vartheta} \tag{2-46}$$

Equation (2-46) can be used to very accurately estimate the change in topography provided every parameter on the right hand side is known. This effectively forms the foundation for DInSAR to detect and estimate change of topography. The following section illustrates DInSAR and different approaches towards DInSAR.

2.12 Differential Interferometry

Differential SAR Interferometry was proposed for the detection and measurement of very small elevation changes over large areas. The basic premise is to obtain interference patterns from SAR images due to *changes in topography*. In the conventional sense, DInSAR can be used to estimate one-dimensional ground movement from one interferometric SAR pair and a DEM. Optical path variation of the imaged scene due to changes in the terrain as perceived by the SAR system can be measured precisely using this technique, generally to sub-centimeter accuracy.

The detection and measurement of the displacement fringe from a change in topography is obtained by first generating an interferogram and then subtracting the fringes due to topography. After the removal of topographical fringes, the residual interference patterns provide a measure of displacement of topography between the interferometric image pairs.

DInSAR can be achieved by two different approaches:

- Four-pass interferometric pair or two-pass with an external DEM.
- Three-pass interferometric pair.

For the four-pass interferometric pair method, the first pair of images is used to generate a DEM; thus, no movement is assumed to have occurred between the acquisitions of the first two images. The subsequent interferometric pair is used for the DInSAR. In the four-pass method, DEMS can be generated for example using ERS-1/2 tandem mode where the time difference between passes is generally only one day. The third and fourth images are captured over the time period in which ground movement is desired to be measured and is generally obtained over a longer interval. For example, the time interval may be one or several orbit cycles of a single satellite, as long as coherence is maintained over that interval. The interferogram from the third and fourth image will exhibit fringes due to topography for non-zero baseline and might exhibit fringes due to change in topography. The reference DEM generated from the first pair or another source is used to remove topographical fringes.

The three-pass DInSAR method uses an interferometric triplet. Three SAR images are obtained, with the first two used to generate a reference DEM. The second and third image are used as the differential pair. For this case, the second and third images are chosen over the time period in which it is desired to measure ground movement.

2.13 Interpreting Subsidence from Differential Interferogram

From the discussions on interferometric fringes in Section 2.7, it was seen that interferometric phase of an interferogram is composed of the phase due to the real topography (assuming negligible decorrelation), phase due to the flat earth (reference phase) and phase due to the possible deformation of topography. Flat-earth phases are a result of the reference ellipsoid WGS84 used for the interferometric processing. After removal of topographic and flat earth phase components, a differential interferogram is left with interferometric fringes that arise due to ground movement. In stable areas where no ground movement is expected, a differential interferogram should be flat with no residual fringes. Figure B-4 in Appendix B, illustrates one such interferogram overlaid on top of the master SAR image as a transparent layer. Observe the area of subsidence shown in 3-D, which is also identified on the interferogram and the master SAR image. Note the flat areas beside the subsiding region in the interferogram. It is apparent by the uniform distribution of single colors that these regions are not undergoing any movement.

Displacement, being a vector, has both magnitude and direction, and the direction of this movement in flat regions is generally assumed to be along the z-axis (subsidence) [2,5,19]. However, in reality the differential interferogram only

shows ground movement as perceived along the SAR look angle. That is, only one component of the actual three-dimensional movement is recorded. Consider Figure 2-13, which illustrates the constituents of a differential interferogram. In Figure 2-13, **D** indicates the SAR look direction and **B** indicates the movement of a point on ground. SAR can only estimate the movement along its look direction; hence, **D** can be interpreted as the component of the movement **B** along the SAR look direction. Therefore, it becomes obvious that to measure subsidence (movement along the z-direction), it must be assumed that lateral movement components are zero such that **D** is the projection of subsidence alone.

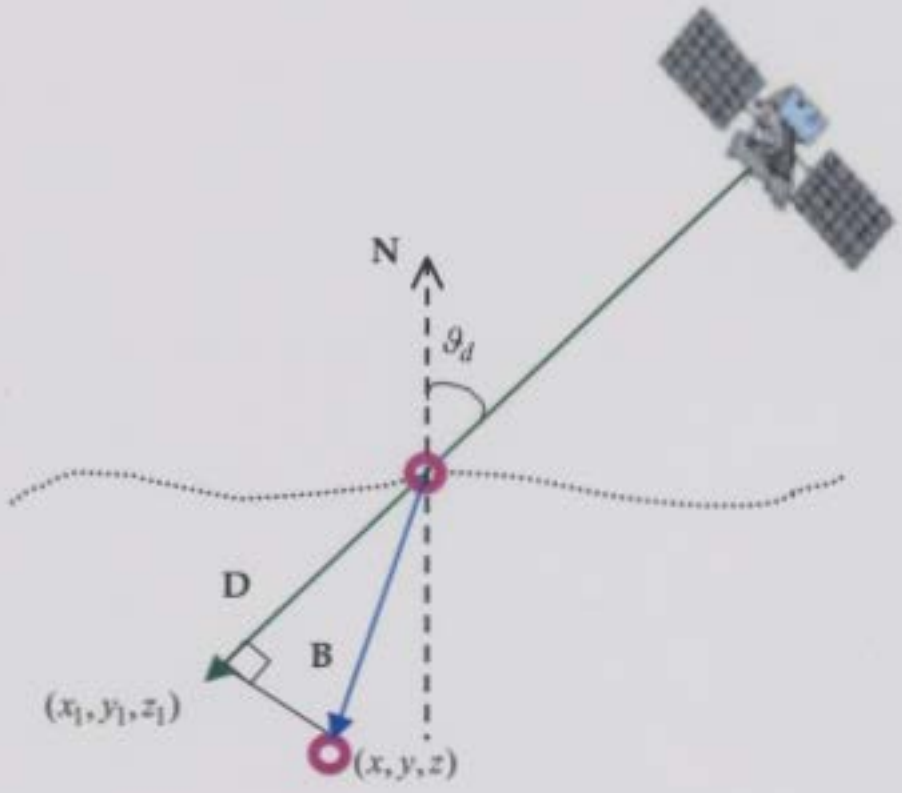

Figure 2-13: Ground subsidence from InSAR, where ϑ_d is the descending pass look angle

In principle, only one component of the displacement vector can be obtained from a single interferometric pair [19]. To measure three components of displacement, one must have three sets of interferometric pairs, each of which have different look directions, unless additional information (e.g., from ground observations) is available to determine the full three-dimensional displacement field [19]. However, the remote-sensing satellites capable of interferometry as listed in Table 2-1 can only obtain interferometric pairs with two different look directions. Most of these satellites are in near polar orbit, which means their trajectories are confined to roughly North Pole to South Pole orbits. The satellite trajectory from north to south is referred to as the descending pass and that from south to north as the ascending pass. Ascending pass interferograms differ from descending pass interferograms in their look directions. Thus, the combination of ascending pass and descending pass interferograms will give two components of the displacement vector along the plane of the radar line-of-sight. Each ascending and descending pair can be fused together to obtain 2-D ground movement from which the third dimension of movement can be estimated based on prior knowledge of the terrain. In the next chapter, this issue is further explored along with a technique to estimate 3-D movement from two look directions.

Chapter 3

Fusion of Ascending and Descending Pass Interferograms

The previous chapters have described SAR and DInSAR methods to derive general ground movement. It was seen that with satellite repeat-pass interferometry, topographical maps could be obtained. This leads to the discussion of the DInSAR technique and ways it can be used to obtain one dimensional displacement vectors of the imaged scene. This chapter will further dissect the DInSAR technique and develop a means to fuse more than one look direction.

Using DInSAR, if one look direction is used to obtain ground movement estimates, then only one dimension of movement can be derived. Other directions of movement must then be assumed from the topography. For example, moving slopes are generally assumed to be moving along the slope

direction. This would be a poor assumption if there are known "slumps" along the slope. Also, regions that are generally flat are assumed to have no lateral movement component such that the only movement is vertical (heave or subsidence). However, even for flat regions, the assumptions of zero lateral movement can produce significant subsidence measurement errors. This is true especially in the case of significant localized movement, whereby the sides of the moving region "cave in" towards a central maximum (negative sign convention used for subsidence) as shown in Figure 3-1.

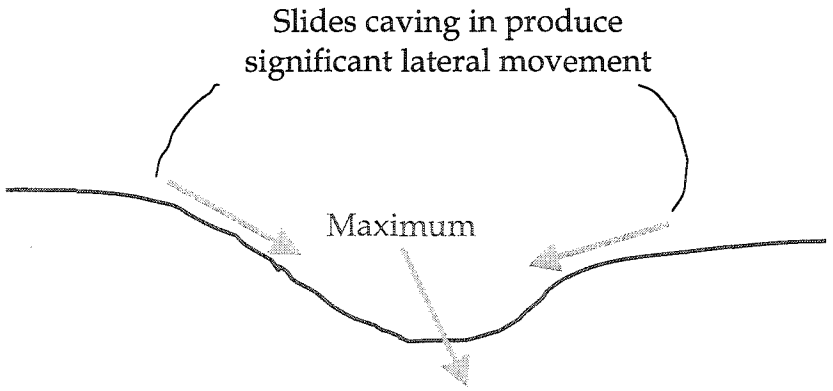

Figure 3-1: Sliding from both sides to produce lateral movement. Note: Figure B-4 in Appendix B illustrates the 3-D perspective.

Consequently, there is a rationale to improve ground movement estimates by fusing data from different look directions to produce 2D and possibly 3D movement. The sections below illustrate a technique to fuse different look

directions, and with the aid of least square techniques to produce an estimate of 3D movement.

3.1 Ascending and Descending Pass Geometry

As mentioned previously, space-borne SAR allows imaging of two look directions from ascending and descending passes. The fusion of two differential interferograms obtained from ascending and descending passes can be understood on the basis of their imaging geometry.

Figure 3-2 below provides an illustration of the orbital path of a typical polar orbiting satellite that allows two different look directions from ascending and descending passes.

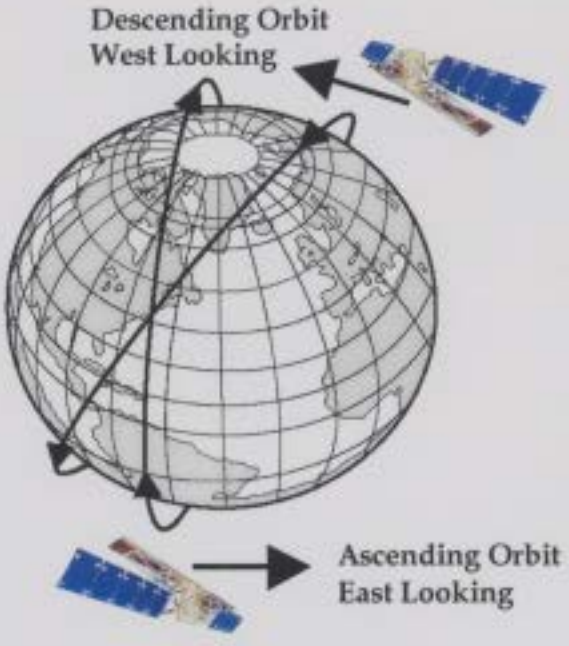

Figure 3-2: Descending and ascending orbits (RADARSAT International, 1996)

Most polar orbiting satellites look in a single direction, either the left or the right of their orbital path. For example RADARSAT-1 and ERS-1/2 are right looking

satellites, such that their look direction is to the East on the ascending pass, and to the West on the descending pass. The upcoming RADARSAT-2 can rotate its antenna to produce both a left and right looking direction. As Figure 3-2 illustrates, the orbital path is tilted slightly off the poles; for RADARSAT-1 and ERS-1/2 this tilt is roughly 8° from true North at the equator. As the satellites approach the poles, the map-projected orbit varies significantly from the 8° tilt. This is illustrated in Figure 3-3, which shows the map-projected coverage of RADARSAT-1.

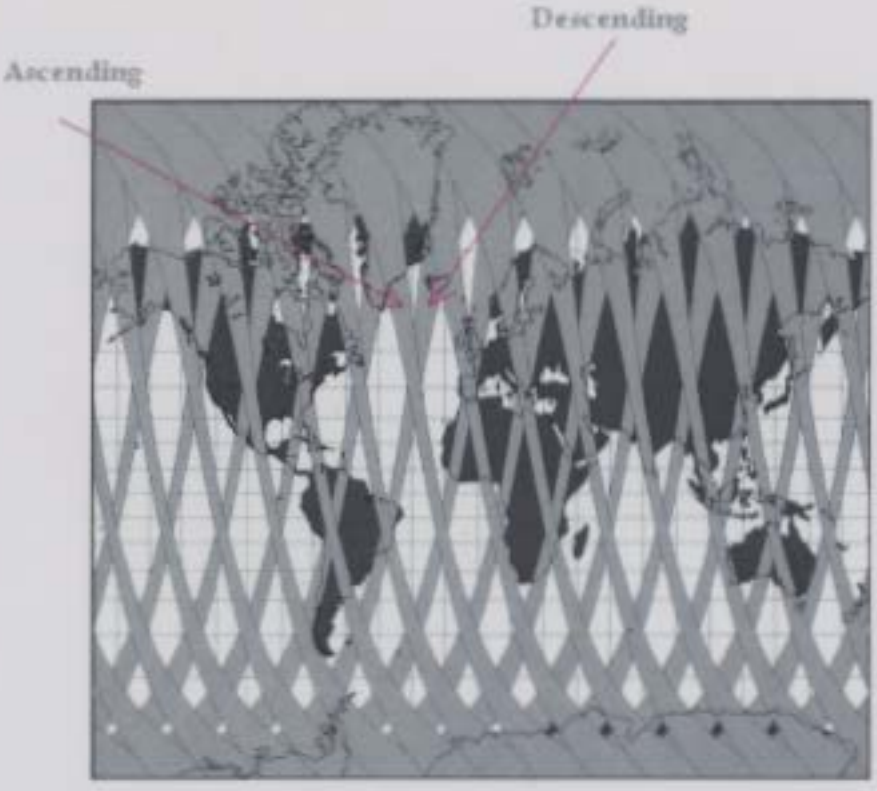

Figure 3-3: Coverage area for RADARSAT-1 for both ascending and descending passes. (RADARSAT International, 1996)

Figure 3-3 shows gradual change in map projected tilt angle from the equator, and then an abrupt curve in tilt angle at the top and bottom of the map. Over a

small segment of the orbit (one or two images) that is not near the poles, the map projected orbit path can be approximated by a straight line with a fixed tilt angle. A plan view of the look directions is illustrated in Figure 3-4 below.

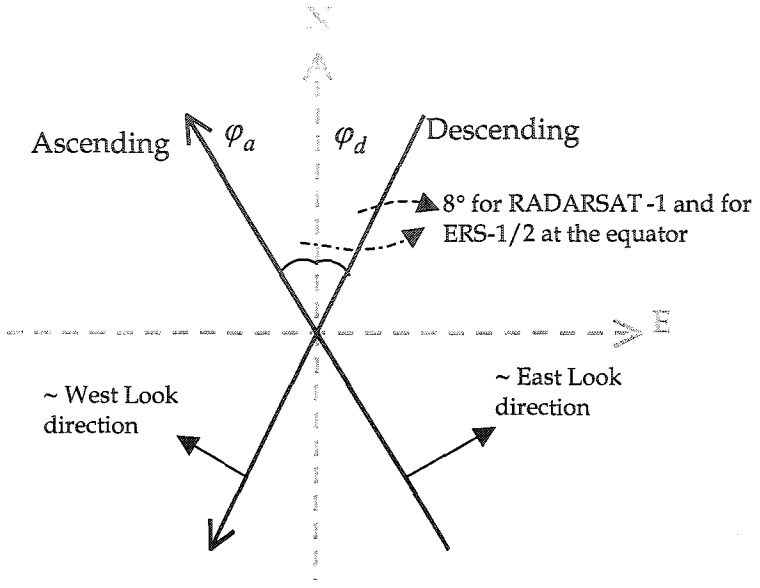

Figure 3-4: Plan view of satellite look direction illustrated

Now, consider a detailed profile view of the satellite look direction for each pass in Figure 3-5 and Figure 3-6. This profile view geometry has been discussed previously (cf. Figure 2-10), and will allow the decomposition of the differential slant range change to an actual ground movement vector. Consider the case where a point P on the ground has moved during a repeat pass and this movement vector is denoted as:

$$\mathbf{B} = \mathbf{L} + \mathbf{S},$$

where **B** is the movement of point P to P′ from pass one to pass two, **L** is the lateral component (East-West and North-South components) and **S** is the subsidence component. Using Cartesian coordinates:

$$\mathbf{L} = EW_x\,\hat{x} + NS_y\,\hat{y} = \Delta x\hat{x} + \Delta y\hat{y}, \tag{3-1}$$

and

$$\mathbf{S} = S_z\,\hat{z} = \Delta z\hat{z}\ ; \tag{3-2}$$

thus, **B** can be represented as

$$\mathbf{B} = \Delta x\hat{x} + \Delta y\hat{y} + \Delta z\hat{z}, \tag{3-3}$$

where $\hat{x}$, $\hat{y}$ and $\hat{z}$ denotes the East-West, North-South and Vertical direction in a right hand coordinate system with origin at P.

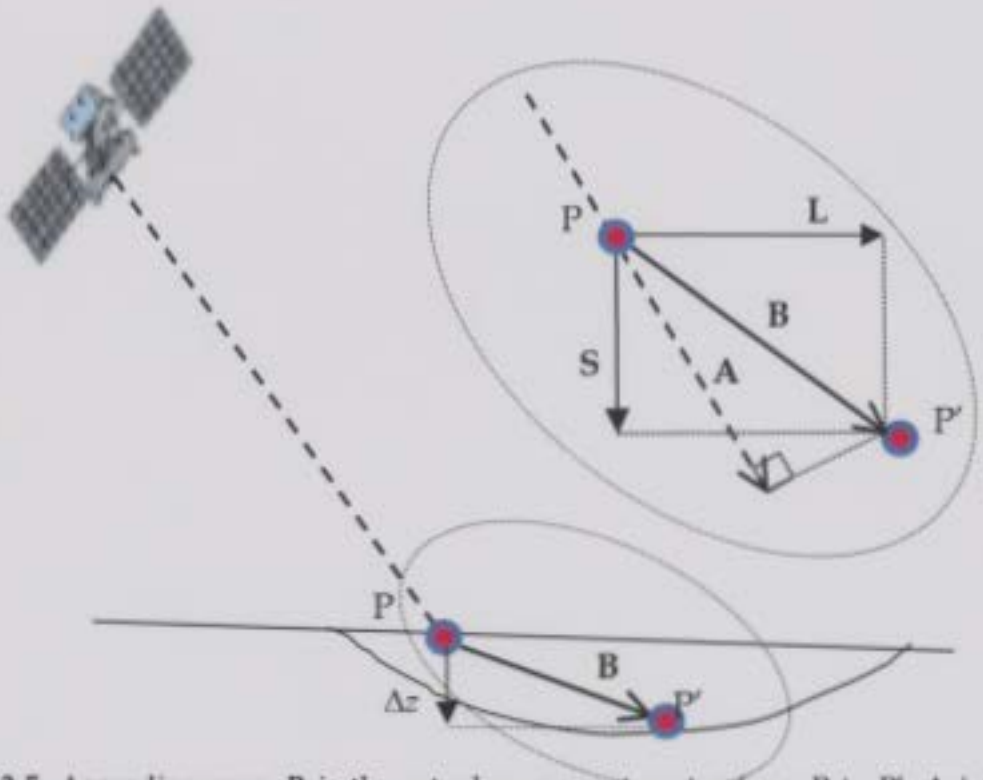

Figure 3-5: Ascending pass. **B** is the actual movement vector from P to P′, **A** is the measured component of **B** from ascending pass, **S** is subsidence component and **L** is lateral component.

As shown in Figures 3-5 and 3-6, **A** and **D** are obtained from ascending and descending differential interferogram, and are the measured components of the movement **B**. Thus, **A** denotes the measured component of **B** along the SAR look direction for an ascending pass as shown in Figure 3-5. Similarly **D** denotes the measured component of **B** along the SAR look direction for a descending pass as shown in Figure 3-6.

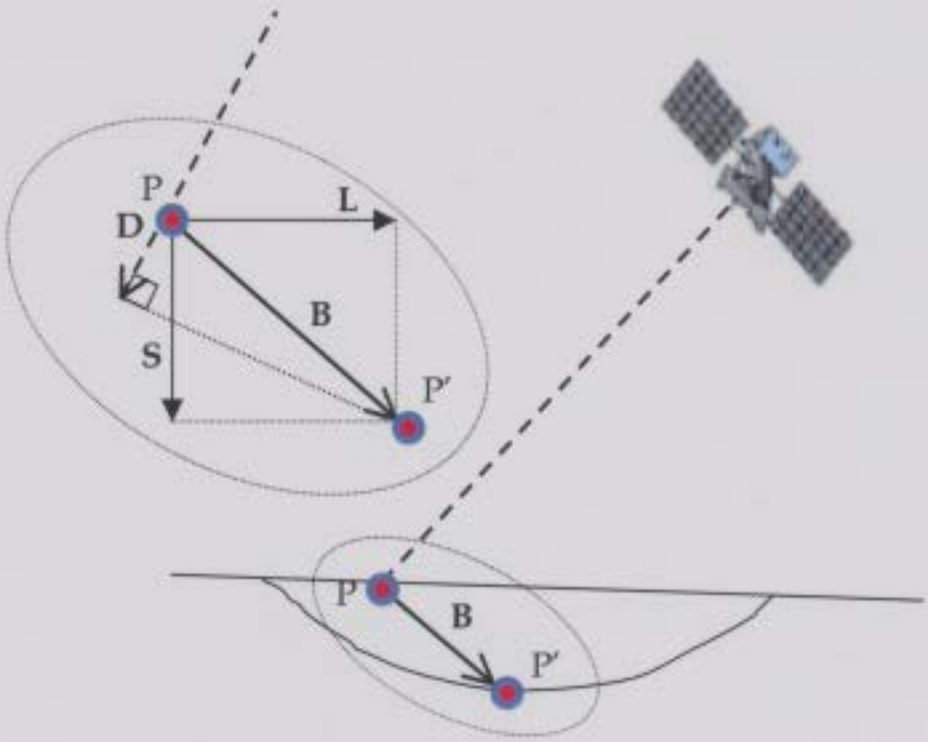

Figure 3-6: Descending pass. **B** is the actual movement vector from P to P', **D** is the measured component of **B** from descending pass, **S** is subsidence component and **L** is lateral component.

3.2 Ascending and Descending Pass Equations

The fact that the satellite measures a slant range change along the line of sight of the sensor is suggestive of the use of a circular coordinate system. This

will conveniently allow the conversion to a Cartesian (map oriented) coordinate system to express ground movement in terms of vertical and lateral components. Consider now the relationship between the satellite coordinate system, consisting of incidence angle ϑ, orbit tilt angle φ and slant range change (**D**, **A**, since these vectors are obtained from a differential interferogram) to the standard spherical coordinate system consisting of unit vectors $<\hat{\rho},\hat{\theta},\hat{\phi}>$. As shown in Figure 3-7, the satellite incidence angle ϑ can be expressed in circular coordinates $<\rho,\theta,\phi>$ as

$$\vartheta = \pi - \theta . \tag{3-4}$$

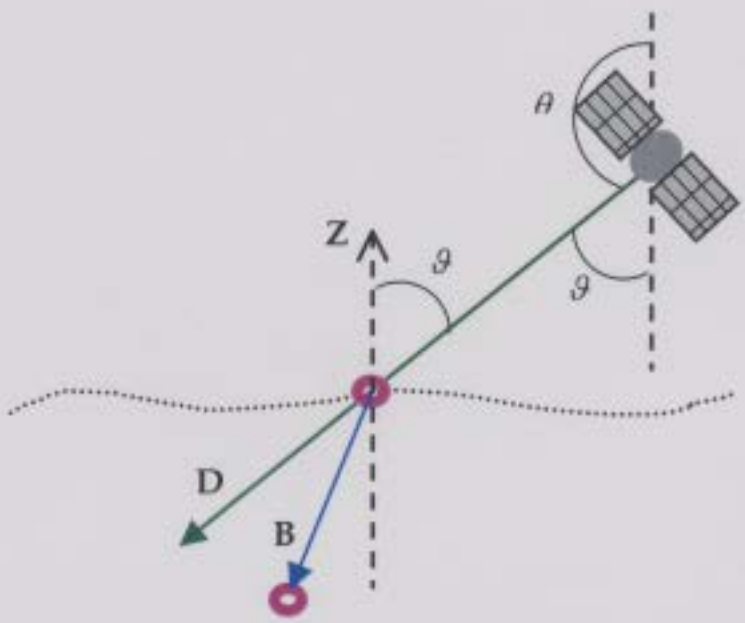

Figure 3-7: Relating look angle ϑ with respect to circular coordinate θ

The satellite orbit, presently expressed in terms of the tilt angle φ, can also be expressed in terms of the circular coordinates with the origin at the measured

point on the ground shown in Figure 3-8. Since the geometry of the tilt angle is different for the ascending and descending passes, Figure 3-8 shows the two different cases relating φ_a to ϕ_a on the ascending pass and φ_d to ϕ_d on the descending pass. Thus, the relation between orbit tilt to spherical coordinates becomes:

$$\phi_a = \varphi_a, \text{ and} \tag{3-5}$$

$$\phi_d = \pi - \varphi_d \tag{3-6}$$

Finally, the slant range change vectors **D** and **A** are oriented in the $\hat{\rho}$ direction. Therefore, it becomes possible to formulate the transformation of slant range change, look angle and look direction for two different look directions to standard spherical coordinates, replacing $<\hat{A},\vartheta_a,\varphi_a>$ to corresponding $<\rho_a,\theta_a,\phi_a>$ for ascending pass geometry, and $<\hat{D},\vartheta_d,\varphi_d>$ to $<\rho_d,\theta_d,\phi_d>$ for descending pass geometry.

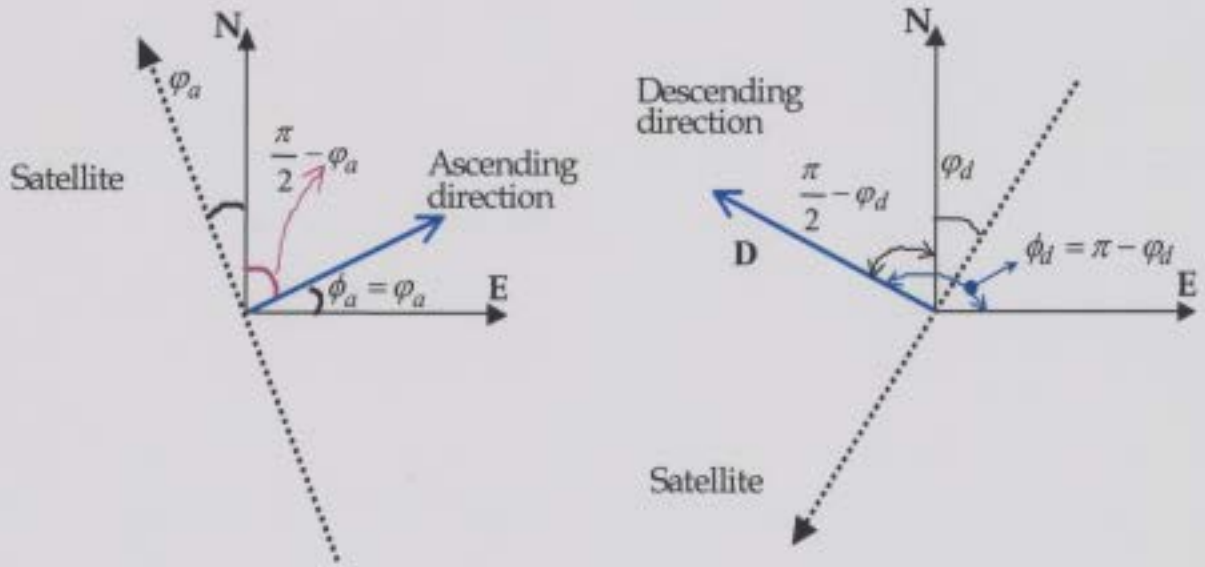

Figure 3-8: Relating satellite co-ordinate system to geometrical coordinate system, where φ_a and φ_d are the angles relating to inclination of satellite trajectory with respect to geographical North-South for ascending and descending passes.

The final transformation from the spherical to map projected Cartesian (EW, NS and Subsidence) system is achieved with a standard dot product table (Table 3-9).

·	$\hat{\rho}$	$\hat{\theta}$	$\hat{\phi}$
$\hat{x}$	$\sin\theta\cos\phi$	$\cos\theta\cos\phi$	$-\sin\phi$
$\hat{y}$	$\sin\theta\sin\phi$	$\cos\theta\sin\phi$	$\cos\phi$
$\hat{z}$	$\cos\theta$	$-\sin\theta$	0

Table 3-9: Dot product table relating spherical coordinate system to Cartesian coordinate system

Using all of the previous relationships, equations can now be derived to allow the fusion of ascending and descending pass DInSAR data. For the descending pass geometry, the equations are

$$\mathbb{D} = \Delta\rho_d \hat{\rho} = \Delta x_1 \hat{x} + \Delta y_1 \hat{y} + \Delta z_1 \hat{z} \tag{3-7}$$

$$\mathbb{B} = \Delta x \hat{x} + \Delta y \hat{y} + \Delta z \hat{z} \tag{3-8}$$

where,

$$\Delta x_1 = \Delta\rho_d \sin(\theta_d)\cos(\phi_d) \tag{3-9}$$

$$\Delta y_1 = \Delta\rho_d \sin(\theta_d)\sin(\phi_d) \tag{3-10}$$

$$\Delta z_1 = \Delta\rho_d \cos(\theta_d), \tag{3-11}$$

come directly from the dot product table of Figure 3-9 and $\Delta\rho_d$ is the measured slant range change in the descending direction. Hence the dot product of $\mathbf{B}$ and $\mathbf{D}$ is given by:

$$\mathbf{B} \cdot \mathbf{D} = \Delta x_1 \cdot \Delta x + \Delta y_1 \cdot \Delta y + \Delta z_1 \cdot \Delta z \tag{3-12}$$

$$\mathbf{B} \cdot \mathbf{D} = \Delta\rho_d[-\sin(\vartheta_d)\cos(\varphi_d)\Delta x + \sin(\vartheta_d)\sin(\varphi_d)\Delta y + \cos(\vartheta_d)\Delta z] \tag{3-13}$$

Now, to get the component of $\mathbf{B}$ in the $\mathbf{D}$ direction, the dot product is divided by $|\mathbf{D}|$ as follows:

$$\frac{\mathbf{B} \cdot \mathbf{D}}{|\mathbf{D}|} = \mathbf{B} \cdot \hat{D}, \tag{3-14}$$

where,

$$|\mathbf{D}| = \Delta\rho_d \tag{3-15}$$

Expanding the above equation gives:

$$\mathbb{B} \cdot \hat{D} = -\sin(\vartheta_d)\cos(\varphi_d)\Delta x + \sin(\vartheta_d)\sin(\varphi_d)\Delta y + \cos(\vartheta_d)\Delta z. \tag{3-16}$$

Recall now the elements of equation (3-16):

- ρ_d is the slant range change (differential interferogram of descending pass);
- φ_d is the projection of the satellite trajectory for descending pass;
- ϑ_d is the corresponding incidence angle of the descending pass;

- Δx is the displacement along the x axis;
- Δy is the displacement along the y axis; and
- Δz is the displacement along the z axis.

Similarly it is possible to derive the equation for the ascending pass geometry.

$$\mathbf{B} \cdot \hat{A} = -\sin(\vartheta_a)\cos(\varphi_a)\Delta x - \sin(\vartheta_a)\sin(\varphi_a)\Delta y + \cos(\vartheta_a)\Delta z\,, \qquad (3\text{-}17)$$

where in this case,

- φ_a is the projection of the satellite trajectory for ascending pass
- ϑ_a is the corresponding incidence angle of the ascending pass.

Using equation (3-16) and (3-17) it is now possible to complete a relationship between components $\Delta x, \Delta y, \Delta z$ and slant range change measurements. The derived set of equations can be represented in a compact matrix form:

$$\begin{bmatrix} -\sin(\vartheta_d)\cos(\varphi_d) & \sin(\vartheta_d)\sin(\varphi_d) & \cos(\vartheta_d) \\ -\sin(\vartheta_a)\cos(\varphi_a) & -\sin(\vartheta_a)\sin(\varphi_a) & \cos(\vartheta_a) \end{bmatrix} \begin{bmatrix} \Delta x \\ \Delta y \\ \Delta z \end{bmatrix} = \begin{bmatrix} \Delta\rho_d \\ \Delta\rho_a \end{bmatrix}. \qquad (3\text{-}18)$$

Equation (3-16) and (3-17) can be independently used to extract any one of the three dimensional ground movement components, either by setting the other two components to be zero or by using prior information about their magnitude and direction. The system of equations (3-18) is under-determined with two equations and three unknowns. The incidence angles of the SAR, ϑ_a and ϑ_d are represented as constants over the entire scene and the representative value is at

the center range pixel of the SAR scene. The incidence angle can be calculated for each range pixel of the SAR scene with the knowledge of its value at the center. Though the change in incidence angle from one pixel to the other is very small over a given scene, this information can be utilized to construct an over-determined system of equations. The variations in φ_a and φ_d are negligible over a single scene and are often treated as constants.

To resolve the under-determined system, as a first approximation, one of the displacement variables can be assumed to be zero. For example, polar orbiting satellites have look directions that are predominantly in the East-West direction. As a result, the slant range change is less sensitive to lateral movement in the North-South direction. Thus, a first approximation could use the assumption that lateral movement in the North-South direction (i.e. Δy) is zero.

3.3 Estimating 3-D Ground Movement

The synthesis equations that were derived for extracting ground movement from the two non-parallel passes can, in general, be used to derive two dimensional ground movement. In principle, only one component of the displacement vector can be obtained from a single interferometric pair of similar viewing geometry. To measure three components of displacement, one must have three sets of interferometric pairs, each of which have different look

directions, unless additional information (e.g., from ground observations) are available to determine the full three-dimensional displacement field. To extract the third component of movement, assumptions have to be made in the absence of a third differential interferogram with unique look direction. With satellite interferometry, it is not possible to obtain this third unique pair. However, under certain conditions it may be possible to estimate three dimensional ground movement using least squares techniques. These conditions include regions experiencing well-behaved ground movement, in which the movement is generally homogeneous over many resolution cells of the SAR sensor.

With reference to Figure 3-10, consider a small area on the ground viewed by a varying incidence angle ϑ to $\vartheta+\Delta\vartheta$ over which the surface change is a small-scale coherent change common to several adjacent pixels. In other words, the deformation is well behaved with no discontinuities. With this assumption, the under-determined system in equation (3-18) can be restructured into an over-determined system for pixels within the region bounded by $(\vartheta, \vartheta+\Delta\vartheta)$. Consider n pixels in that neighborhood where the position of the radar scatter has not changed substantially; however, the ensemble of the scatter has moved up, down, or sideways in some correlated fashion. This implies that an area on the ground experienced homogenous movement and can be collectively grouped by those n pixels.

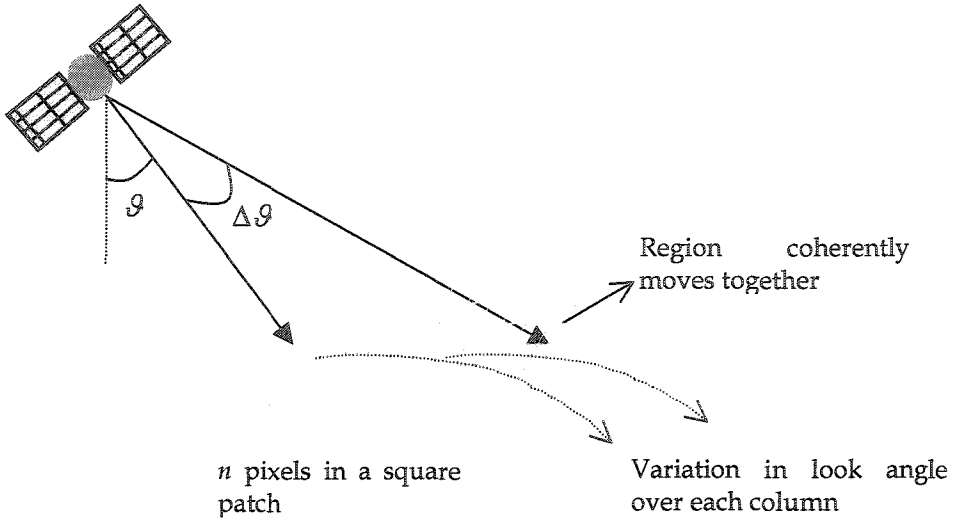

Figure 3-10: Bounded region of n pixels that coherently move together

For the i^{th} pixel in that n pixel region (Figure 3-10), the 3-D movement Δx_i, Δy_i and Δz_i can now be estimated. The conversion matrix for each pixel i is given as

$$\begin{bmatrix} -\sin(\vartheta_{d_i})\cos(\varphi_d) & \sin(\vartheta_{d_i})\sin(\varphi_d) & \cos(\vartheta_{d_i}) \\ -\sin(\vartheta_{a_i})\cos(\varphi_a) & -\sin(\vartheta_{a_i})\sin(\varphi_a) & \cos(\vartheta_{a_i}) \end{bmatrix} \cdot \begin{bmatrix} \Delta x_i \\ \Delta y_i \\ \Delta z_i \end{bmatrix} = \begin{bmatrix} \Delta\rho_{d_i} \\ \Delta\rho_{a_i} \end{bmatrix}, \qquad (3\text{-}19)$$

The least squares solution for the system of equations in (3-19) can be represented as $\mathbf{MX} = \mathbf{b}$ where $\mathbf{M}$ is the system matrix,

$$\mathbf{X} = \begin{bmatrix} \Delta x \\ \Delta y \\ \Delta z \end{bmatrix} \text{ and } \mathbf{b} = \begin{bmatrix} \Delta\rho_d \\ \Delta\rho_a \end{bmatrix}.$$

The least squares solution of $\mathbf{X}$ is such that the size of the residual vector is minimal. The over-determined system of equations permits a solution for each Δx_i, Δy_i and Δz_i; however, as discussed in Section 3.2, meaningful measurements

might only be obtained from Δx_i and Δz_i. The reason is due to the imaging geometry of the SAR satellite (Figure 3-10) whereby the slant range change (SRC) is relatively insensitive to changes in the y direction compared to x and z directions. As a consequence, the measurement error of the SAR sensor may be greater than that of the measured Δy (North-South) movement, except in the case of substantial lateral movement. Averaging many interferograms might reduce the measurement errors sufficiently to allow reasonable estimates in the y direction.

The grid for the over determined system of equations with overlapping ascending and descending pass images is illustrated in Figure 3-11. The variation of ϑ_{a_i} and ϑ_{d_i} over a small area on the ground is insignificant. Therefore a relatively large area has to be chosen to provide a meaningful result from the least squares estimation. The rationale for this is based on the convergence of a least squares solution. However, it also reduces the likelihood of having a region of homogeneous ground movement with no discontinuities. To mitigate these potential problems, an optimization routine can be employed to determine the region of most suitable size. This can be achieved by varying the size of n (number of pixel as a variable) pixel neighborhood as shown in Figure 3-11 to estimate subsidence movement using any one of the two differential interferogram (either ascending or descending) until a satisfactory

level of correlation is achieved when compared with data obtained from the global positioning systems (GPS). By doing this, a number of homogeneous ground movement pixels can be estimated for the region under investigation. This number can then be used for the least squares solution to estimate ground movement in 3-D.

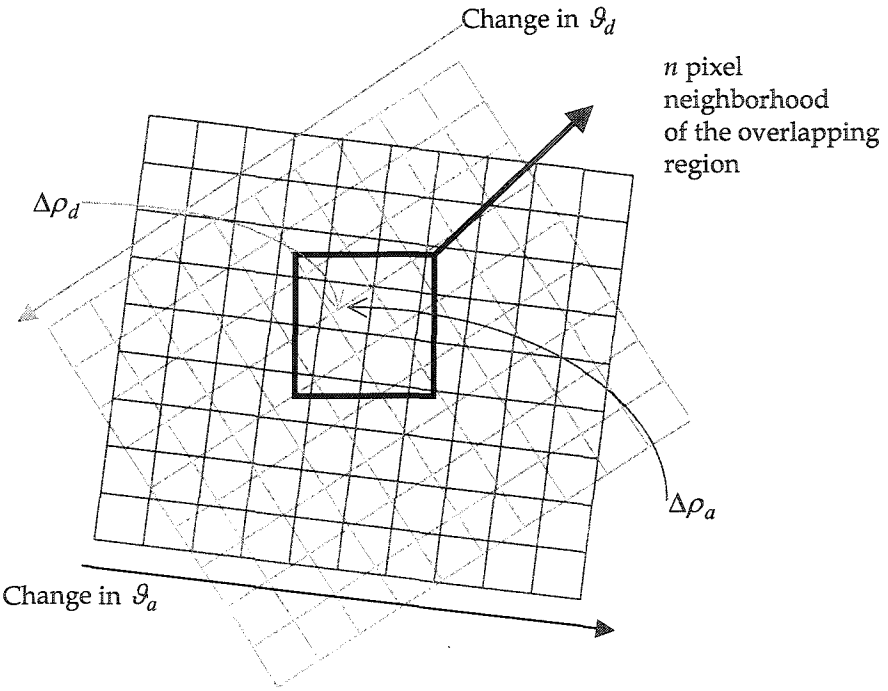

Figure 3-11: Ascending and descending pass grid with varying incidence angle. The n neighborhood identifies region of continuous displacement field used for the least-squares solution.

In summary, this chapter has derived a technique to estimate 3D ground movement from DInSAR by fusing ascending and descending pass images. It has also illustrated the difficulty in extracting 3D ground movement vectors from only two look directions. If any of the movement components are known a

priori, then the other two components can be easily estimated except for the lack of sensitivity in the north-south direction. With a homogeneous ground movement assumption, mathematical modeling techniques were derived to estimate the three unknowns. The verification of the proposed method is explored in the following chapter, which illustrates and explains the rationale of each verification step and resolves issues with the results as encountered. In this chapter a test region is used to illustrate the validity of the movement measurement technique by comparing DInSAR derived movements with in-situ measurements.

Chapter 4

Verification and Results

The previous chapter has outlined a technique to extract 3D ground movement by fusing data from two satellite look directions. A least squares technique was proposed, aided with a uniform ground movement assumption. To verify the derived method and to validate the technique, an area with known and measured ground movement should be used. This is the subject of the present chapter.

Based on historical surveys, the North Belridge Oil Field located in San Joaquin Valley in southern California is known to be experiencing significant ground movement due to oil production [49]. This ground movement has resulted in significant problems for companies operating in the region. For example, one gas pipeline company has experienced several ruptures to a pipeline that runs directly through the subsiding region. The failure modes of

this pipeline have generally been in a lateral direction (Figure 4-1), hence the rationale for seeking to accurately measure lateral movement with DInSAR.

Figure 4-1: Pipeline failure due to lateral ground movement. (Courtesy of Southern California Gas Company and C-CORE)

To measure this movement, GPS surveys were made of 65 monuments scattered throughout the region, which is illustrated in Figure 4-2. The area of coverage for this survey was approximately 10km^2 where measurements from these 65 monuments were recorded by Southern California Gas Company (SoCal Gas).

SoCal Gas provided a total of ten surveys for this DInSAR research, including six surveys in 2000 and four surveys in 2001.

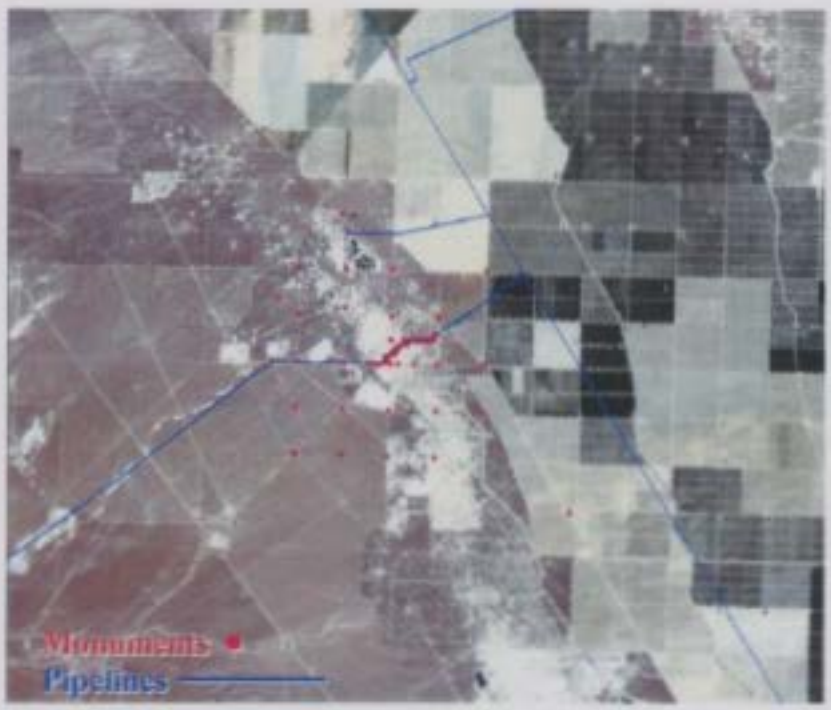

Figure 4-2: GPS monument position along the pipeline vector

The recording of these GPS surveys was not periodic and there were instances when the interval of readings exceeded many months. To normalize these inconsistencies in the GPS survey, standard slope fitting techniques were used to estimate a general movement trend for each monument from the GPS measured data set. These data were used to validate ground movement data derived from a series of SAR images using DInSAR and the techniques discussed in Chapter 3.

The DEM required to remove topographical information with the DInSAR technique was obtained from a tandem mode ERS-1 and ERS-2 pair. The time interval between interferometric acquisitions of ERS-1/2 is only one

day and is suitable for DEM generation, since phase decorrelation due to changes in the scattering properties of the ground is limited over that period. The interferogram shown in Figure 4-3 is obtained after processing the ERS-1/2 interferometric pair, which contains the topographical information.

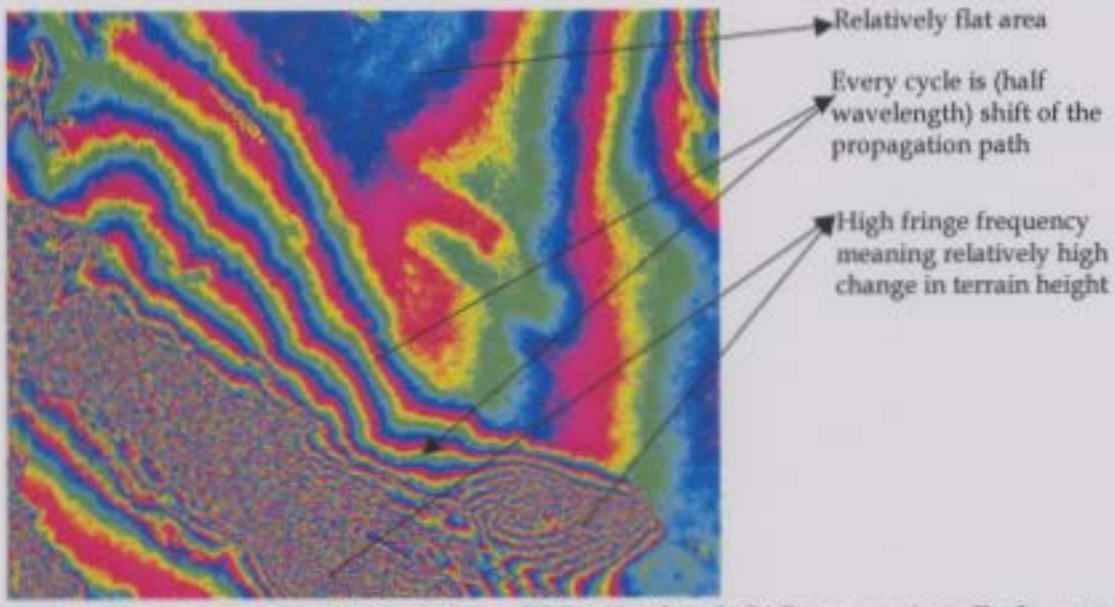

Figure 4-3: Interferogram obtained from ERS-1/2 after InSAR processing. Each contour line represents 28mm (i.e. half of the radar wavelength).

Figure 4-4 is the corresponding DEM for the interferogram shown in Figure 4-3.

Figure 4-4: DEM from ERS-1/2 after InSAR processing.

RADARSAT ascending and descending scenes were obtained over a 7-month period during 2001 for the validation. The area of interest containing the 65 monuments is well contained by the coverage of RADARSAT Fine Mode (~ 8m resolution of 50 km by 50 km). Table 4-1 lists all the images used for validating the fusion method, including both ascending and descending passes. Interferograms were derived for each of the 8 pairs. All pairs exhibited excellent coherence, thus DInSAR results were expected to be of very good quality.

Interferogram Pairing order.	Orbit		Date of Acquisition
1	27662	Ascending	February 21st 2001
2	28348	Ascending	April 10th 2001
3	29377	Ascending	June 21st 2001
4	30406	Ascending	September 1st 2001
	30749	Ascending	September 25th 2001
5	27726	Descending	February 25th 2001
6	28412	Descending	April 14th 2001
7	29441	Descending	June 25th 2001
8	30470	Descending	September 5th 2001
	30813	Descending	September 29th 2001

- Interferogram pairing [1&5, 2&6, 3&7, 4&8] as the D-InSAR Fusion Pairs.
- Dem was generated from ERS-1/2.
- ERS-1 ORBIT=22517-FRAME=2891, November 4th 1995
- ERS-2 ORBIT=02844-FRAME=2891, November 5th 1995

Table 4-1: Satellite orbit and data processed for differential interferometry

Two examples of differential interferograms (only displacement fringes with removed topographical fringe contribution) for ascending and descending passes are shown in Figure 4-5 and Figure 4-6.

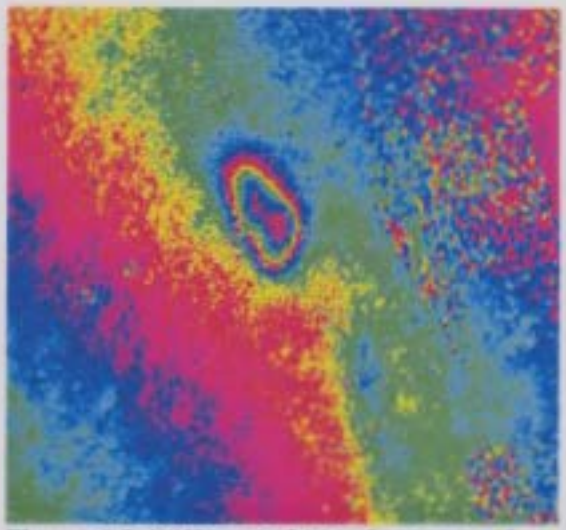

Figure 4-5: Differential interferogram of 30470 and 30813 Descending pass from RADARSAT-1

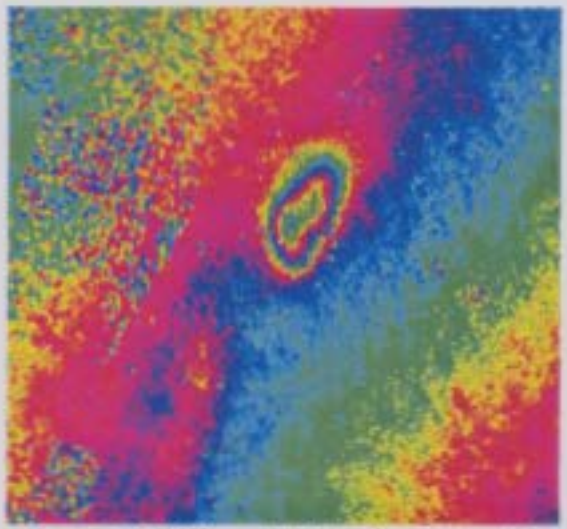

Figure 4-6: Differential interferogram of 30406 and 30749 Ascending pass from RADARSAT-1

Linear trends on the interferogram are often manifested due to inaccurate satellite orbit parameters and atmospheric pressure variations [50]. Figure 4-5 is a zoomed interferogram, focusing on the area of ground movement shown in Figure 4-7. Figure 4-7 shows slant-range change processed for the image pair 7 and 8 listed in Table 4-1. Non-uniform contrast variation can be observed on the left hand image of Figure 4-7 starting from the bottom left corner (bright) to the top right corner (dark). This implies the presence of a uniform slope in the image scene on the left hand side of Figure 4-7. However, there is no such slope in reality and the area is known stable from the geographic location of the scene. Thus, it is quite obvious that the evidence of this slope may have been introduced due to the satellite imaging system and must be removed. This can be achieved by sampling points around the fringe ellipse as seen in Figure 4-7. This is done by multiple regressions to fit a trend plane and remove that from the

scene. In this case, a two-dimensional regression model is used to estimate the best plane that can be fitted with sampled data points around the region of maximum displacement from the differential interferogram. The resultant residue image as shown in the right hand image of Figure 4-7 is the differential slant-range change and is a result of ground movement only.

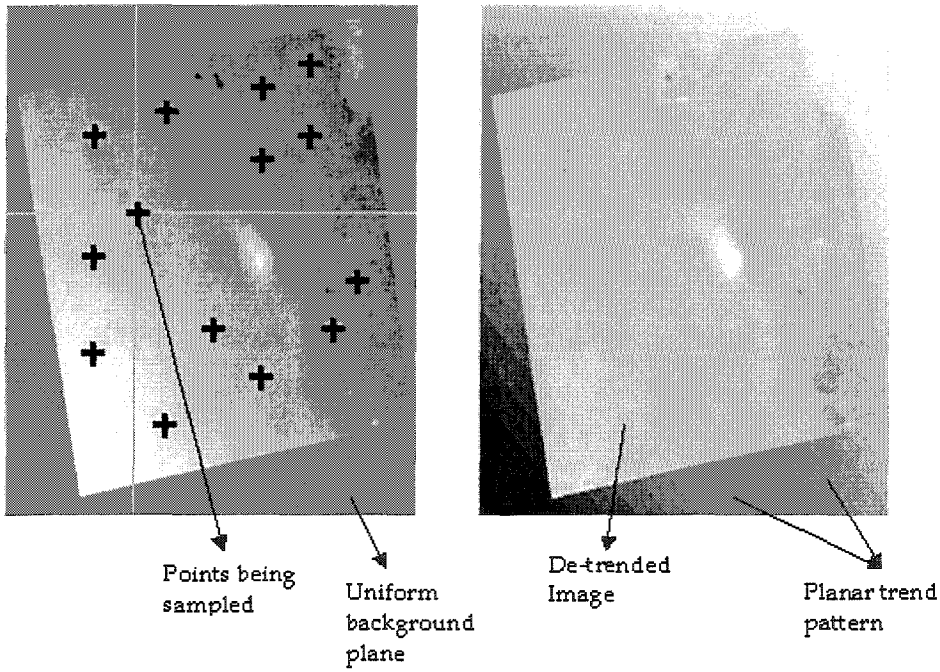

Figure 4-7: Figure on the left is with a planar trend and the figure on the right is after removing the planar trend.

4.1 Comparison of GPS Measurements Projected onto SAR LOS

The measurements of ground position via global positioning satellites or GPS is a popular and convenient method for measuring ground movement. Although it does not achieve the same accuracy as a rigorous theodolite-derived

survey, differential GPS measurements with a fixed and moving station can achieve reasonably accurate positional estimates. The accuracy of these estimates increases with the amount of time the roving station collects its data at a single point and accuracies of 1-2 cm in x, y and 2-5 cm in z are achieved respectively if data are collected for greater than 20 minutes or so.

The GPS readings that were collected at the ground station monuments were measured with the standard rover/base station system. Each survey was captured over a two day period, and measurements were generally taken at each monument for only a few minutes. As a consequence, the GPS measurements are only expected to have accuracies on the order of 5 cm. Since the accuracy of DInSAR measurements is on the order of 5 mm or so, the DInSAR measurements were instead compared with linear trends of movement at each GPS monument. Assuming a linear trend of movement, the GPS measurements were fitted with a regression line to extract the movement trend. The survey of ground movement taken over year 2000 and 2001, revealed a standard deviation of 0.75 cm in East-West, 0.86 cm in North-South and 1.56 cm in subsidence of the GPS points about the regression line for the 65 monuments. This indicates that GPS measurements cannot be directly compared with that of InSAR, since GPS measurements themselves contain errors. However, the GPS *trends* have accuracies that are much more favorable to DInSAR comparison and the results presented here will confirm that this is indeed the case.

The first validation that was conducted involved a comparison of the GPS trends with the DInSAR Line of Sight (LOS) measurements. This comparison was performed to determine if, in fact, the satellite slant range change measurements after SAR and InSAR processing are correct. To perform this comparison, the measurements of each GPS monument were projected onto the SAR look directions. The existence of a tight linear trend of GPS and DInSAR should validate the SAR line of sight measurements of the satellite and should compare favorably with industry accepted in-situ measurements. Each GPS monument reading is denoted as

$$\mathbf{G}_j = gps_{x_j} \cdot \hat{x} + gps_{y_j} \cdot \hat{y} + gps_{z_j} \cdot \hat{z}\,, \tag{4-1}$$

where $\mathbf{G}_j$ is the movement at the j^{th} monument. For the descending pass geometry, the satellite look direction at the j^{th} GPS monument is in the direction $\mathbf{D}_j$. Thus, the projection of the GPS measured movement vector $\mathbf{G}_j$ onto the descending pass geometry can now be represented as per equation 3-18 as

$$\mathbf{G}_j \cdot \hat{D}_j = -\sin(\vartheta_{d_j})\cos(\varphi_d).gps_{x_j} + \sin(\vartheta_{d_j})\sin(\varphi_d).gps_{y_j} + \cos(\vartheta_{d_j}).gps_{z_j} \tag{4-2}$$

Similarly, the LOS projected component of $\mathbf{G}_j$ for ascending pass geometry can be expressed as

$$\mathbf{G}_j \cdot \hat{A}_j = -\sin(\vartheta_{a_j})\cos(\varphi_a).gps_{x_j} - \sin(\vartheta_{a_j})\sin(\varphi_a).gps_{y_j} + \cos(\vartheta_{a_j}).gps_{z_j} \tag{4-3}$$

A comparison of DInSAR and projected GPS was performed for each of the 8 DInSAR pairs. The GPS movement measurements were normalized (movement per day translated to movement in 24 days, which is one RADARSAT-1 cycle) to the same time period of each DInSAR pair, so that a perfect correlation would have a slope of unity. Figures 4-8 and 4-9 give examples of the correlation for ascending and descending passes for one pair set (interferogram pairing order 1 and 5 of Table 4-1) from February to April 2001. Figure 4-10 and 4-11 shows the average of all four pairs of SAR data acquired for both passes from February 2001 to September 2001 compared to GPS measurements projected on the SAR look direction. These plots show an excellent correlation of 98% and 97%, which is improved over the single DInSAR measurements with correlation of 89% and 90% in Figures 4-8 and 4-9. Note that the slopes of each of the Figures from 4-8 to 4-11 as shown below are close to unity.

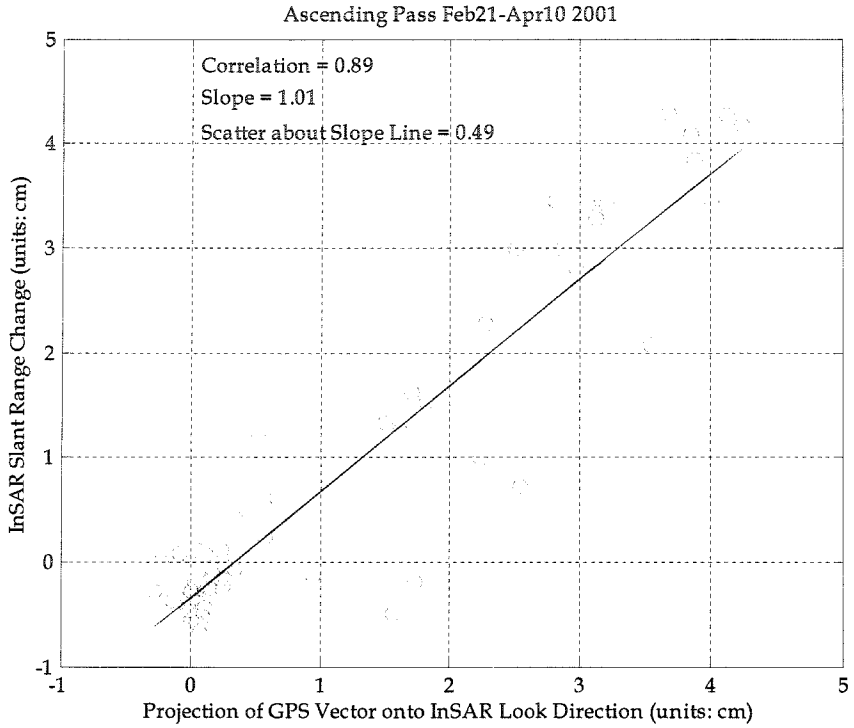

Figure 4-8: InSAR SRC (cm) versus $\mathbf{G} \cdot \hat{A}$ [Feb-Apr 2001]

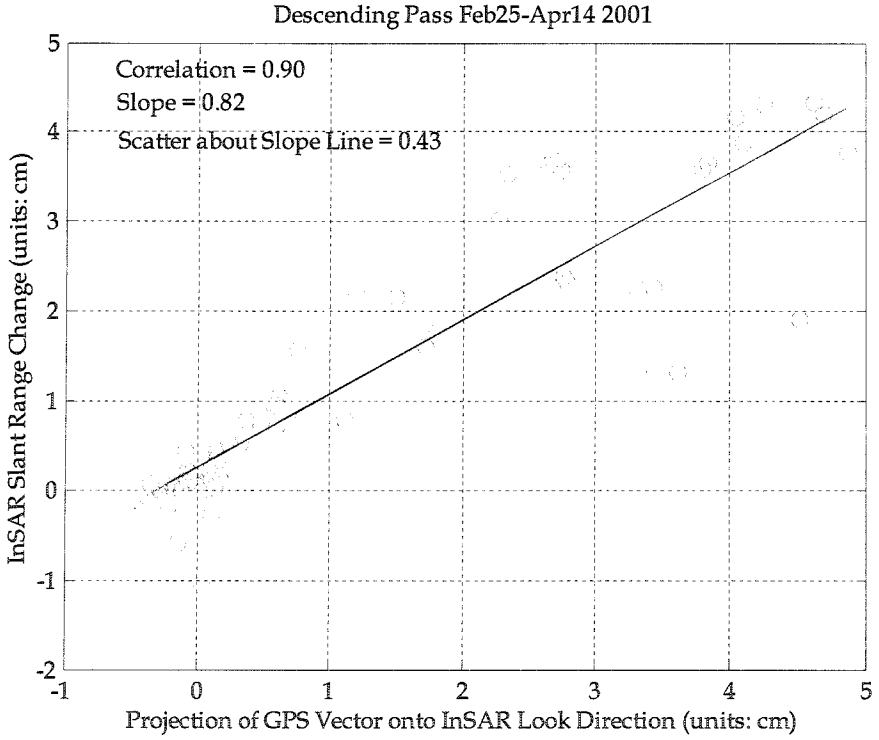

Figure 4-9: InSAR SRC (cm) versus $\mathbf{G} \cdot \hat{D}$ [Feb-Apr 2001]

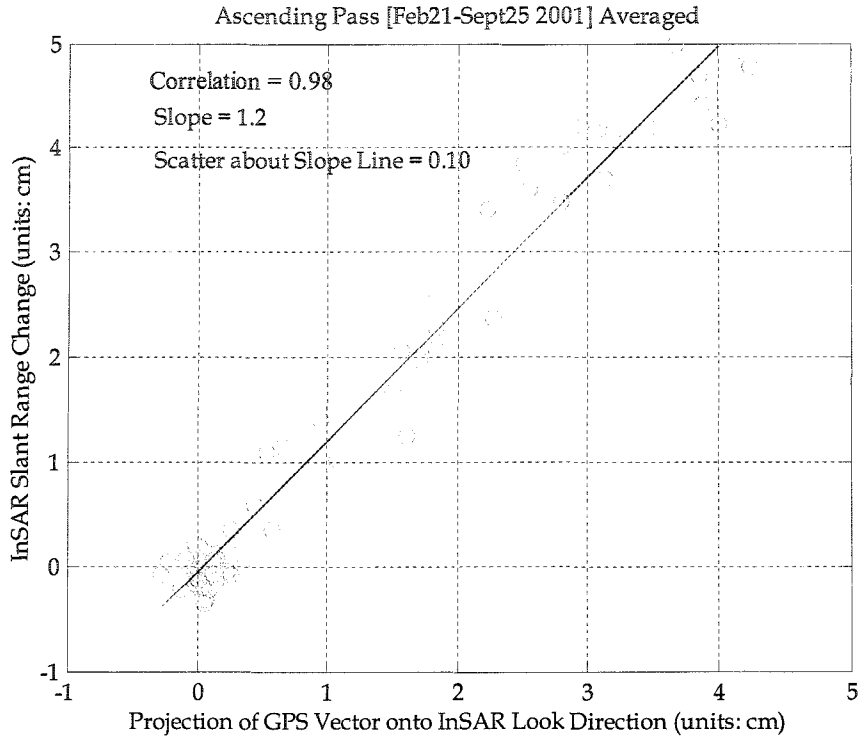

Figure 4-10: InSAR SRC (cm) versus $\mathbf{G} \cdot \hat{A}$ [Averaged Feb-Sept 2001]

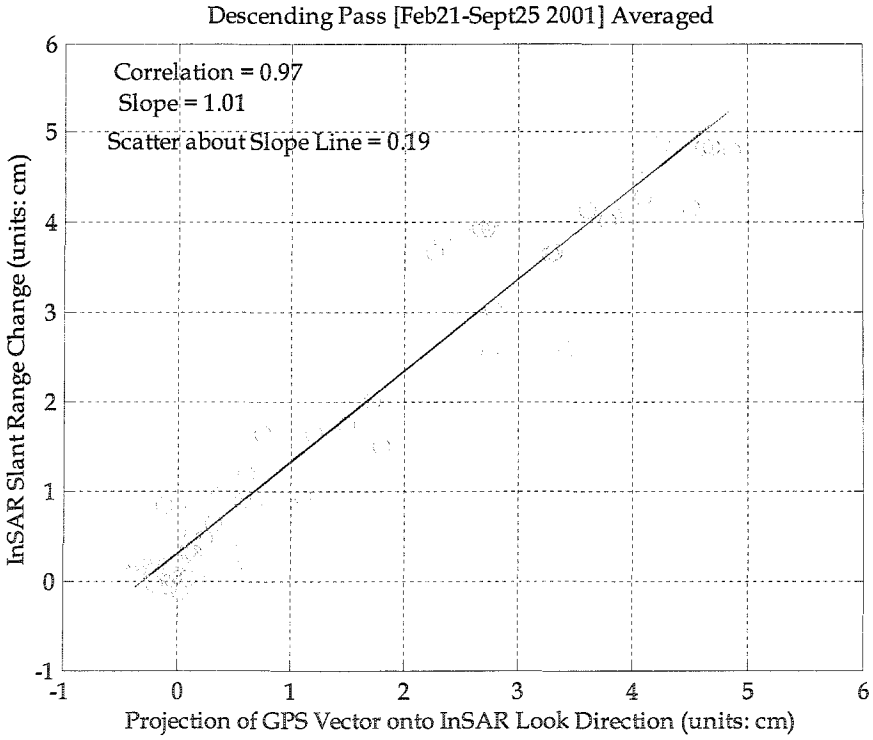

Figure 4-11: InSAR SRC (cm) versus $\mathbf{G} \cdot \hat{D}$ [Averaged Feb-Sept 2001]

The two plots in Figure 4-10 and 4-11 show a strong positive correlation and indicate the trend achieved with all eight pairs (4 descending pair and 4 ascending pair). This validates that averaging DInSAR measurements over a series of interferograms will reduce the measurement error of the sensor to provide a more accurate movement estimate. Appendix A contains the remaining plots, Figures A1 to A6 for rest of the DInSAR pairs.

4.2 Validation of 2-D Ground Movement

To properly verify the fusion technique presented here to estimate lateral ground movement, a region experiencing significant lateral ground movement is required. This can be verified by examining companion ascending and descending pass interferograms. Specifically a difference in slant range change between ascending and descending pass differential interferograms that is greater than the sensor measurement error (~ 5 mm) for some incidence angle indicates that lateral ground movement has been detected. Conversely, if the SRC measurements of the companion ascending and descending pass interferograms are equal, this indicates that only a vertical (z direction) movement was measured. For the series of interferograms used here, the presence of lateral movement as discussed earlier via Figure 1-2, can be confirmed by plotting the ascending/descending SRC difference at each of the

ground station monuments as shown in Figure 4-12. The ground station monument positions were obtained by sampling at the correct latitude/longitude from the interferogram for the locations of the GPS survey. Figure 4-12 shows SRC differences in excess of 10 mm for a substantial number of ground station monuments in each of the interferograms.

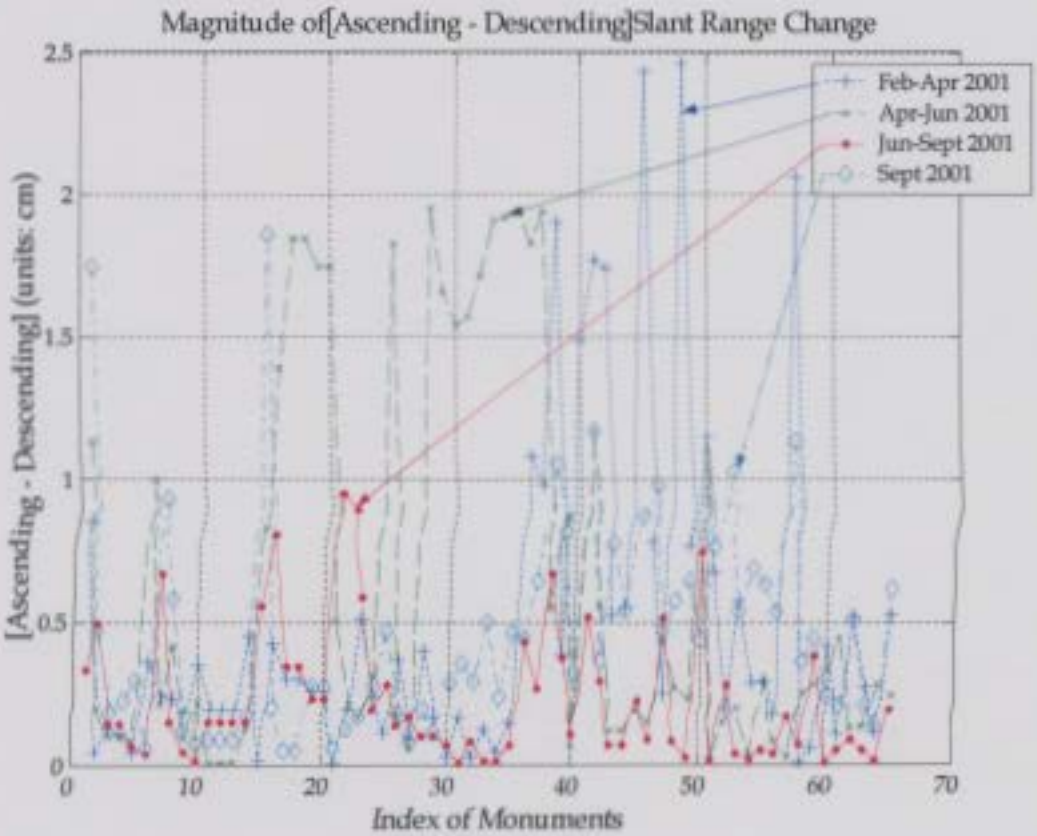

Figure 4-12: Variation over time in SRC (cm) between Ascending pass and Descending pass.

This phenomenon can be confirmed by inspecting ascending and descending pass geometry (cf. Figures 3-6 and 3-7). Had the ground movement been only vertical then the measured SRC vectors **A** and **D** should be the same in magnitude. Alternatively, the magnitude of **A** and **D** will be different if there

are displacements other than subsidence. From Figure 4-12, taking the absolute difference of SRC from ascending and descending passes shows the magnitude of lateral movement that can be expected over the region of interest. One can conclude that for example $|A| > |D|$ the lateral movement is generally eastward. Conversely, for example for $|D| > |A|$ one can conclude that the magnitude of lateral movement is generally westwards. Figure 4-12 shows the absolute magnitude of lateral movement in the region under investigation.

According to the processing steps and necessary equations developed in previous sections, the subsidence and lateral movement were derived from each of the interferograms. The first technique that was attempted was a 2D movement estimate, whereby the movement in one direction was assumed to be known to allow estimation of the other two directions. Since satellite DInSAR is more sensitive to East-West (x) and Subsidence (z) movements, the North-South (y) movement was arbitrarily set to zero. The technique was applied to each of the 8 DInSAR pairs. The result for a single DInSAR pair and an overall average of all 8 pairs is provided in Figures 4-13 to 4-16. Figures 4-13 and 4-14 are comparisons of 2-D ground movement from February to April 2001 (48 days, which is 2 RADARSAT-1 cycles) from DInSAR with respect to GPS derived movement trends, both normalized (movement per day translated to one RADARSAT-1 cycle) to 24 days.

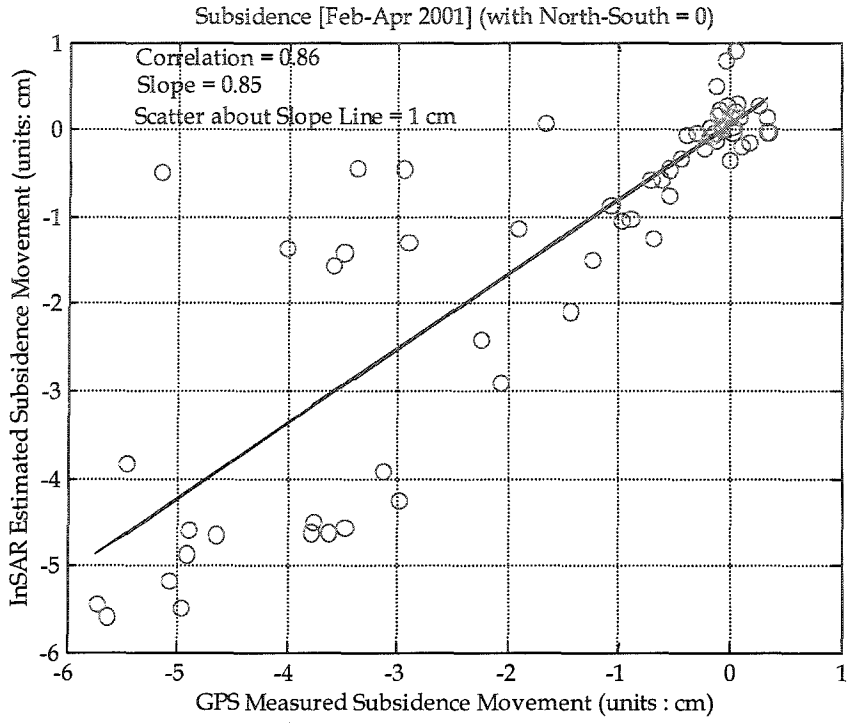

Figure 4-13: InSAR versus GPS subsidence normalized to 24 days from February -April 2001

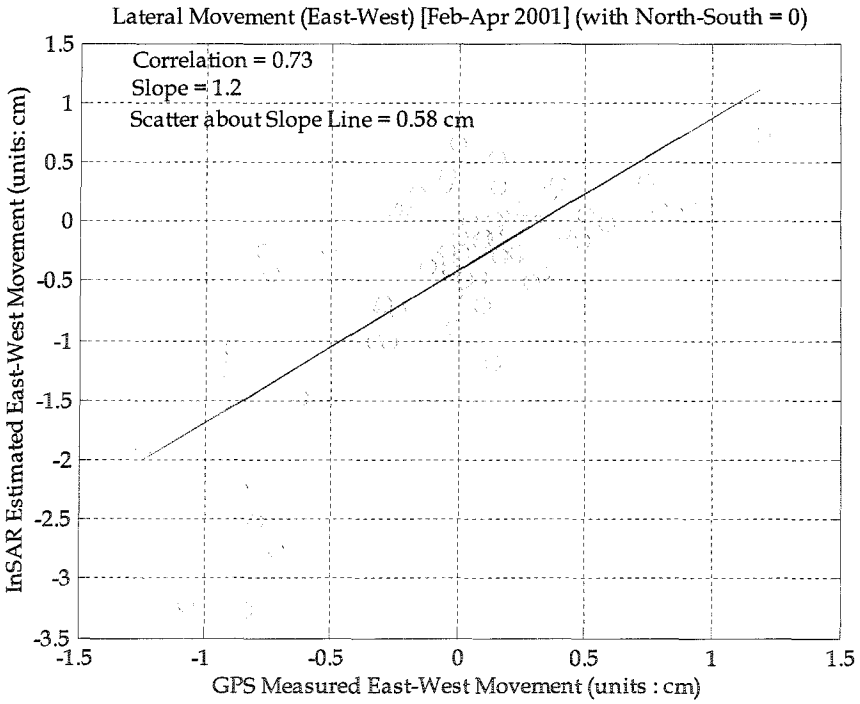

Figure 4-14: InSAR versus GPS East-West movement normalized to 24 days from February - April 2001.

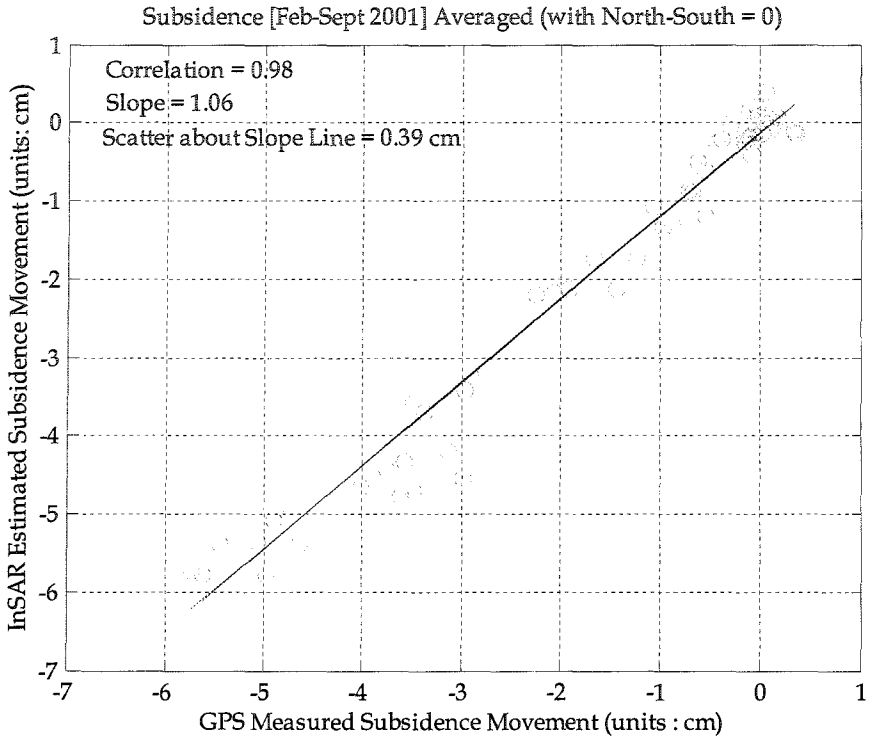

Figure 4-15: InSAR versus GPS subsidence normalized to 24 days averaged over 4 DInSAR pairs from February - September 2001.

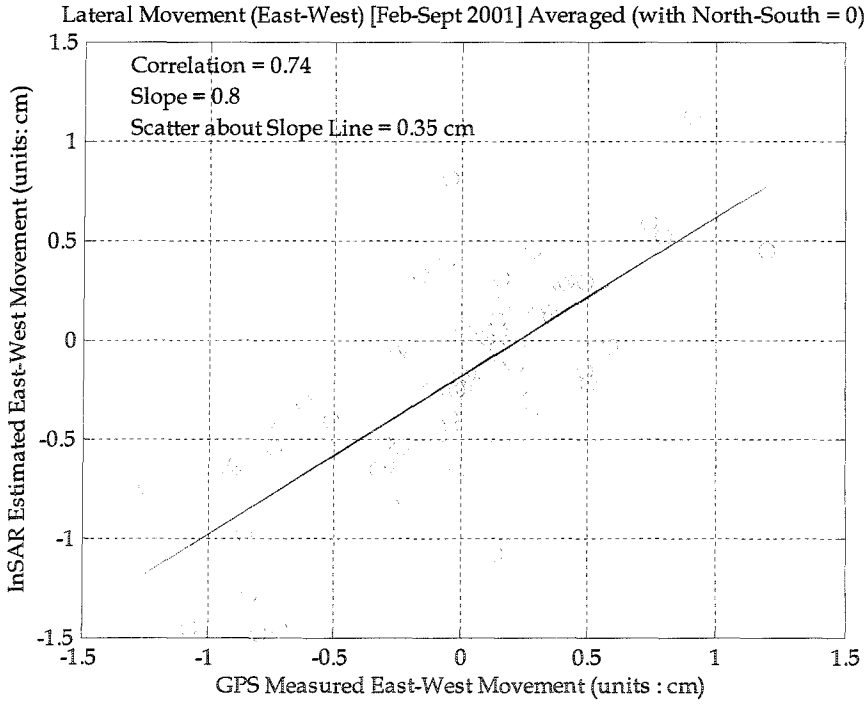

Figure 4-16: InSAR versus GPS East-West movement normalized to 24 days averaged over 4 DInSAR pairs from February - September 2001.

Figure 4-15 and 4-16 are comparisons of 2-D ground movement from February to September 2001 from DInSAR with respect to GPS derived movements normalized to 24 days. DInSAR pairs from February to September 2001 were obtained by processing each differential pair from the list of images shown in Table 4-1 and then averaged. These plots illustrate the following:

1. Subsidence and East-West movements derived from DInSAR correlate very favorably to GPS.
2. Subsidence estimates appear to correlate more favorably than East-West measurements.
3. The average variance (scatter of the data) from the trend line achieved in subsidence and East-West movement for an individual interferogram is [1 and 0.58] cm while the overall variance (from the trend line) in subsidence and East-West movement is [0.39 and 0.35] cm, respectively.

These results are very encouraging and the achieved accuracies may be sufficient for many applications. However, for this case study, it was known that many of the 65 GPS monuments were taken along a line that runs East-West through the region of greatest ground movement. Consequently, many of the monuments experienced more East-West movement than North-South.

The results may not have been as favorable if substantially higher North-South movement was experienced at these monuments, making the assumption

of $\Delta y = 0$ to be invalid. A more robust approach would involve no prior assumptions of movement. As will be shown, the previously presented technique employing least squares estimation, *instead* of the $\Delta y = 0$ assumption, produces improved subsidence and lateral movement estimates and thus, in general, is a better overall technique.

4.3 Simulation with Synthetic Data

To validate the ground displacement estimation method using the least squares technique, an artificial ground movement model was created. The objective is to verify estimated ground movement in each direction using artificially created SRC data for two look directions (ascending and descending). The simulated ground movement data were modeled after the ground displacement occurring in the San Joaquin Valley, which is the field location of the satellite and GPS data collection that will be presented later. Consequently, a direct comparison can be made between the simulated and measured results.

4.3.1 Derivation of Synthetic Data

The San Joaquin Valley site is experiencing localized subsidence that is spatially shaped like a "bowl" of movement. The maximum subsidence occurs roughly in the middle and gradually drops off in a radial direction to a point of

negligible subsidence at some maximum radius. The simulated movement model was created to emulate the one observed in Figure B-4 in appendix B, and is given in Figure 4-17.

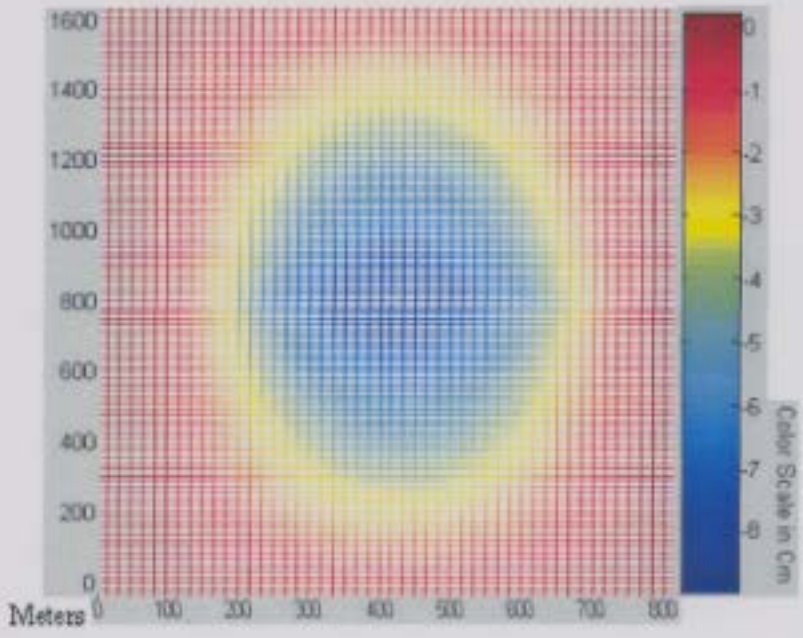

Figure 4-17: The simulated Subsidence movement.

The corresponding lateral movement is modeled from the subsidence by examining the *rate of change* of subsidence ground movement. The location of maximum lateral movement is where the "slope" of the subsidence pattern is maximum. Therefore, lateral movement is inferred to be zero at the center of the "bowl" at the point of maximum subsidence and also at the outer perimeter of the bowl. The point of maximum lateral movement occurs at the middle point between the center and the outer perimeter of the bowl, simulating where the sides of the bowl will "cave-in" towards the center. The direction of this "cave-in" indicates the proportion of the movement that is North-South and East-West.

The simulated lateral movements that emulate this behavior are shown in Figures 4-18 and 4-19.

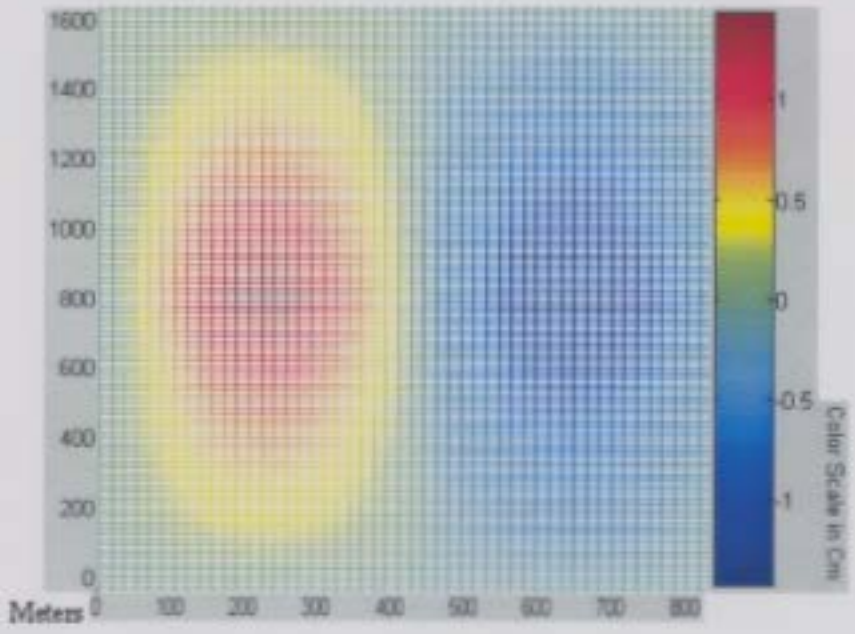

Figure 4-18: Illustrates the East-West movement

The subsidence movement was simulated using a Blackman window, which is *"bowl shaped"*. If the lateral movement is then *"inferred"* from the rate of change of subsidence, taking the derivative of the Blackman window will produce the desired lateral movement magnitude. If the lateral movement direction is inferred as the radial direction to the center of the subsidence "bowl", both East-West and North-South movements can be thus derived. Using this model, the lateral movement can be simulated using two raised cosines equally spaced and opposite in direction and tapered at the ends to simulate East-West and North-South movements. The movements have been scaled to be on the same order as the actual San Joaquin Valley movement.

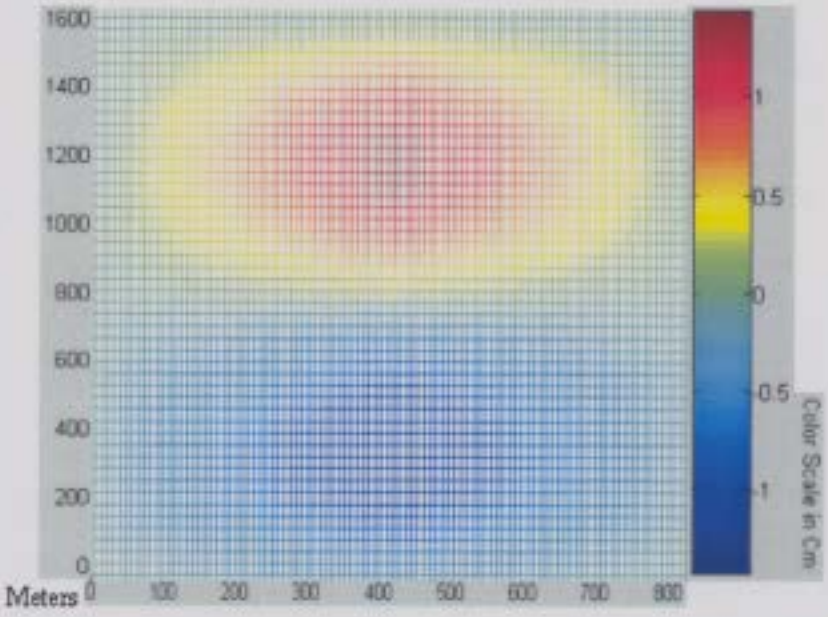

Figure 4-19: Illustrates the North-South movement

From these three sets of synthetic movement data, appropriate slant range change (SRC) data for both ascending and descending passes were generated. This can be achieved by projecting the movement vectors to satellite look directions. Thus, two artificial SRC (descending/ascending) data sets were generated by combining the synthetic movements using equation 3-16 and 3-17. Figure 4-20 illustrates one such SRC dataset for the ascending pass.

Ground movement estimates were derived using the two SRC data (ascending/ descending pass) and with the aid of equations derived in Section 3.3. The estimated ground movement was then compared with the simulated movement data. In doing this, the accuracies of the 3-D ground movement estimation model can be verified. The verification results with artificial data will indicate the maximum accuracy that can be achieved in practice.

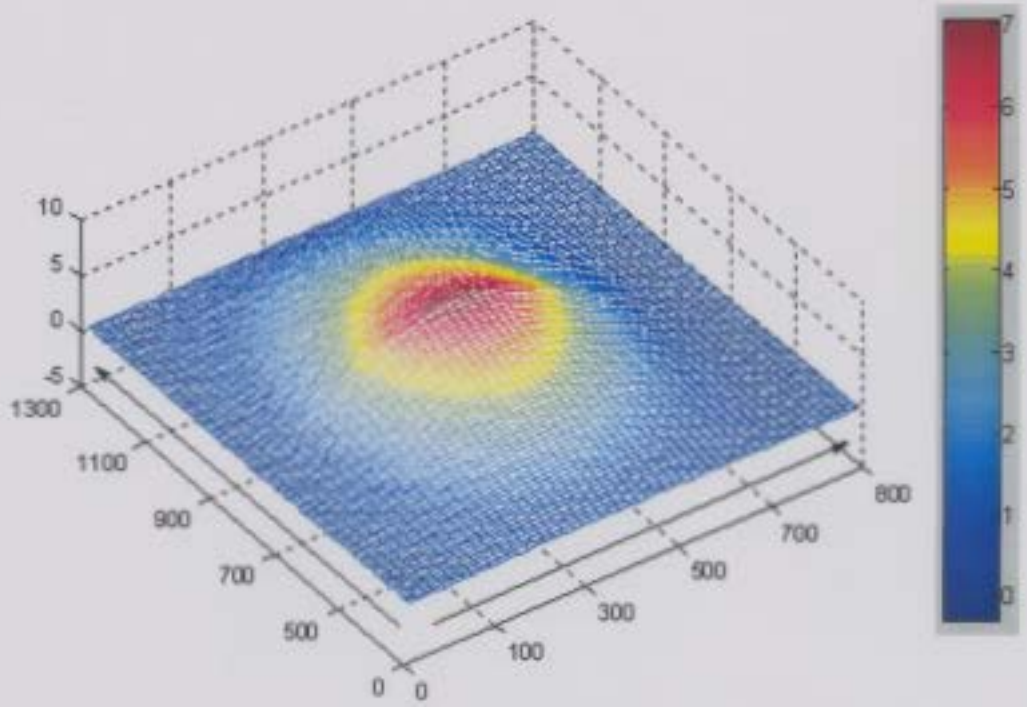

Figure 4-20: Slant Range Change data for ascending pass. (Artificially created from individual East-West, North-South and Subsidence data. SRC shown as positive here in the plot.)

4.3.2 Movement Components Derived from Simulated Data

The GPS survey that was conducted in the San Joaquin Valley site was conducted mainly along the pipeline right-of-way (ROW), which runs generally along an East to West direction. The movement experienced along this line is predominantly East-West and subsidence because the ROW coincidentally runs through the point of maximum movement. In addition to the ROW monuments, there was a coarse grid of monuments that were equally spaced around the region of ground movement, the majority of which fell into non-moving regions. As a consequence, the majority of the moving monuments experienced predominantly East-West and Subsidence movement, and North-South

movement was only minor in most cases. This presented some difficulty in verifying the North-South satellite estimates from the satellite imaging geometry because the actual North-South movement projected onto the satellite look direction was comparable to the sensor error. Figure 4-21 illustrates sampled GPS monument positions that were obtained by the survey.

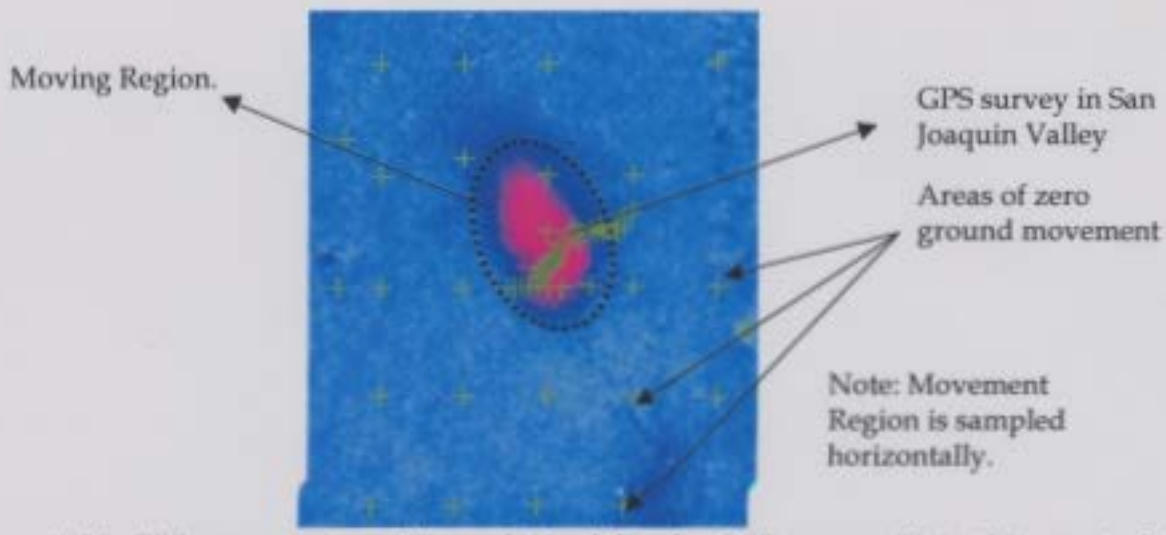

Figure 4-21: GPS monument positions obtained by the GPS survey. Note that most of the monument positions inside the dotted ellipse shown as area of movement are mainly on the horizontal (East-West direction).

The comparison between the simulated movement and estimated movement from the simulated SAR plots are shown in several forms, as detailed below:

1. To emulate the GPS monument positions along the pipeline ROW, the simulated data were sampled horizontally along the center of the data through the maximum subsidence location.
2. To determine the algorithm's performance in the region of maximum North-South movement the simulated data were sampled vertically

along the center of the data through the region of maximum subsidence.

3. To determine the overall performance, the simulated data were sampled with a uniform grid, both vertically and horizontally.

Results from each of these cases will be considered individually. Firstly, consider the case when monument position is sampled along the horizontal line. Figure 4-22 illustrates the position of these monuments that are used for the subsidence estimates.

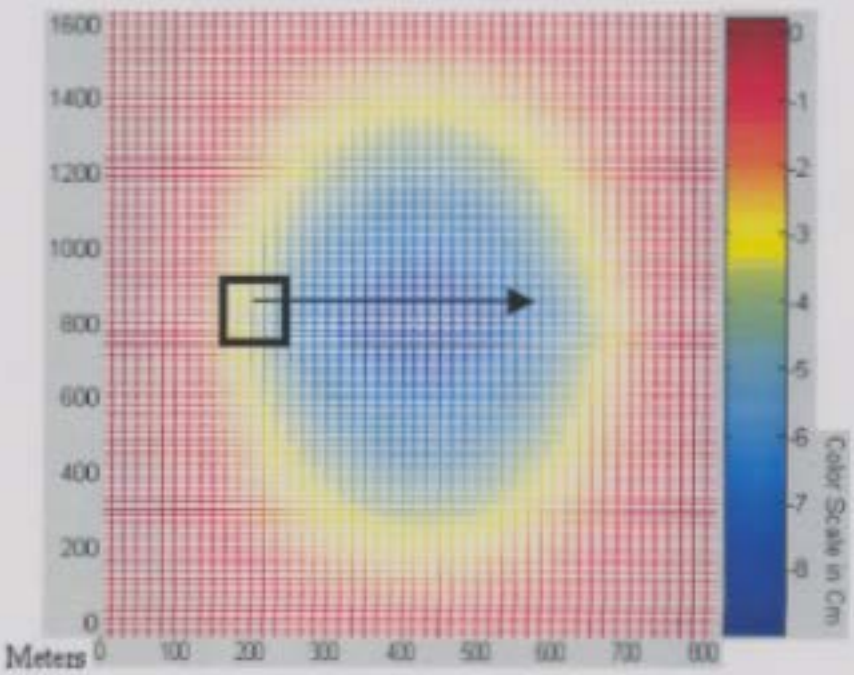

Figure 4-22: Monuments sampled horizontally as shown by the arrow

The plots shown in Figures 4-23, 4-24 and 4-25 depict the solution of the least squares estimates compared with synthetic data sampled along the horizontal line.

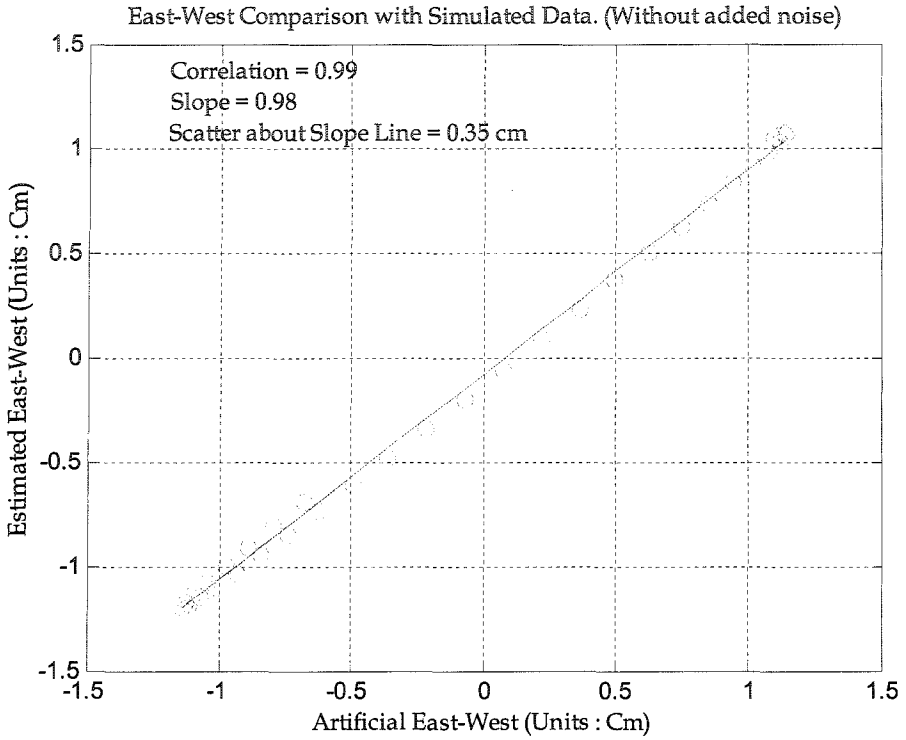

Figure 4-23: Comparison of East-West movement sampled horizontally

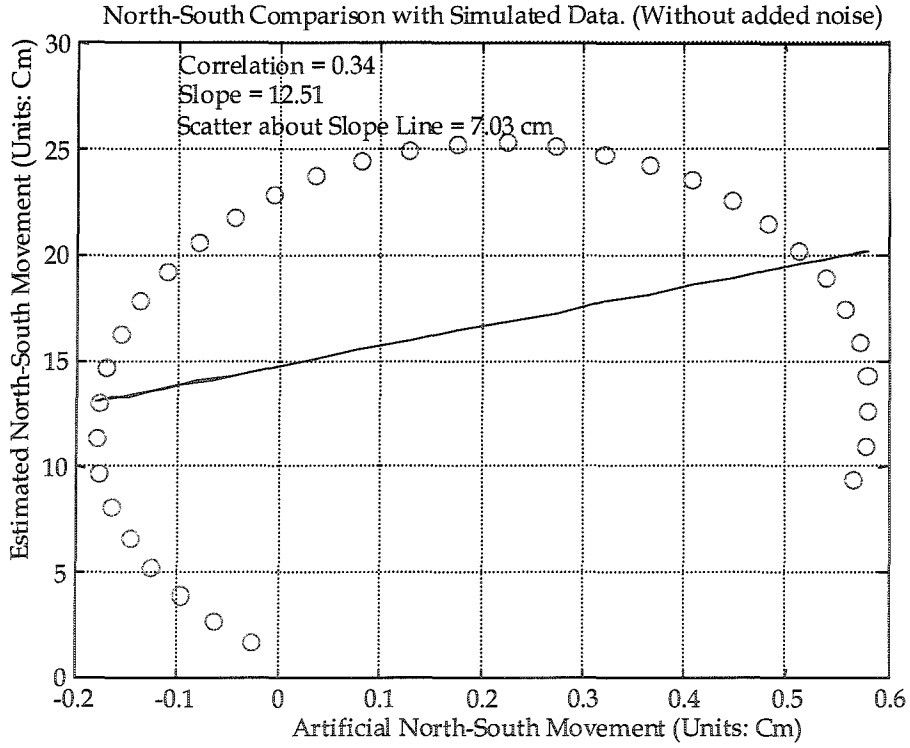

Figure 4-24: Comparison of North-South movement sampled horizontally

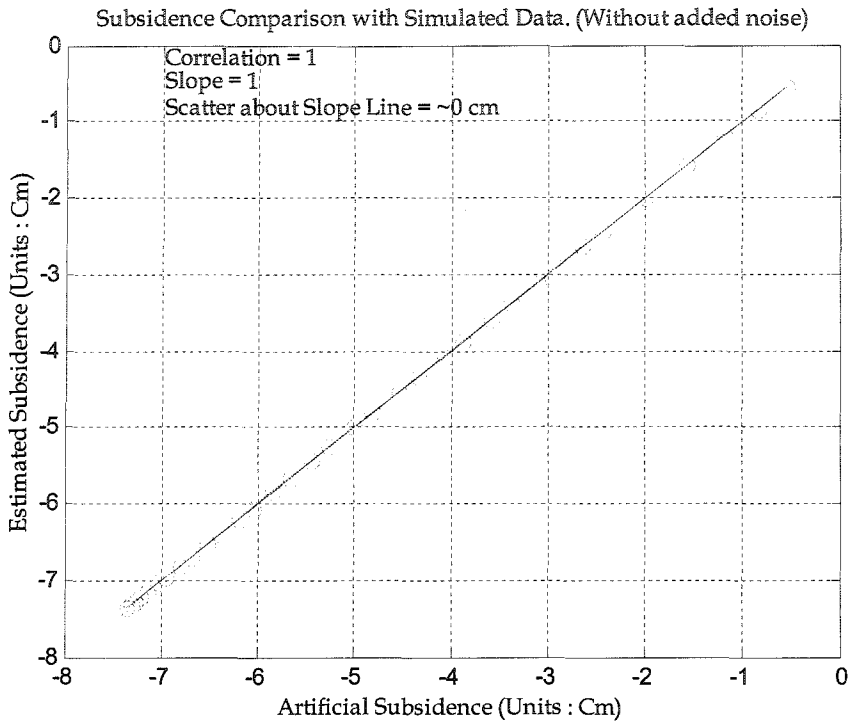

Figure 4-25: Comparison of Subsidence sampled horizontally

Note that East-West and Subsidence movement correlate favorably, however, the North-South movement estimate is highly scattered, but very regular and grossly overestimated. This problem is closely investigated in Section 4.3.3, and a possible solution is illustrated. For now, the reasons for these problems are intimated below:

1. InSAR based on polar-orbiting satellite sensor is relatively insensitive to ground movement in the North-South direction due to its imaging geometry. Since the contribution of the SRC measurement to the North-

South direction is low, the potential for the least squares estimate to be non-convergent to the actual solution is high. As noted, the convergence issues with least squares solutions on the problem at hand are dealt with in Section 4.3.3.

2. Synthetic ground movement data for each directions (East-West, subsidence and North-South) was first generated as discussed earlier. These data sets were then combined to obtain the SRC-D (SRC descending pass) using equation 3-16 and SRC-A (SRC ascending pass) using equation 3-17. The least squares estimation technique as discussed and defined by equation 3-19 was then used on the simulated SRC-D and SRC-A to estimate individual movement directions. The estimated movement from the results obtained from equation 3-19 was then compared with the initial synthetic dataset for movement in each direction. The least squares estimation technique works well for the East-West and subsidence estimates, provided the homogenous ground movement assumption holds true for a bounded region of n points as illustrated by Figure 3-10. In this case, the assumption was that the solution of the over-determined system is the result of all measured components (x, y and z) being homogeneous over a given grid of n points. Otherwise, the solution of the predicted components may exhibit large errors if it is discontinuous or substantially non-homogeneous over that grid. Figure 4-26 illustrates

that, for the case of the horizontal line through the center of the maximum subsidence, the North-South component changes direction from positive to negative, while the East-West and Subsidence components do not. As a result, the assumption of non-homogeneous movement is least applicable to the North-South movement as this would manifest in the SRC. Under this situation, the estimated North-South movement might not only have large errors but might also not correlate well. Both of these problems occur in this case as illustrated previously in Figure 4-24.

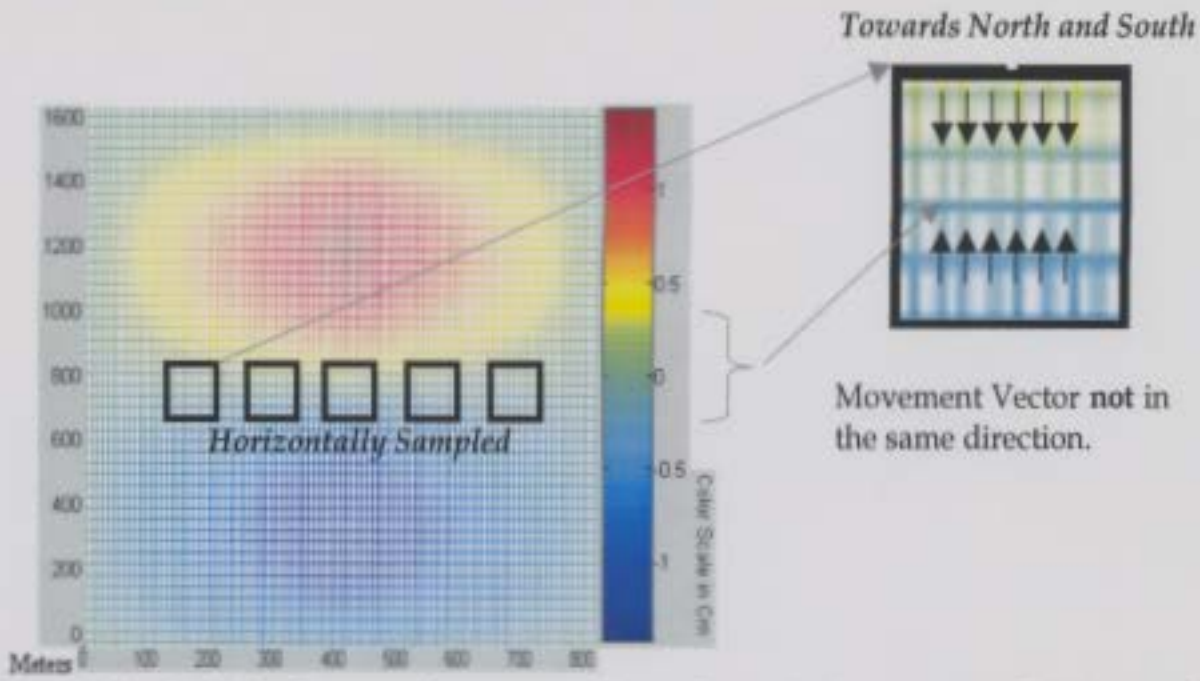

Figure 4-26: North-South ground movement shows discontinuity over a small region on the ground when sampled horizontally

Consider the second case where points are sampled along the vertical axis that is running from North to South. Figure 4-27 illustrates the position of these simulated monuments.

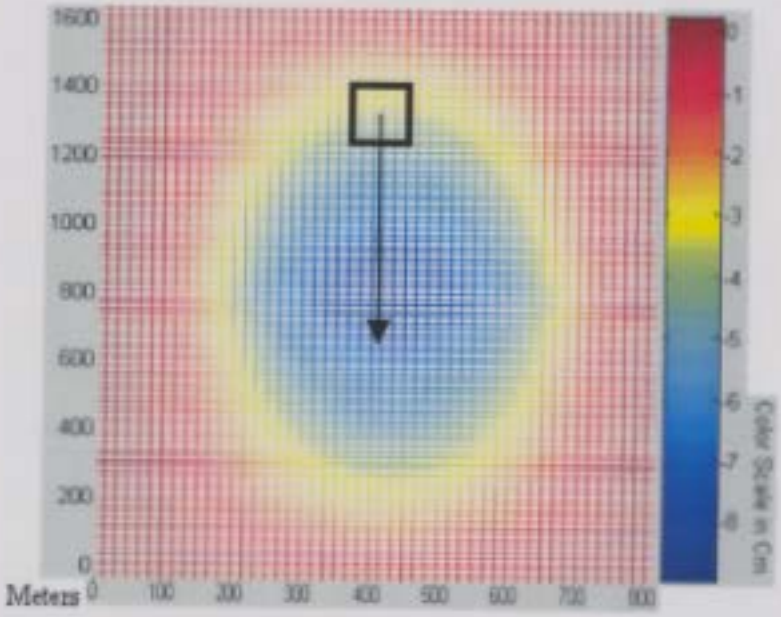

Figure 4-27: Monuments sampled vertically as shown by the arrow

The plots shown in Figure 4-28, 4-29 and 4-30 are the solution of the least squares estimates compared with synthetic data sampled along the vertical line.

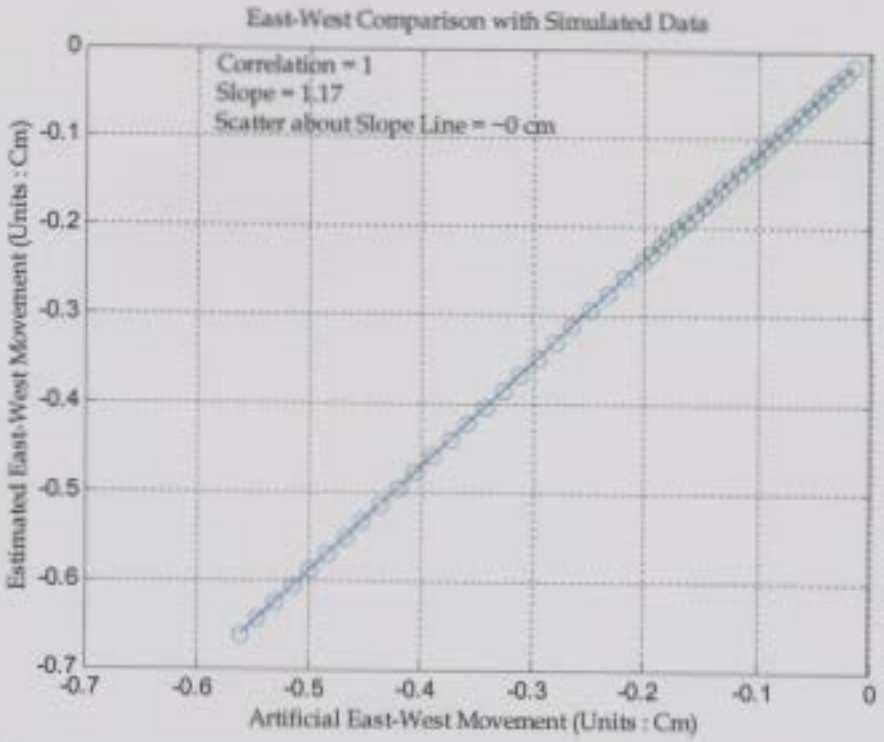

Figure 4-28: Comparison of East-West movement sampled vertically

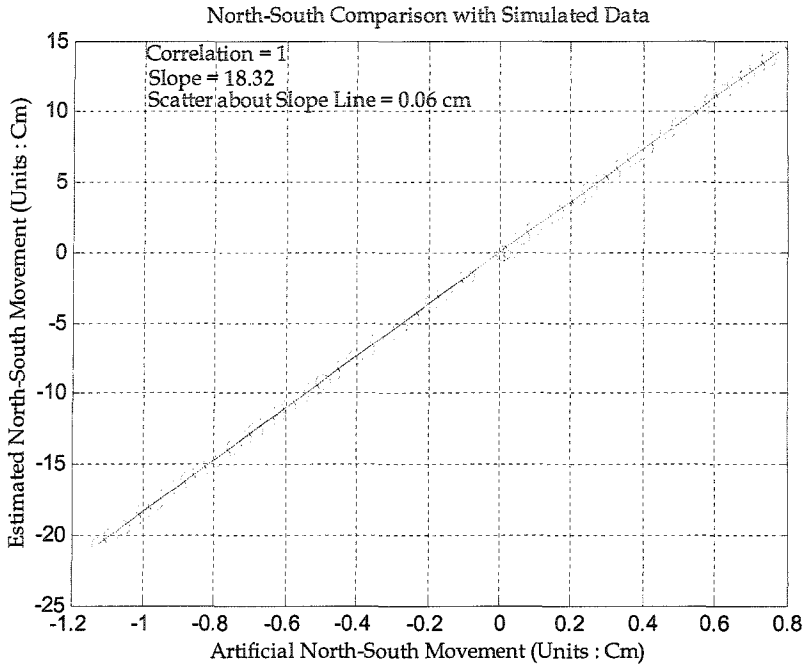

Figure 4-29: Comparison of North-South movement sampled vertically

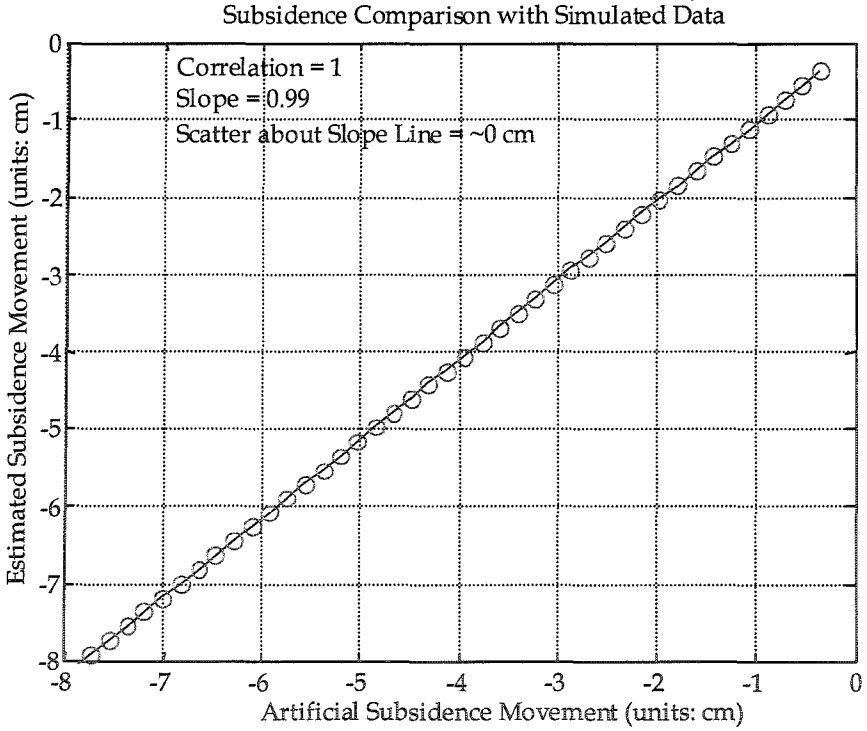

Figure 4-30: Comparison of subsidence movement sampled vertically

Note that in the second case, a tight linear trend observed in the estimated North-South movement. This may be explained by observing that the North-South movement along the line does not change direction (Figure 4-31) over the least squares estimation region, as it did for the first case along the horizontal line. However, the North-South movement is still grossly overestimated indicating that the least squares solution has not converged to the correct solution. It is speculated that this is due to the fact that SRC measurements do not contribute significantly to the North-South component. Therefore, the least squares solution is not convergent for this direction.

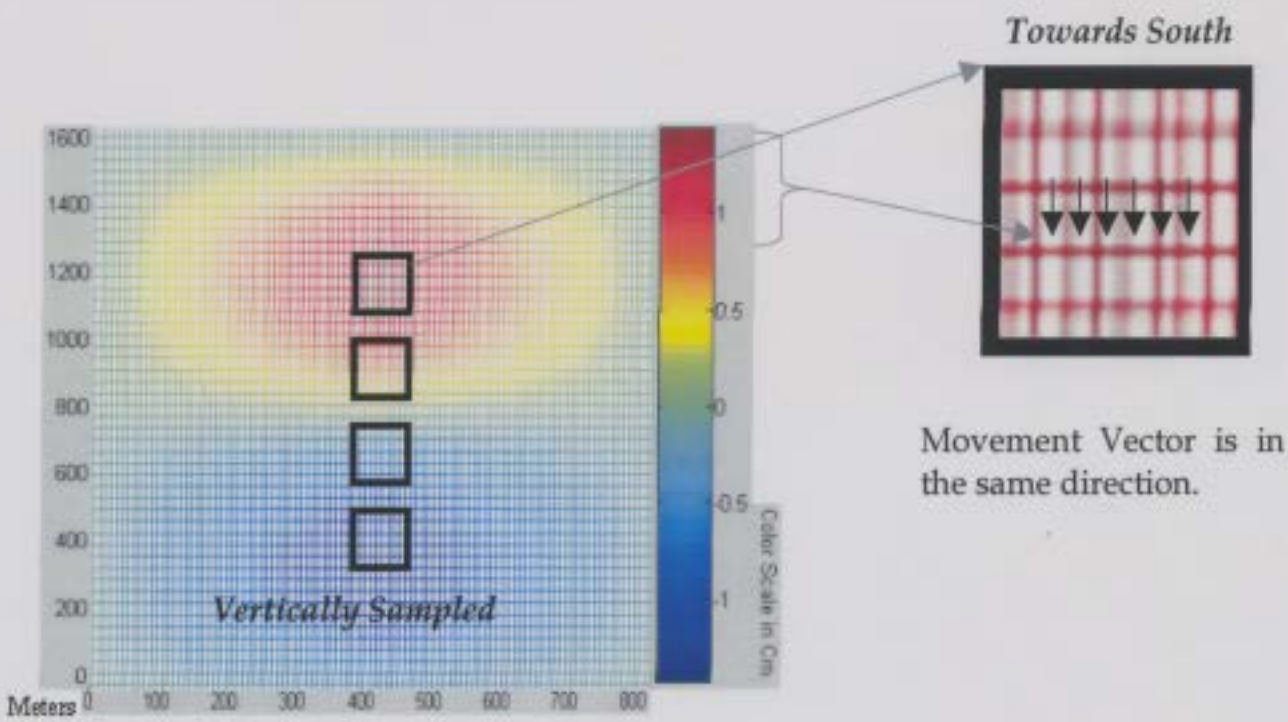

Figure 4-31: North-South ground movement shows homogeneity over a small region on the ground when sampled vertically

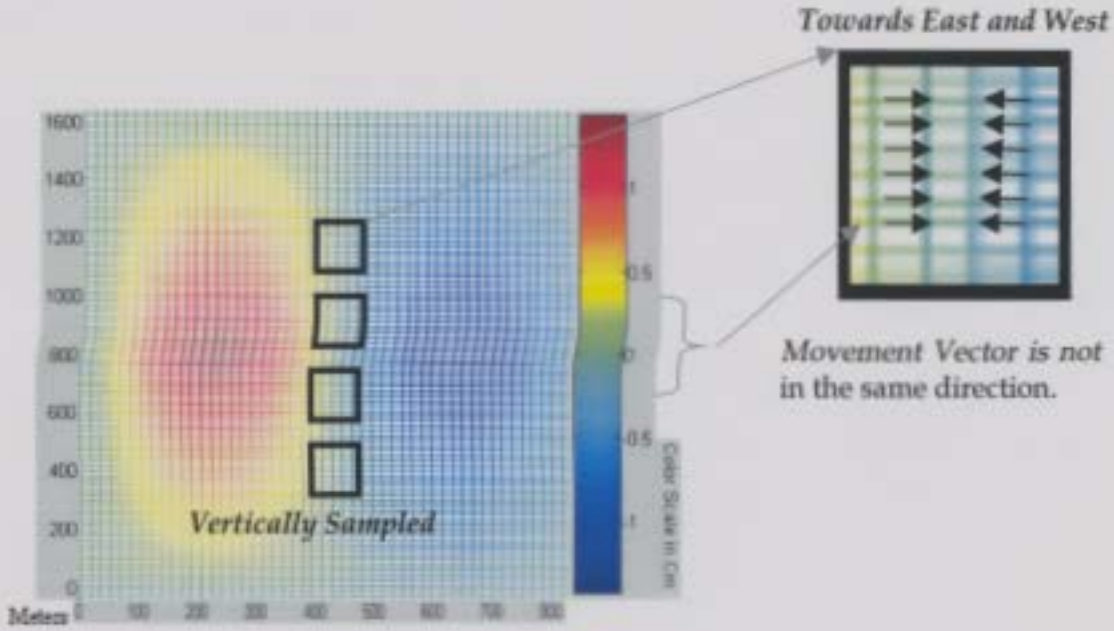

Figure 4-32: East-West ground movement shows discontinuity over a small region on the ground when sampled vertically

It can be observed that the slope of the estimated East-West movement in Figure 4-28 had degraded in comparison with Figure 4-23 without the loss of correlation. This degradation is likely due to the fact that the East-West components will change direction over the small image region used for the least squares estimation. However, loss in correlation is not observed in the East-West movement because of the large contribution of the SRC component to the East-West direction.

The conclusion from the above analysis suggests that the estimated North-South ground movement will be grossly overestimated irrespective of being in regions of large (with no expected direction changes) or small (with expected direction changes) North-South movement. This is due to the fact that the

North-South component does not substantially contribute to the InSAR SRC. Note, however, that there is no bias in regions of homogeneous ground movement for zero North-South movement. Nevertheless, strong correlation can be expected in regions undergoing uniform North-South movement that is either moving northwards or moving southwards as a least squares solution. Regions undergoing movement in both directions as shown in Figure 4-26 suggest that the estimated solution would be decorrelated.

To get an overall idea of the expected errors associated with ground movement measurements using least squares techniques, the third case is now considered with a uniform sampling of the entire image grid. To be consistent with a uniform survey, monument positions were sampled all over the image as shown in Figure 4-33.

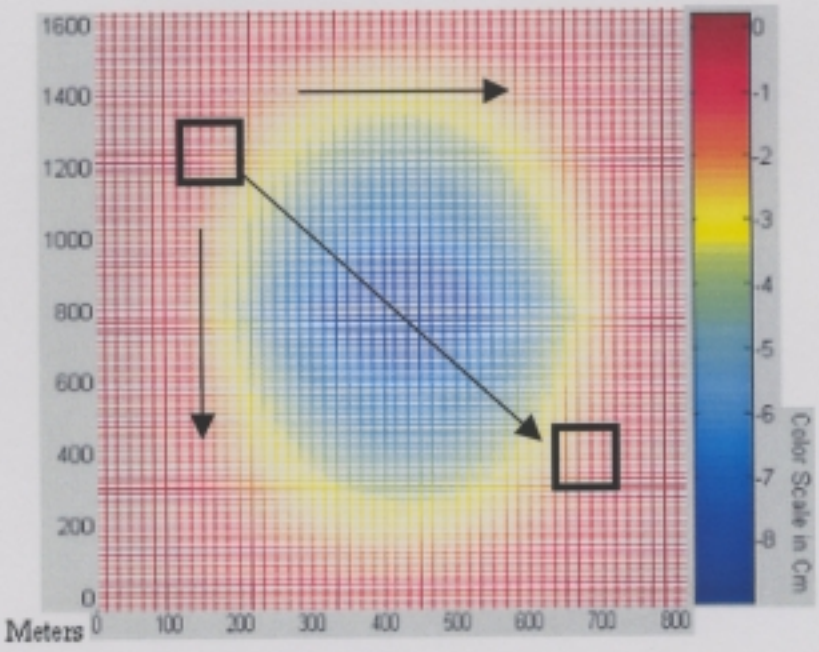

Figure 4-33: Monuments sampled along the image grid

Figures 4-34, 4-35 and 4-36 illustrate the comparison between estimated ground movement and artificially generated ground movement vectors for this case. The results appear similar to those previously exhibited by the horizontally sampled line, whereby good results appear in subsidence and East-West. High scatter and overestimation is exhibited by the North-South component estimate. It is therefore speculated that the major reason for non-convergence to an optimal solution is due to the low contribution of the North-South component to the SRC.

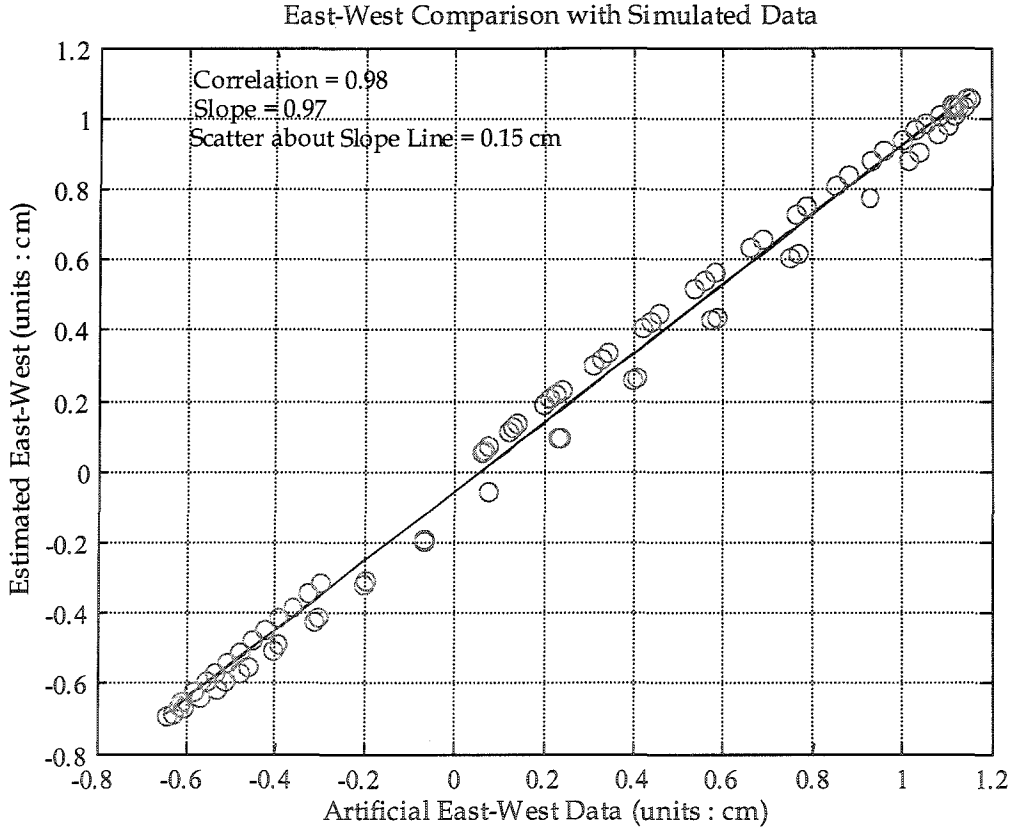

Figure 4-34: Comparison of East-West movement sampled over the entire image

The points were sampled over the entire image region, extreme Eastward movement and extreme Westward movements are observed in Figure 4-34.

Similarly, extreme Northward movement and extreme Southward movement are observed in Figure 4-35.

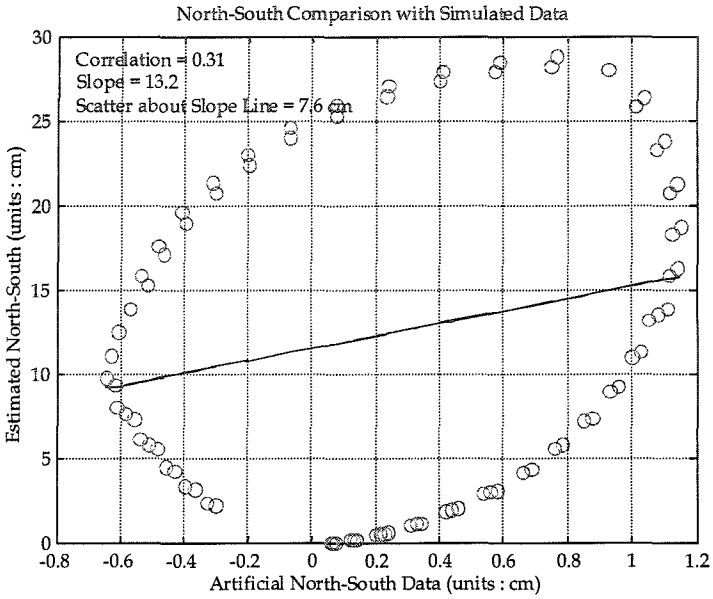

Figure 4-35: Comparison of North-South movement sampled over the entire image

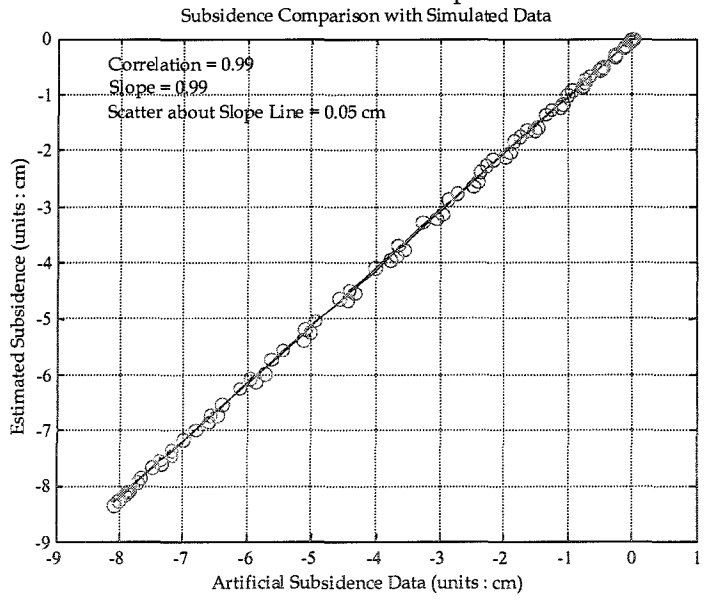

Figure 4-36: Comparison of subsidence movement sampled over the entire image

Accuracies of DInSAR in measuring ground movement are often limited by atmospheric artifacts and phase noises due to spatial decorrelation, and the

accepted measurement errors are ± 5 mm in the SRC measurements. To account for this in the simulated data, Gaussian noise can be introduced to the synthetically generated Slant Range Change data to get a sense of the additional measurement scatter associated with practical ground movement measurements. Figure 4-37 illustrates SRC-A generated as discussed above after adding Gaussian noise with a variance of (5 mm) ^{2}.

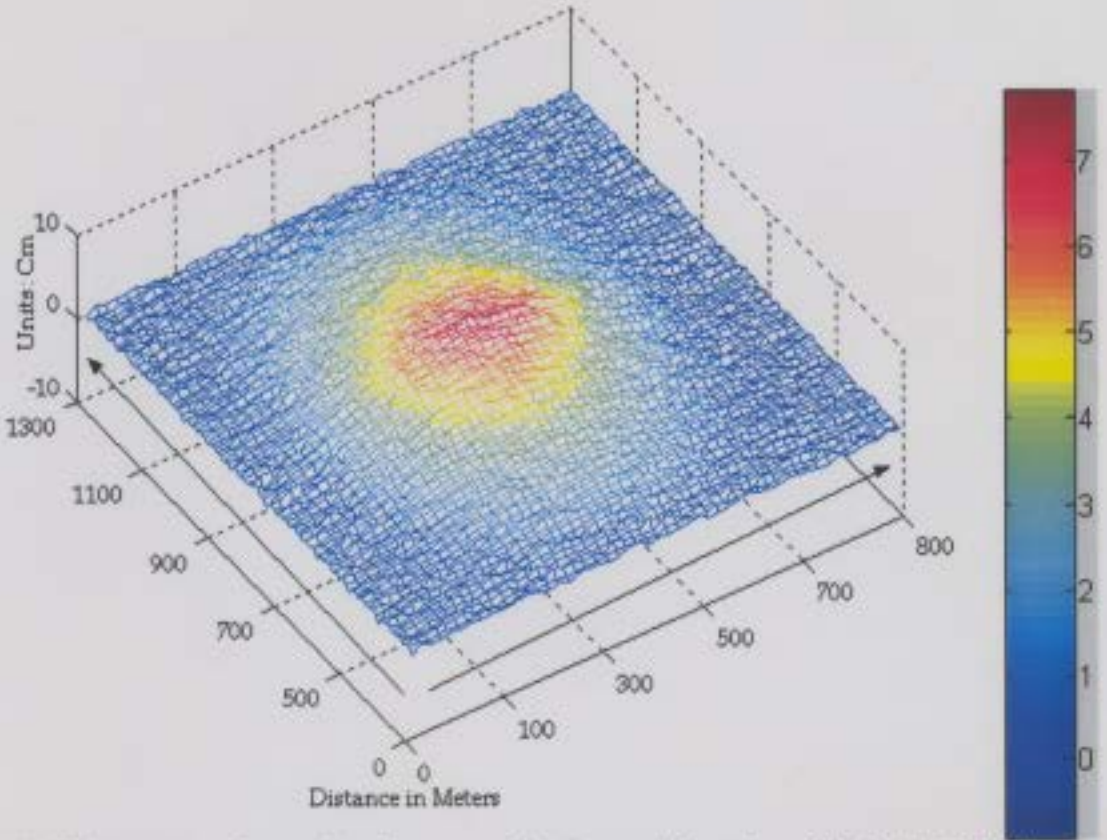

Figure 4-37: Slant range change data for ascending pass with noise added. (Artificially created from individual East-West, North-South and Subsidence data. SRC shown as positive here.)

Figures 4-38, 4-39 and 4-40 show the comparison of ground movement derived by the least squares estimation model with that derived from the SRC. In this case, the monument sampling is a uniform grid (both vertical and horizontal)

about the SRC data. The effect of noise on the solution of individual movement components is shown in the plots below as additional scatter about the trend line. As with the previous data set, the plots illustrate that the least squares model provide fairly accurate estimate of subsidence and East-West movement. The North-South movement is overestimated and does not correlate very well for reasons explained earlier.

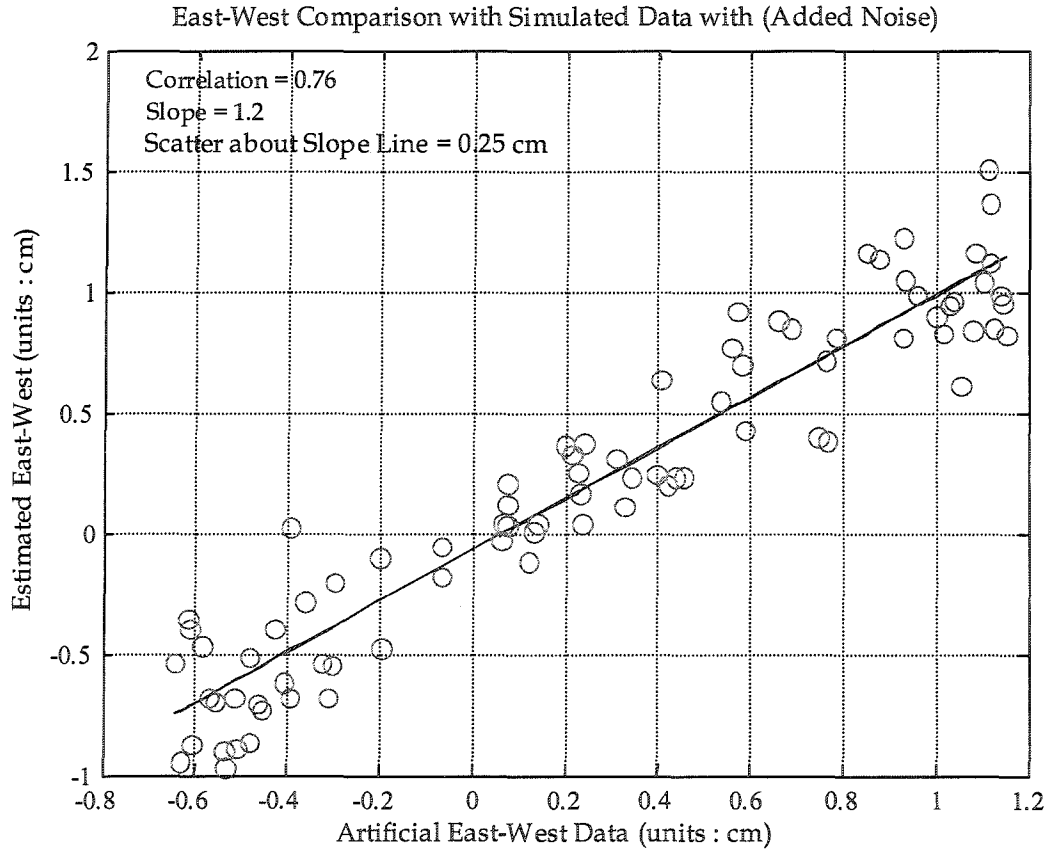

Figure 4-38: Comparison of East-West [with noise]

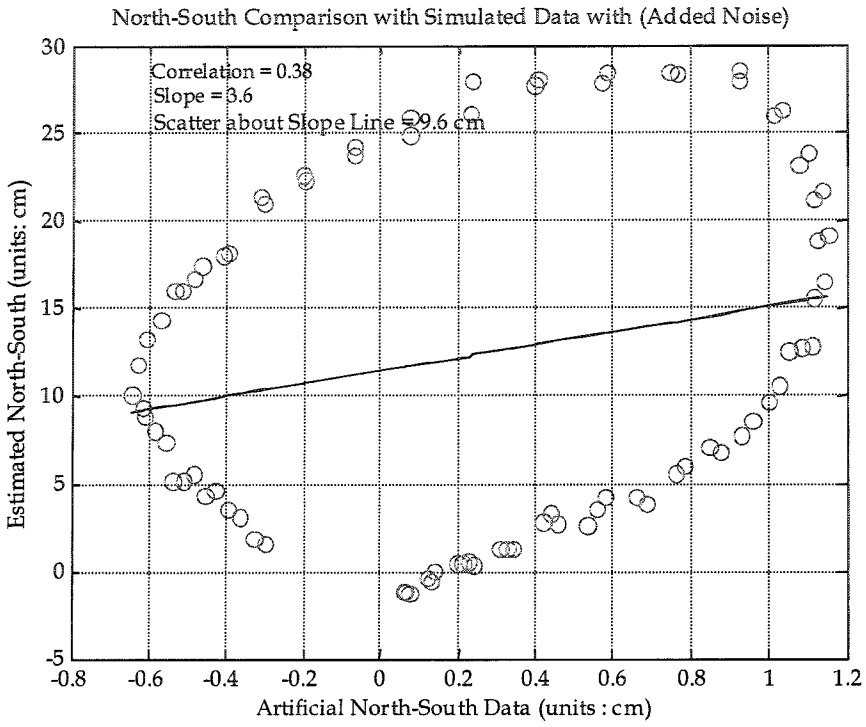

Figure 4-39: Comparison of North-South [with noise]

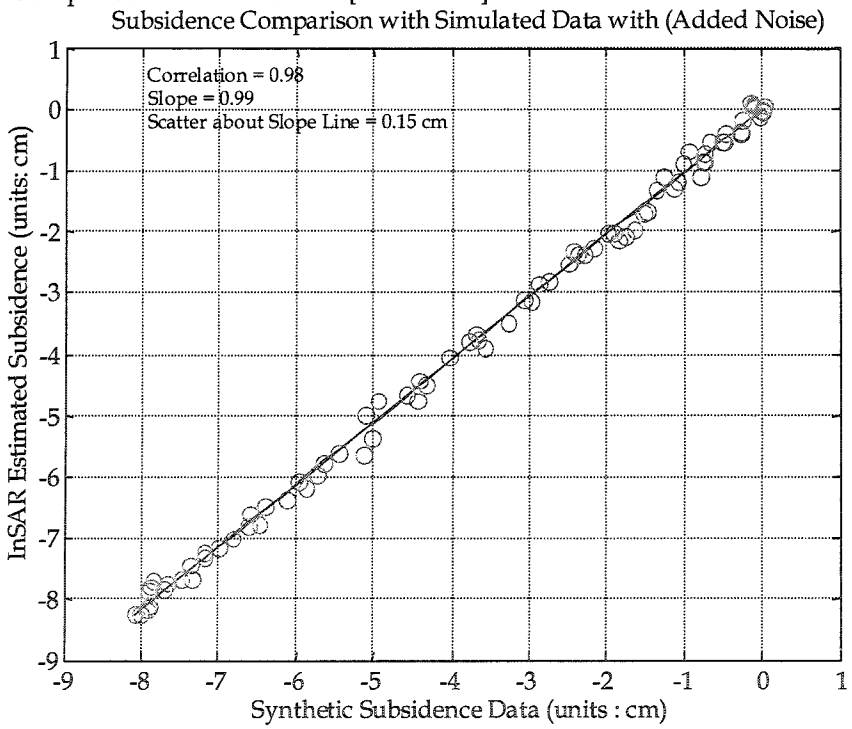

Figure 4-40: Comparison of Subsidence [with noise]

4.3.3 Simulation of Movement Components Derived from Modified Least Squares Technique

The key component for estimating North-South ground movement presented earlier relies on Least Squares Solution (LSS). Recall that this method relies on the translation of an underdetermined system to an over determined one based on variation of satellite incidence angle over a homogeneous ground movement region. Results presented in the previous section shows that the method requires modification to address the gross over estimation of the North-South movement and the observed scatter, as shown in Figure 4-39.

Consider a solution of the linear system in the least squared sense as defined in equation (3-19) as MX = b. Solving an over determined system MX = b in the least-squared sense means minimizing the square sum of the error vector defined as $\mathbf{e}^T\mathbf{e}$, where **e** = MX-b and the superscript T indicates transpose. The LSS solution then becomes $X = (M^TM)^{-1}M^Tb$ [43] provided the inverse exists. In this case X is the column vector of size 3 × 1 and M is of size 2n × 3, where *n* is the number of grid spaces considered for estimation of 3-D ground movement.

Let the estimated component obtained from the LSS be denoted as $\hat{X}$. Then for all X, $\|M\hat{X} - b\| \leq \|MX - b\|$ should hold if LSS truly reduces the error **e**. However, the LSS technique fails when columns of M are linearly dependent [44, 45]. In this case the existence of a single minimizing solution $X = \hat{X}$ is in

question [44]. This implies that if the columns of the matrix M in the least squares problem manifest linear dependency, then there is no unique solution. In this case it is still possible to construct a solution provided the (M^TM) matrix is invertible but it is likely to be inaccurate. The problem becomes dominated by the dependent columns, and becomes very ill conditioned [43].

A closer investigation on the transformation matrix M for the simulated data reveals linearly dependent columns of M, which indicates that estimation of non-measured component of the movement may be very inaccurate. The satellite SAR geometry is natively more sensitive to East-West and subsidence directions than North-South direction. This implies that the solution of the estimated North-South component might be inaccurate. The previous results indicate that this inaccuracy is manifested in the poor estimation of the North-South component. Given this, the obvious question is whether it is possible to improve the estimated North-South movement with the aid of a modified LSS. Various other forms of LSS techniques are proposed in the literature to address the problem with linear dependency including [46]. Constrained LSS is the most desirable one in this case because it provides a control over the estimates. Observing the previously simulated results indicates the expected error in the North-South direction. This knowledge can be imposed on the matrix M to obtain a constrained LSS solution. The expected errors in measuring North-South movement that is due to the relative insensitivity of InSAR along North-South

direction can be used to create a constrained matrix W with the same number of rows and columns as that of M. Figures 4-38, 4-39 and 4-40 suggest that for every unit of subsidence movement the North-South movement is over estimated by ~400%. Under the assumption of bowl shaped homogeneous ground movement presented earlier, it was observed that the magnitude of lateral ground movement is limited to 1.5cm. Thus 400% of 1.5 cm corresponds to 6cm, which can be used as a constrained coefficient in the matrix W. The matrix W then becomes:

$$W = \begin{bmatrix} a_i & b_i & c_i \\ a_i & b_i & c_i \end{bmatrix}, \tag{4-4}$$

where i = 1 to number of rows,

$a_i = c_i = 1$ and

$b_i = 6$.

The coefficients a_i and c_i are that of East-West movement and subsidence respectively, and can be set to unity since these components are the measured components and manifests no errors in the estimations. The coefficients b_i are that of North-South movement estimates and can be weighted to 6. This could balance the estimated ground movement solution by fixing the relative error that was observed in the plots before.

The new system then becomes

$$W M X = b. \tag{4-5}$$

The new system is identical in form with the old one, but the LSS of the new system becomes

$$X = ((WM)^T WM)^{-1} (WM)^T b, \tag{4-6}$$

which should not adversely affect the East-West and subsidence estimates while improving the North-South estimation. The state of singularity for equation (4-6) is controlled by the coefficients a_i, b_i and c_i. The coefficients for the weighting matrix W were chosen to fix the relative errors observed in the previous plots. The choice of coefficients would enable a non-singular system of equation by which ground movement parameters can be estimated. Figure 4-41 illustrates the North-South estimation with the aid of constrained LSS. It can be observed that the gross over-estimation in Figure 3-39 was minimized considerably.

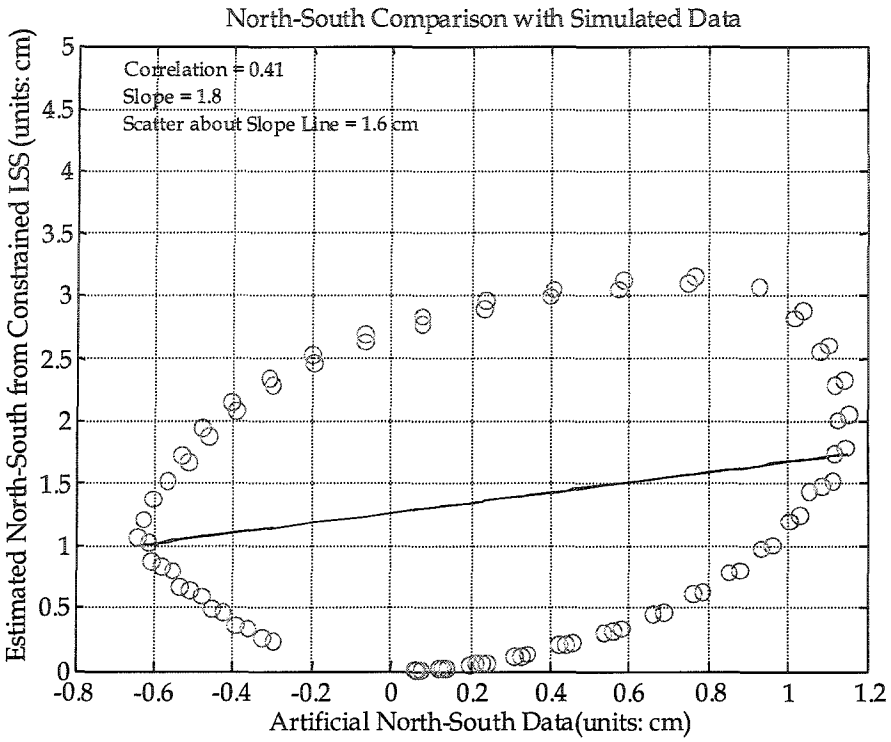

Figure 4-41: Comparison of Subsidence as a solution of constrained LSS with simulated data

The solution of equation (4-6) can be further constrained by taking the gradient of the SRC over a neighborhood of pixels, where ground movement is to be estimated. The gradient vector magnitude of the SRC over a small grid will be proportional with respect to the amount of lateral ground movement of that region as explained in Section 4.2. This assumption is on the basis of uniform subsidence, whereby the region is sinking with uniform lateral movement from both directions (East-West and North-South) resulting in a bowl-like shape as illustrated in Figure 3-1. Figure B-4 in appendix B shows the true shape of the subsiding area and is indeed like a bowl. Thus, more lateral movement is likely to occur when the rate of change of the SRC with respect to distance is observed

in a particular region. With this assumption, the solution obtained from equation (4-6) for North-South movement can be adjusted (weighted) using the gradient of the SRC vector of that region. Ground monument positions were sampled uniformly over the entire image as was done previously. Figure 4-43 illustrates the success of this improved estimation technique, where the estimated North-South ground movement compared with synthetic data reduces the scatter to 0.47 cm.

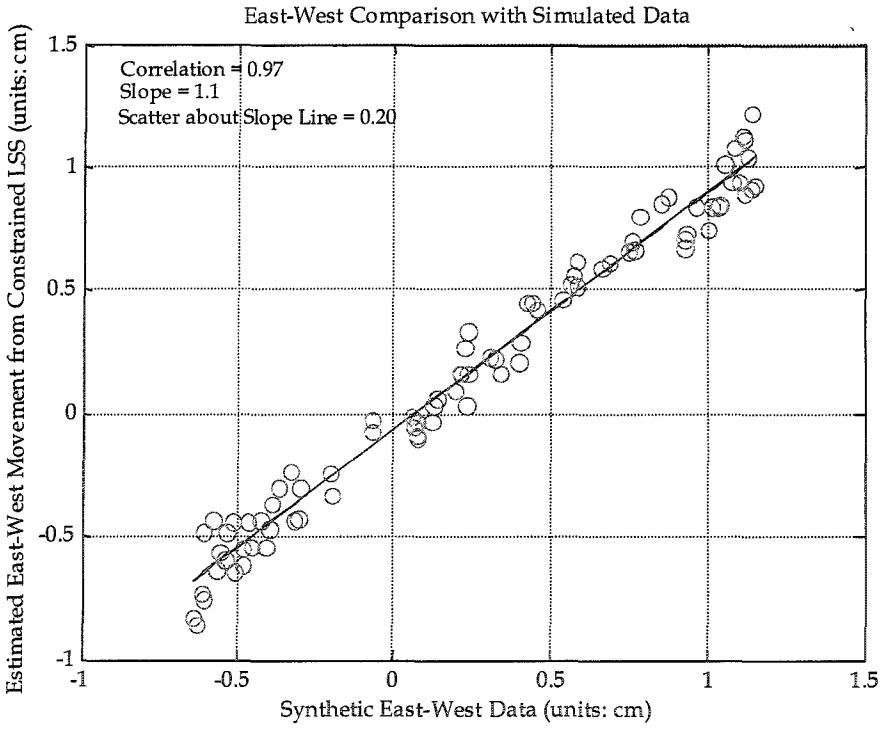

Figure 4-42: Comparison of East-West ground movement from constrained LSS solution

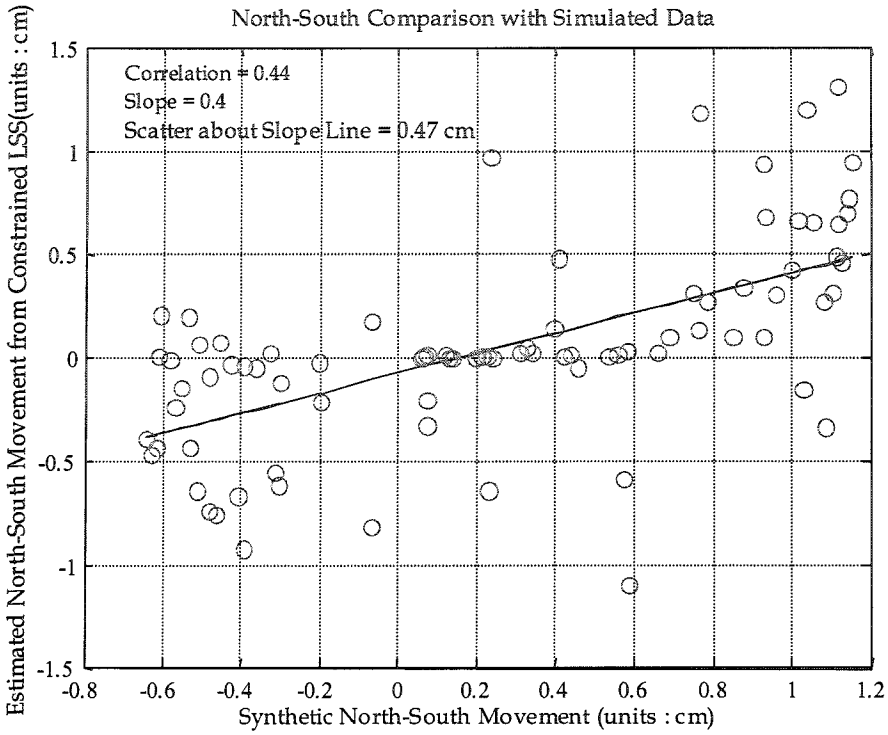

Figure 4-43: Comparison of North-South ground movement from constrained LSS solution

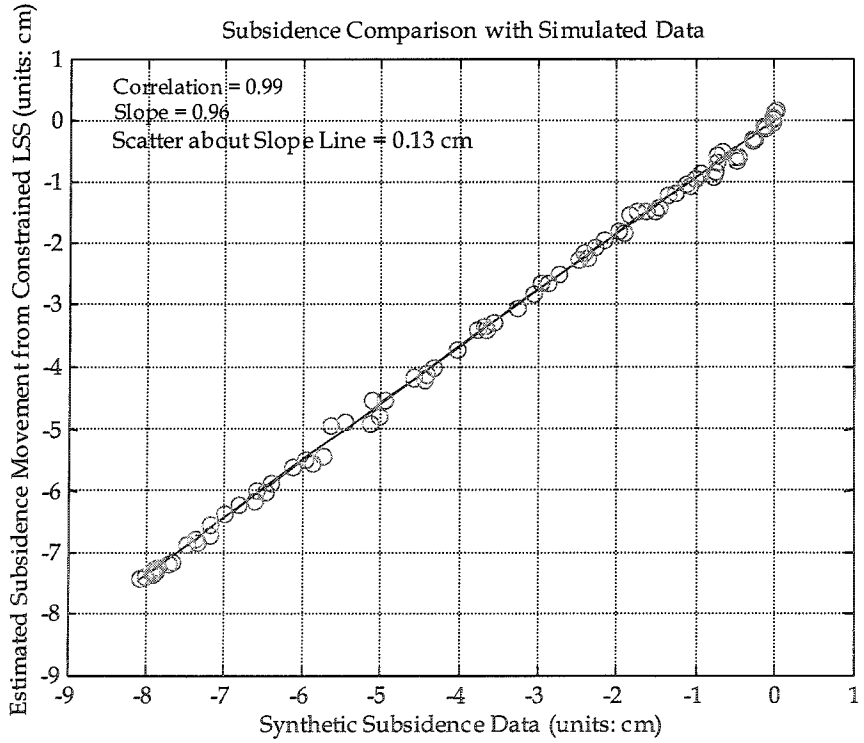

Figure 4-44: Comparison of North-South ground movement from constrained LSS solution

Note that the new technique estimates the North-South movement more accurately by minimizing the scatter about the slope line in Figure 4-39 from 9.6 cm to 0.47 cm in Figure 4-43.

Although this section mentions various assumptions that have to be made to apply the constrained LSS technique, it is important to realize that these assumptions can be generally identified by observing the DInSAR derived slant range measurements. Therefore, the application of this technique only requires information obtained by remote sensing and need not rely on any in-situ or other non-remote sensing sources of a priori information.

4.4 Validation of 3-D Ground Movement Measurements

The final step in the validation is to test the 3D movement estimation technique that employs the least squares model as presented in Section 3.3. The same interferograms and monument data were employed for this validation as presented in the section 4.2. As discussed previously, the least squares technique requires homogenous ground points of coherent movement. To determine the optimum size of the homogeneous patch of moving ground points, an optimization technique was used. Specifically, the least squares method was applied to a variable-sized window to extract lateral movement and subsidence; the subsidence component was then compared with the GPS data to determine the correlation. The window size n as introduced in Figure 3-10 was varied to

determine the best correlation as shown in Figure 4-45. The rationale behind using this method is that the subsidence should get progressively better as the lateral movement estimate improves; at some point the window size will become too large as the assumption of "coherently moving patch of ground" fails. A maximum distance of 10 pixels was limited to the range direction (row). Each pixel on the SAR image processed was of 8 m, which results to 80 m for 10 pixels. It was assumes that coherent ground movement on the range direction would be preserved under 80m. The number of pixels was incremented on the range direction to 10 and then perform the similar by incrementing one of the azimuth direction. This would collectively form the bounded region of coherent ground movement. A plot of this analysis is given in Figure 4-45. Careful observation of this plot shows that a suitable window would be 51 pixels (408m) in a rectangular configuration. Spatially this implies 5 rows of 10 pixels and 1 pixel on the 6^{th} row.

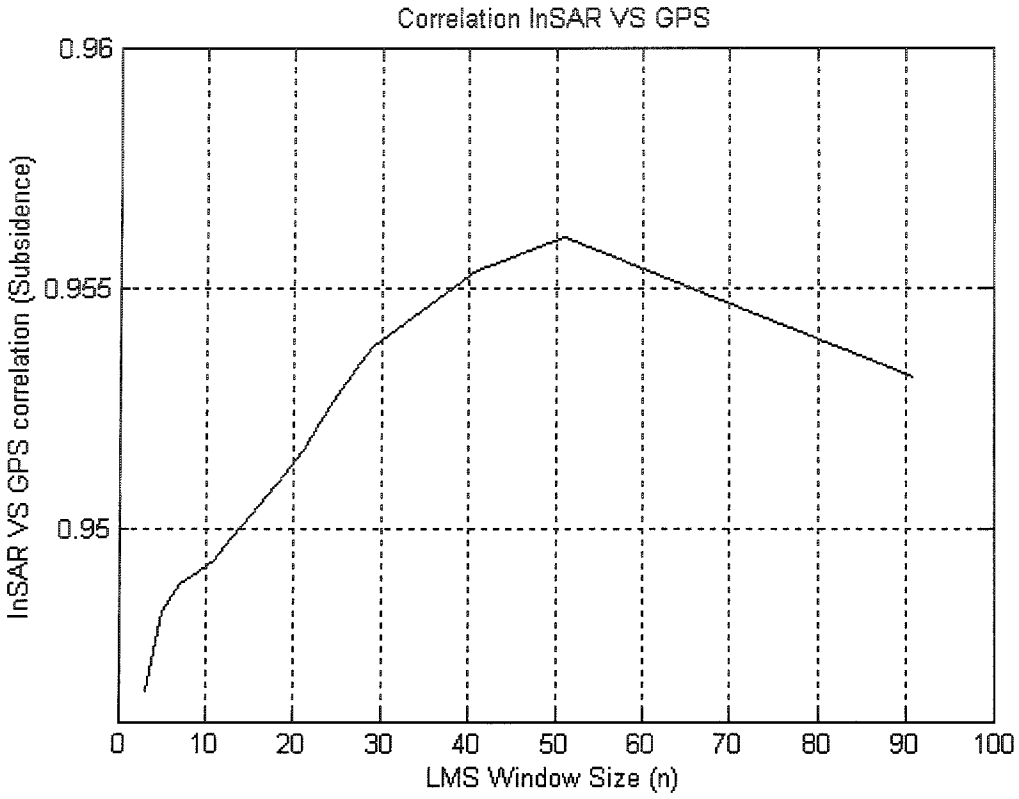

Figure 4-45: Correlation between DInSAR & GPS versus Least Mean Square (LMS) window size (n). The y-axis represents the correlation of InSAR estimated subsidence with respect to GPS measurements for all GPS monuments. The x-axis represents increase in the number of pixels for each InSAR versus GPS analysis.

Using this window size of 51 pixels, the simple least squares technique was applied to all sets of interferograms. These plots show an overall improvement in correlation of subsidence and East-West movement when compared with the previous results where it was assumed $\Delta y = 0$ (cf. Figures 4-13 and 4-14). Figures 4-46, 4-47 and 4-48 show subsidence, East-West and North-South movement obtained from the February - April 2001 pairs, compared with GPS measured movements all normalized to 24-day movement scale.

The subsidence and East-West movement shown in Figure 4-49 and 4-50 shows good correlation between the GPS measured movement and InSAR estimated ground movement. The north-south movement in Figure 4-51 shows poor correlation and is similar to the simulated results presented in Figure 4-39. The results are explained as follows:

1. The measurement error in the North-South direction is fairly significant compared to East-West or subsidence as explained in the previous section. With a 5 mm SRC error the expected scatter in East-West, subsidence and North-South are estimated to be 0.25 cm, 0.12 cm and 9.5 cm. The observed scatter about the slope line for the plots shown in Figure 4-49, 4-50 and 4-51 are within the expected limit as per the simulation results. Hence, the nature of the results is as expected from the simulation.

2. The measurement error of the GPS exacerbates the problem of decorrelated North-South movement and the additional scatter is observed about the plot's x-axis, which further degrades the results.

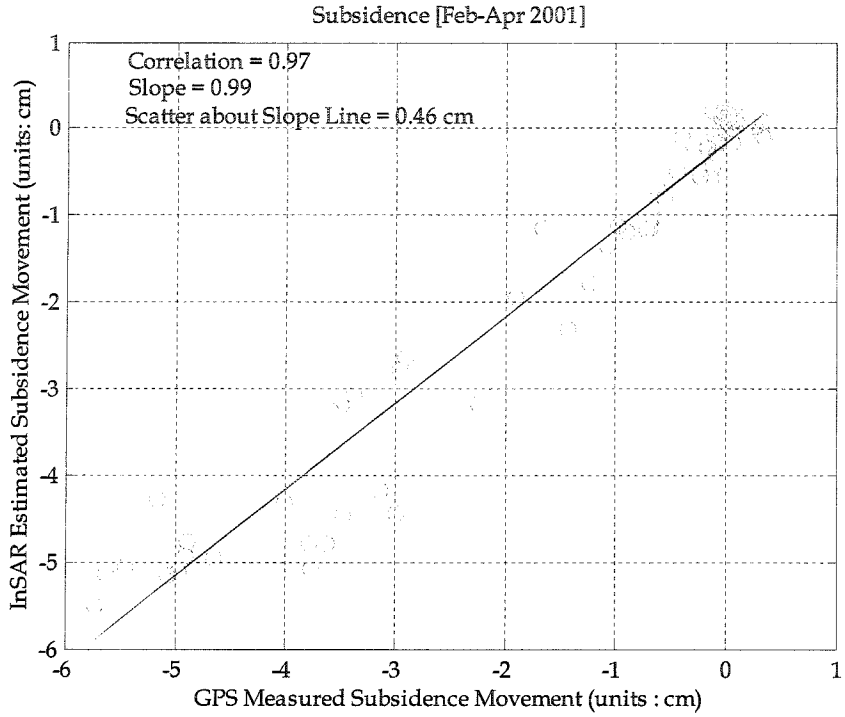

Figure 4-46: InSAR versus GPS Subsidence movement normalized to 24 days from February - April 2001

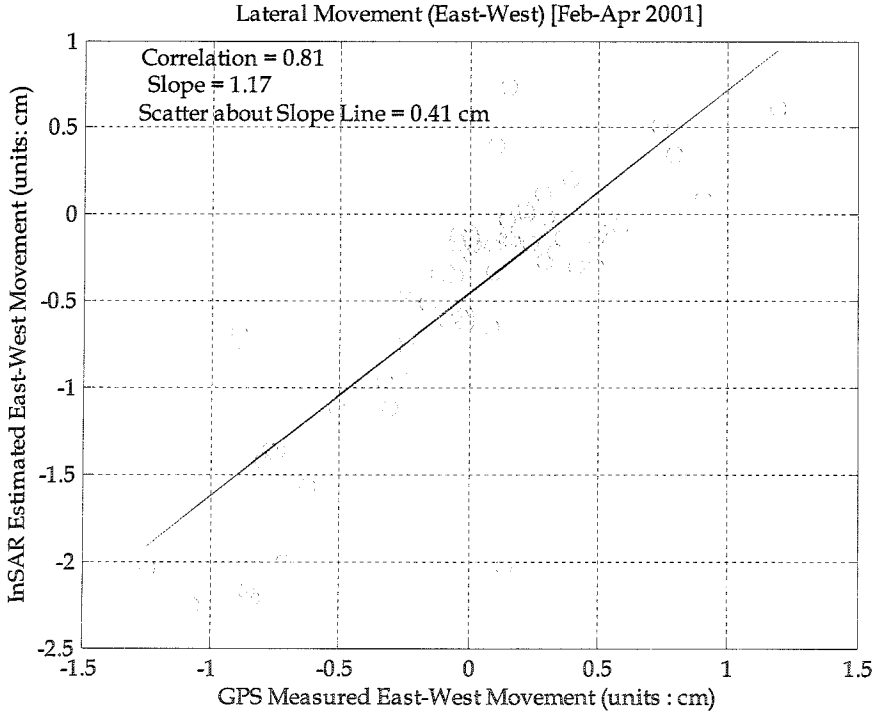

Figure 4-47: InSAR versus GPS East-West movement normalized to 24 days from February - April 2001

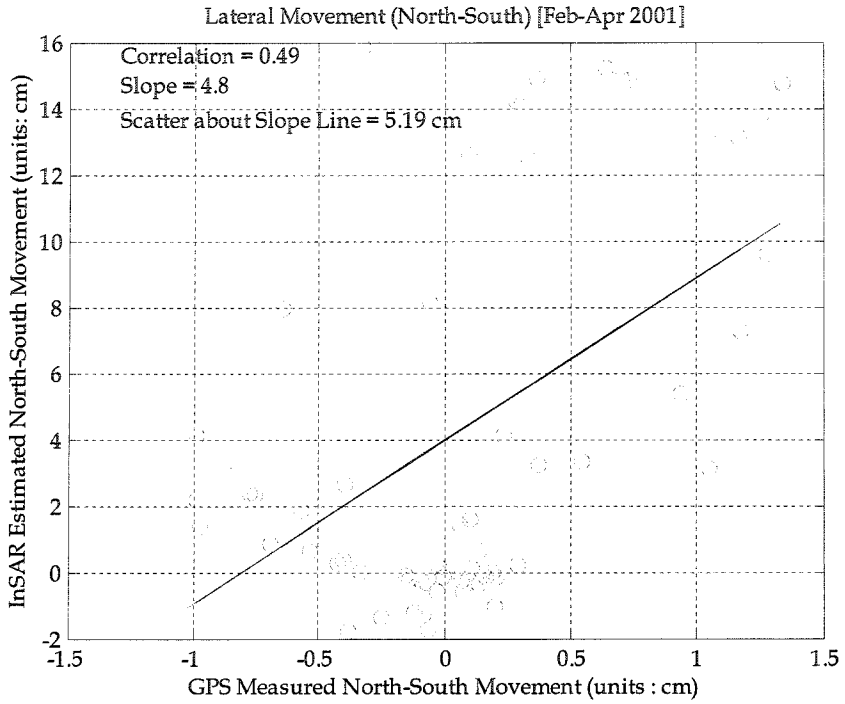

Figure 4-48: InSAR versus GPS North-South movement normalized to 24 days from February - April 2001

Figures 4-49, 4-50 and 4-51 show averaged movement from InSAR (February - September 2001) compared with GPS measured movement trends, both normalized to a 24-day movement scale. Appendix A contains the remaining plots for the entire interval. Carefully observing the two groups of plots (Figure 4-13 to 4-16) and (Figure 4-46 to 4-51) and Figures A-13 to A-21 in Appendix A, it can be seen that the correlation between InSAR measured movement and GPS measured movements have improved over single interferogram results by ~2% for subsidence and ~13% for East-West movement estimates, except for the North-South movement. A marked difference is seen in the East-West displacement when Figure 4-50 is compared with Figure 4-16. The correlation

improved from 0.74 to 0.87, slope improved from 0.8 to 0.81 and scatter about the slope line was minimized from 0.35 to 0.22. The relatively poor results with the North-South movement indicate that additional interferograms might be necessary for the averaging to reveal an improved correlation. More precise measurements of the monuments with a theodolite would also have helped demonstrate better correlation of the North-South movement. However, to truly demonstrate improved results an alternate LSS technique must be applied as was done previously for the simulated SRC data.

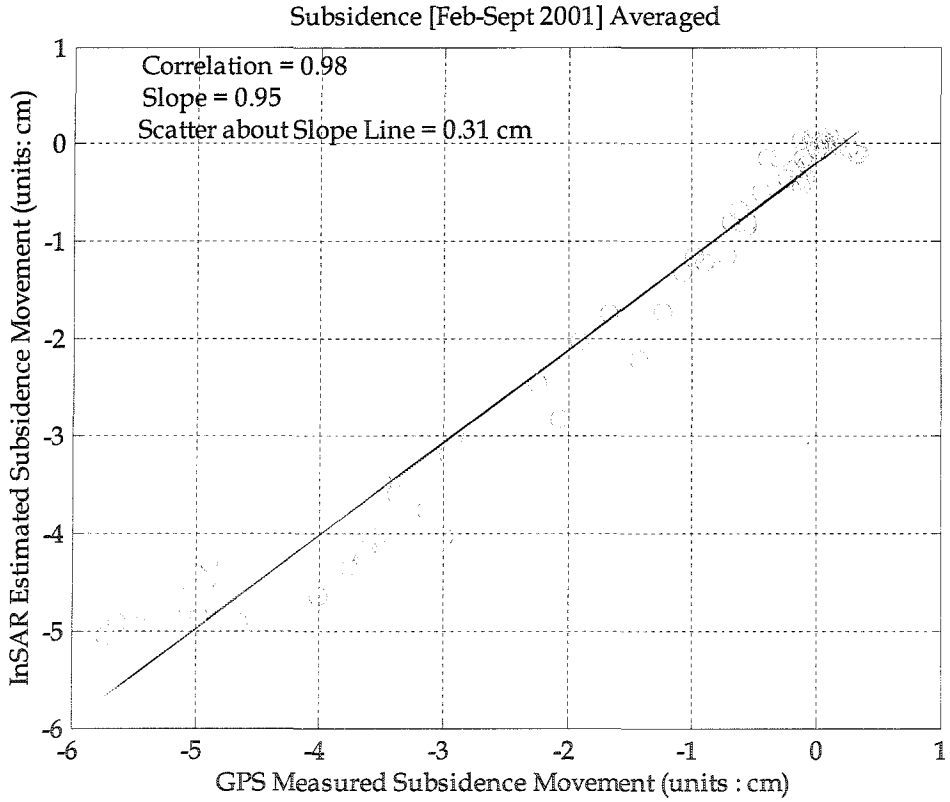

Figure 4-49: InSAR versus GPS Subsidence movement normalized to 24 days from February - September 2001

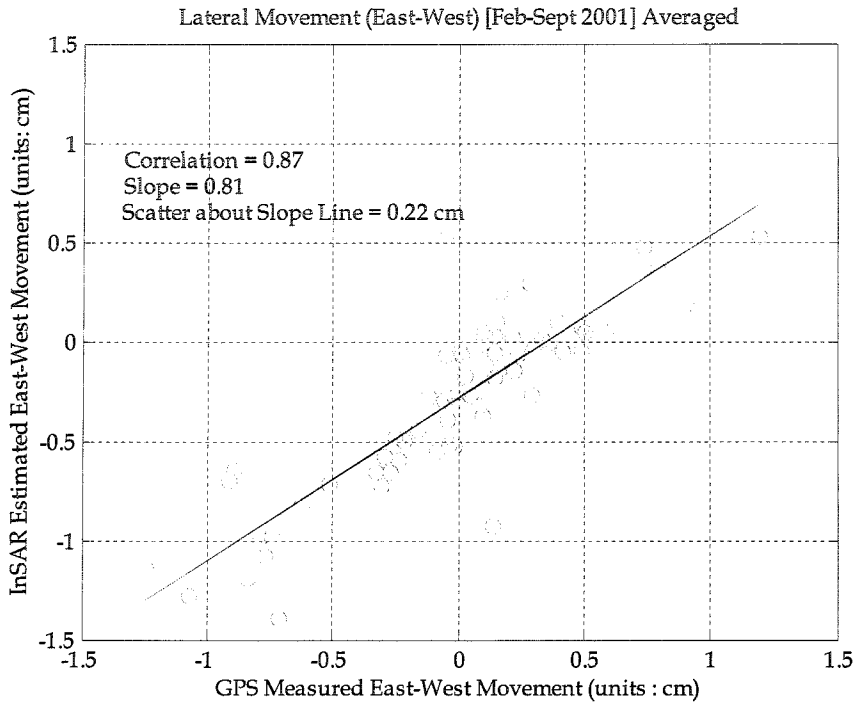

Figure 4-50: InSAR versus GPS East-West movement normalized to 24 days from February - September 2001

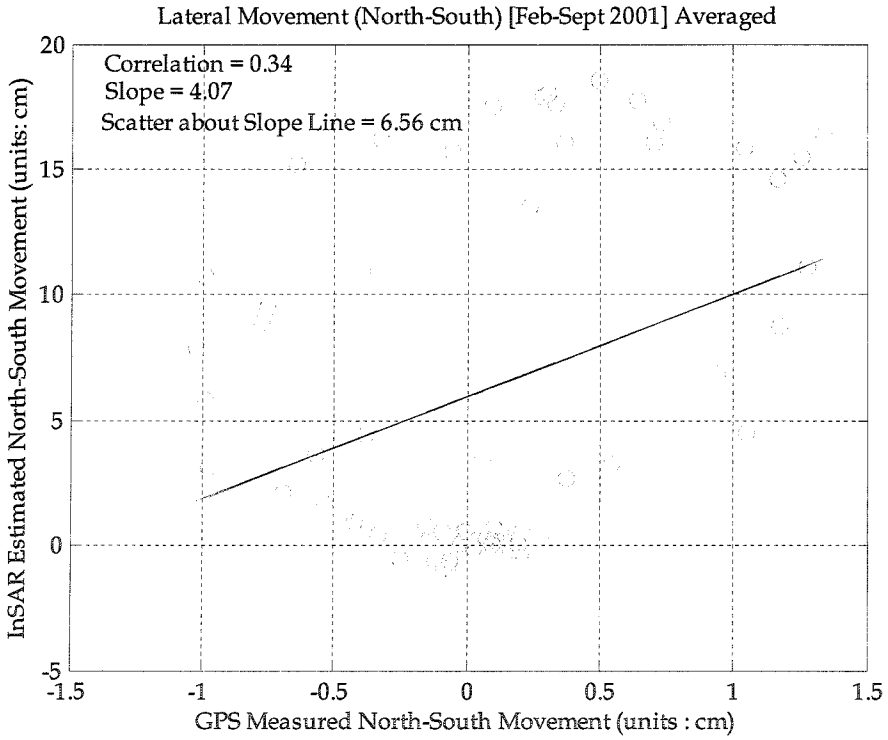

Figure 4-51: InSAR versus GPS North-South movement normalized to 24 days from February - September 2001

4.5 Validation of 3-D Ground Movement Measurements with Constrained Least Squares Solution

A constrained least squares solution as discussed in Section 4.3.3 showed considerable improvement in estimating North-South movement for the simulated results. The same technique can be applied to the obtained series of DInSAR data to validate 3-D ground movement. Figures 4-52, 4-53 and 4-54 show subsidence, East-West and North-South movement obtained from the February - April 2001 pairs compared with GPS measured movements all normalized to a 24-day movement scale.

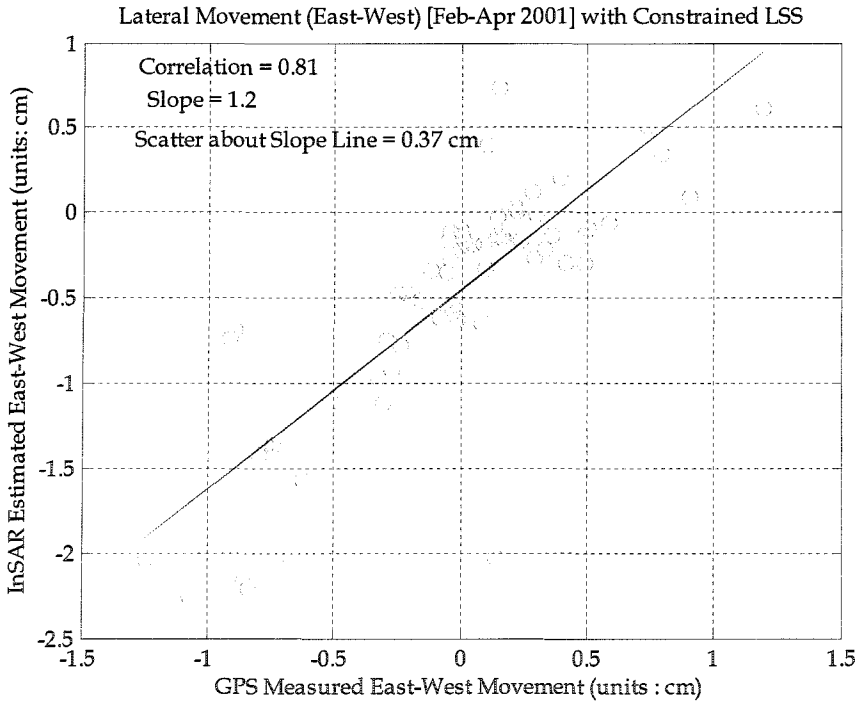

Figure 4-52: Comparison of East-West ground movement from constrained LSS solution

Figure 4-53: Comparison of North-South ground movement from constrained LSS solution

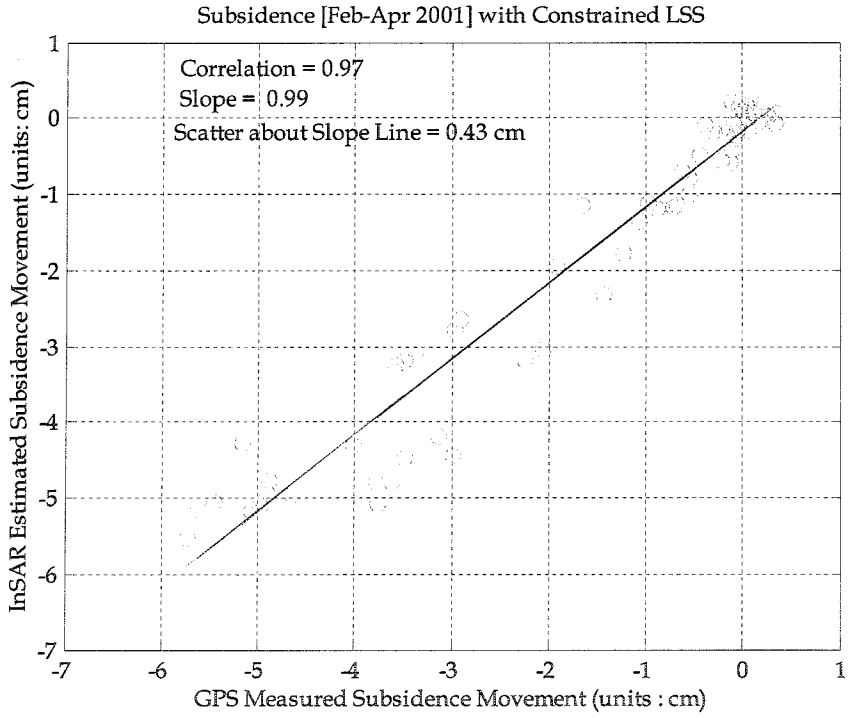

Figure 4-54: Comparison of subsidence ground movement from constrained LSS solution

Figures 4-55, 4-56 and 4-57 shows averaged movement from InSAR (February - September 2001) compared with GPS measured movement trends both normalized to 24-day movement scale. It is clearly observed from the series of Figures 4-52 to 4-57 and additional Figures in appendix A, Figures A-22 to A-30 that the constrained least squares solution has obtained better estimates for all three ground movement components, given that the space-borne SAR configuration is insensitive to North-South movement. The scatter about the slope line also falls well within the order of expected errors as suggested by the simulation results.

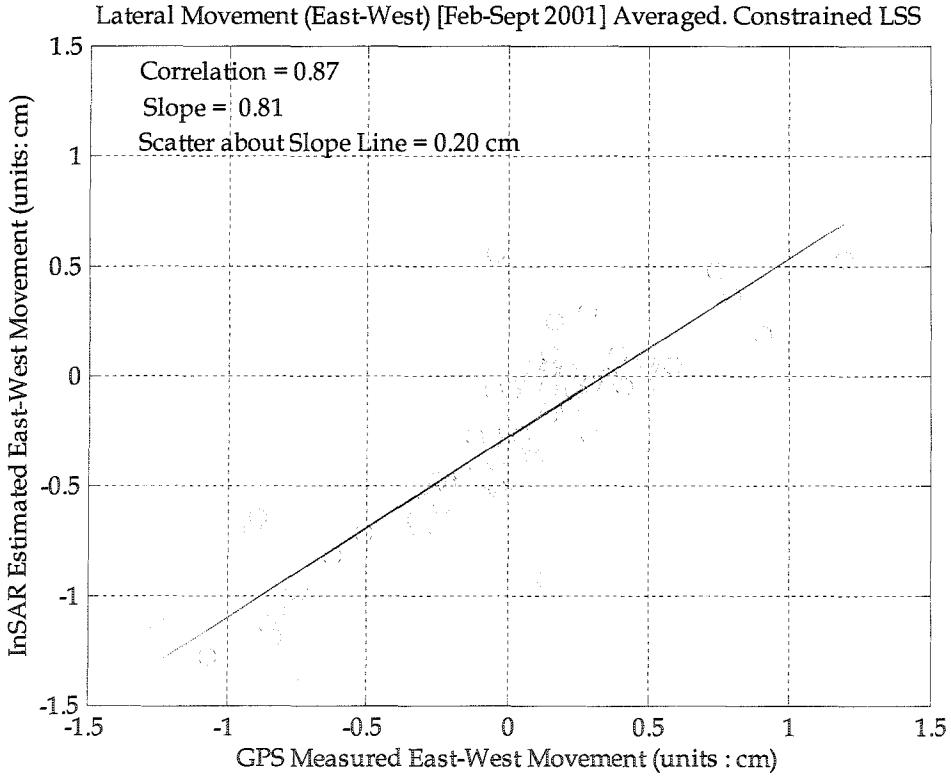

Figure 4-55: Comparison of averaged East-West ground movement from [Feb-Sept 2001] with constrained LSS solution.

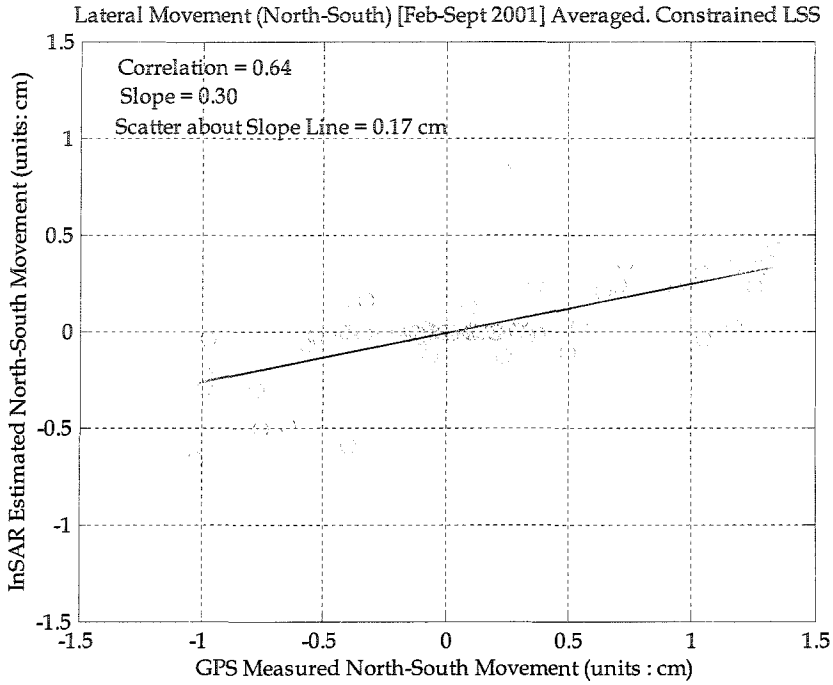

Figure 4-56: Comparison of averaged North-South ground movement from [Feb-Sept 2001] with constrained LSS solution.

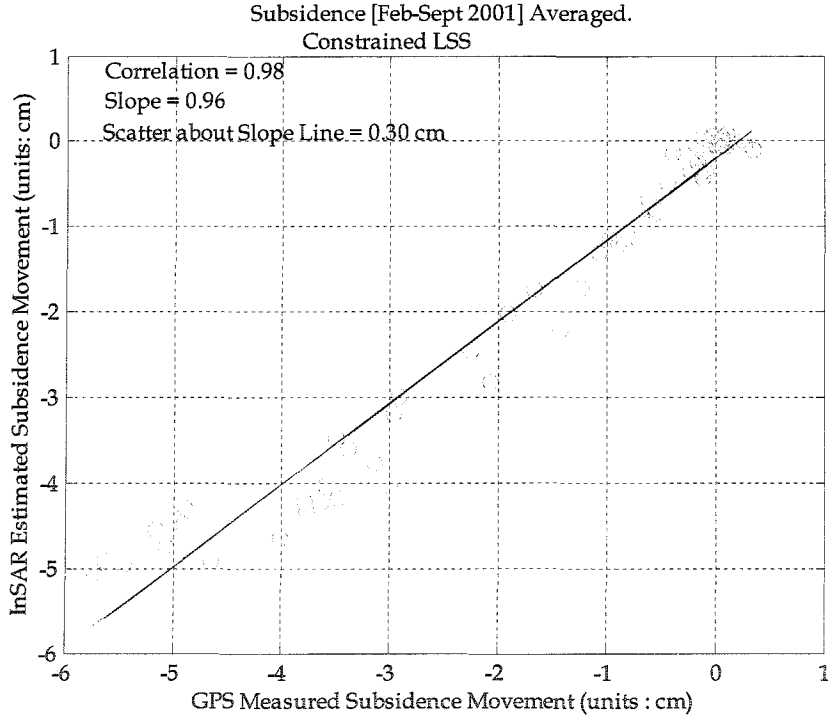

Figure 4-57: Comparison of averaged subsidence ground movement from [Feb-Sept 2001] with constrained LSS solution.

With the use of the constrained least squares method, 3-D ground movement estimation was verified from two satellite-look directions with additional assumptions. The obscurity that was encountered in estimating the inadequately measured component, which is North-South, was handled reasonably well with the constrained least squares technique. Subsidence and East-West movement estimation has also improved to near perfect slope and correlation with this method. Thus under the framework of natural-hazard monitoring, DInSAR combined with the derived fusion technique can be employed to monitor ground movement activity in remote locations, exploiting the unchallenged spatial coverage provided by satellite based remote sensing.

Chapter 5

Conclusion and Recommendations for Future Work

In the context of deriving 3-D ground movement from SAR, a technique for fusing data from ascending/descending pass SAR images in order to extract directional ground movement has been derived and successfully validated especially for East-West movement and Subsidence. The results give an excellent indication of the capability of DInSAR to measure 2-D ground movement. In addition, the technique derived to extract 3-D ground movement demonstrated the existence of a linear trend between DInSAR estimated lateral ground movements and GPS estimated ground movements. The results of the constrained Least Squares Solution (LSS) illustrated in Figures 4-55, 4-56 and 4-57 have a correlation coefficient of 0.87, 0.64 and 0.98. This suggests a good correlation between DInSAR and GPS derived ground movement for East-West,

North-South and Subsidence. The results for extracting East-West movement showed an excellent correlation of 0.87, especially for the averaged results shown in Figure 4-55. In addition, the technique improves the vertical measurements to near perfect correlation of 0.98 with GPS. The North-South movement also showed promising correlation. However, it demonstrates the need for averaging of interferograms to reduce the overall errors. Varying the incidence angle from the center of the SAR scene to the total image area as described in Figure 3-10 helped formulate the over-determined system in Section 3.3. Over a single scene, the variation of incidence angle is about a degree or two. The pattern of inter-correlation among the coefficients makes the M'*M system matrix nearly singular, which, makes estimation of the LSS imprecise for the non-measured component. This problem can be overcome by using a constrained least squares technique that demonstrates substantially improved results. Overall, it can be said that the technique provides a much improved subsidence estimate and a very favorable East-West movement estimate.

There are various limitations to SAR interferometry and the fusion technique discussed here can be applied to mitigate these limitations. Steep slopes facing the SAR look direction cannot always be monitored due to foreshortening or layover. However, research has shown that, for east-west facing slopes, fusing ascending and descending pass images can mitigate this problem. DInSAR, as illustrated in Chapter 4 is not sensitive at all to the ground

movement component along-track. However, in this thesis it was shown that by combining ascending and descending data, it is possible to accurately estimate two components of the deformation and possibly estimate the third component if it is at all present.

Future work in this area should include the examination of the possibility of fusing multiple look directions obtained from different satellites for generating the DInSAR pair. This would enable the derivation of an over-determined system from other satellite look directions. Additional beam positions from the same satellite that provide slightly different viewing geometry may also prove useful. Though it is not possible to find another completely unique and orthogonal viewing perspective from present satellite interferometry, fusing interferometric data with GPS data would be an interesting investigation.

More work can be done to validate the fusion technique presented in this thesis on other regions undergoing ground movement. Using data sets from different terrain configuration and ground movement characteristics can be used. The idea that homogeneous ground movement improves estimation of results could be verified by using new datasets of San Joaquin valley and performing analysis similar to that presented in this work. However, the ideas presented in this thesis can be applied to a broad range of satellite-based ground movement monitoring assignments in reasonably flat areas.

Bibliography

[1] Integrated Global Observing Strategy, Theme Report 2003 "Monitoring of our Environment from Earth and Space."

[2] Y. Chen, G. Zang, X. Ding, Z. Li, "Monitoring Earth Surface Deformations with InSAR Technology," Journal of Geospatial Engineering, Vol. 2, No. 1, June 2000, pp. 3-21.

[3] R.Ajalloeian, B.Bahadoran, "Ground Subsidence due to Percolating and Pumping Water (Case Studies in Iran)," Conference Proceedings Asian Conference on Remote Sensing, November 1998, Manila.

[4] X.Ding, H.Qin, "Geotechnical Instruments in Structural Monitoring," Journal of Geospatial Engineering, Vol 2, No. 1, June 2000, pp. 50-55

[5] J.Youden, D.Power, P.Han, J.English, R.Gailing, M. Rizkalla, "Satellite-based monitoring of subsidence ground movement impacting pipeline Integrity," Proceeding of International Pipeline Conference, September 29 2003, Calgary, Canada.

[6] P.E. Mikkelsen, "Field Instrumentation In Land Slides Investigation and Mitigation", Transportation Research Board Special Report 247. National Academy Press, DC, 1996, pp 278-316.

[7] J.R. Klauder, A.C. Price, S. Darlington and W.J. Albersheim, "The Theory and Design of Chirp Radars," The Bell System Technical Journal, Vol. 39, No. 4, July 1960.

[8] J. Ward, "Space-time adaptive processing for airborne radar," Tech. Rep. TR-1015, MIT Lincoln Labs, Dec 1994.

[9] D. Massonnet, R. Thierry, "Radar Interferometry: Limits and Potential," IEEE Transactions on Geosciences and Remote Sensing, Vol. 31, No. 2, March 1993, pp 455-464.

[10] K. Kramer, "Observation of the Earth and Its Environment Survey of Missions and Sensors," 2nd Ed., Springer-Verlag Berlin Heindelberg, Germany, 1994.

[11] R. Gens, J.L. Genderen, "SAR interferometry - issues, techniques, applications." International Journal of Remote Sensing, Vol. 17, No. 10, 1996, pp 1803-1835.

[12] R. Gens, "Quality assessment of interferometrically derived digital elevation models," International Journal of Applied Earth Observation and Geo-information, Vol. 1, No. 2, 1999, pp 102-108.

[13] O. Bombaci, F. Impagnatiello, A. Torre, "Science results from the spaceborne imaging radar-C/X-Band synthetic aperture radar (SIR-C/X-SAR)," Report Edited by D.L. Evans and J.J. Plaut, URL http://southport.jpl.nasa.gov/ProgressReports0496/Bombaci.Edited.htm.

[14] C. Prati, F. Rocca, Y. Kost, and E. Damonti, "Blind Deconvolution for Doppler Centroid Estimation in High Frequency SAR," IEEE Transactions on Geoscience and Remote Sensing, Vol. 29, No. 6, November 1991, pp 934-941.

[15] C. Curlander, R.N. McDonough, "Synthetic Aperture Radar - Systems and Signal Processing," John Wiler and Sons, New York, 1991.

[16] Trevett J. W, "Imaging radar for resources surveys," University Press, Cambridge, UK, 1986.

[17] H.A. Zebker and R.M. Goldstein, "Topographic Mapping From Interferometric Synthetic Aperture Radar Observations," Journal of Geophysical Research, Vol. 91, 1986, pp , 4993-4999.

[18] C. Ichoku, A. Karnieli, Y. Arkin, J. Chorowicz, T. Fleury, J.P. Rudant, "Exploring the potential of SAR interferometric coherence images," International Journal of Remote Sensing, vol. 19, No. 6, 1998, pp. 1147-1160.

[19] A.K. Gabriel, R.M. Goldstein. H.A. Zebker, "Mapping small elevation changes over large areas: differential radar interferometry," Journal of Geophysical Research, Vol. 94, No B7, 1989, pp.9183-9191.

[20] J. Askne, J. J. Hagberg, "Potential of Interferometric SAR for Classification of Land Surfaces," Proceedings of IGARSS'93, Tokyo, 18-21 August 1993, pp. 985-987.

[21] S. Baronti, D. Frate, F. Frrazzoli, P.Paloscia, S. Pampaloni, P.G. Sviciavon, "SAR polarimetric features of agricultural areas, " International Journal of Remote Sensing, Vol. 16, No 14, 1995, pp 2639-2656.

[22] J. Askne, P.B.G. Dammert, J. Fransson, H. Israelsson, L.M. Ulander, "Retrieval of forest parameters using intensity and repeat-pass interferometric SAR information," Proceedings of Retrieval of Bio and Geophysical Parameters from SAR Data for Land Applications, Toulouse, 10-13 October 1995.

[23] S. Paloscia, "A summary of experimental results to assess the contribution of SAR for mapping vegetation biomass and soil moisture," Canadian Journal of Remote Sensing, Vol.28, No.2, 2002, pp.246-261.

[24] R.M. Goldstein, H.A. Zebker, "Interferometric Radar Measurement of Ocean Surface Currents," Nature, Vol. 328, 1987, pp 707-709.

[25] C. Prati, F. Rocca, "Limits to the resolution of elevation maps from stereo SAR images," International Journal of Remote Sensing, Vol. 11, No 12, 1990, pp 2215-2235.

[26] L. Timmen, X. Ye, C. Reigber, R. Hartmann, T. Fiksel, W. Winzer, J. Knoch-Weber, "Monitoring of Small Motions in Mining Areas by SAR Interferometry," Fringe1996.
Url http://www.geo.unizh.ch/rsl/fringe96/papers/timmen-et-al/.

[27] C. Prati, F. Rocca, A.M. Guanieri, "Effects of speckle and additive noise on the altimetricresolution of interferomteric SAR (ISAR) surveys," International Geoscience and Remote Sensing Symposium, Vancouver, 1989, pp 2469-2472.

[28] C. Cafforio, C. Prati, F. Rocca, "SAR Data Focusing using seismic migration techniques," IEEE Transaction on Aerospace and Electronic Systems, Vol. 27, No 2, 1991, pp 194-207.

[29] F.K. Li, R.M. Goldstein, "Studies of multibaseline space borne interferometric synthetic aperture radars," IEEE Transactions on Geosciences and Remote Sensing, Vol. 28, 1990, pp 88-97.

[30] C. Prati, F. Rocca, "Use of the spectral shift in SAR interferometry," Proceedings-2 Second ERS - 1 Symposium, 1993.

[31] F. Gatelli, A.M. Guarnieri, F. Parrizzi, P. Pasquali, C. Prati, F. Rocca, "The Wavenumber Shift in SAR Interferometry," IEEE Transaction on Geoscience and Remote Sensing, Vol. 32, No. 4, July 1994.

[32] D. Massonnet, M. Rossi, C. Carmona, F. Adragna, G. Pletzner, K. Feigl, "The displacement field of the Landers earthquake mapped by radar interferometry," Nature, Vol 364, 8 July 1993, p 138 - 142.

[33] R. M. Goldstein, H. Engelhardt, B. Kamb, and R. M. Frolich, "Satellite Radar Interferometry for Monitoring Ice Sheet Motion: Application to an Antarctic Ice Stream," Science, Vol. 262, December 1993, pp. 1525-1530.

[34] L. Ge, S. Han and C. Rizos, "Interpolation of GPS results incorporating geophysical and InSAR information," Earth, Planets and Space, Vol. 52, No. 11, 2000 ,pp 999-1002.

[35] L. Ge, C. Rizos, S. Han & H.A. Zebker, "Mine subsidence monitoring using the combined InSAR and GPS approach," 10th FIG Int. Symp. on Deformation Measurements, Orange, California, 19-22 March 2001.

[36] D. Small, D. Nuesch, "Validation of Height Models from ERS Interferometry," proceedings of ESA-Fringe 1996 Work Shop, Zurich, Switzerland, September 1996.

[37] Q. Lin, J.F. Vesecky, H.A. Zebker, "New Approaches in Interferometric SAR Data Processing," IEEE Transactions on Geosciences and Remote Sensing, Vol. 30, No. 3, May 1992, pp 560.

[38] C. Ichoku, A. Karnieli, Y. Arkin, J. Chorowicz, T. Fleury, J.-P. Rudant, "Exploring the potential of SAR interferometric coherence images, International Journal of Remote Sensing," Vol. 19, No. 6, 1998, pp. 1147-1160.

[39] H.A. Zebker, J. Villasenor, "Decorrelation in Interferometric Radar Echoes," IEEE Transactions on Geoscience and Remote Sensing, Vol.30, No.5, September 1992, pp 950.

[40] A.K. Gabriel, R.M. Goldstein, "Crossed orbit interferometry theory and experimental results from SIR-B," International Journal of Remote Sensing and Geosciences, Vol. 9, No. 5, 1988, pp 857-872.

[41] R. Rodriquez, J.M. Martin, "Theory and design of interferometric synthetic aperture radars," IEEE Proceedings-F Vol. 139, No. 2, 1992, pp 147-159.

[42] R. Gens, "Quality assessment of interferometrically derived digital elevation models," International Journal of Applied Earth Observation and Geo-Information, Vol. 1, No. 2, 1999, pp 102-108.

[43] Z. Bai, H. Zha, "A new preprocessing algorithm for the computation of the generalized singular value decomposition," SIAM Journal of Scientific Computing, Vol. 14, 1993, pp 1007-1012.

[44] N.N. Abdelmalek, "On the solution of the linear least squares problems and pseudo-inverses," Computing, Vol. 13, No. 3, 1974, pp-215-228.

[45] N.J. Higman, "Accuracy and Stability of Numerical Algorithms," Society for Industrial and Applied Mathematics, Philadelphia, First Edition, 1996.

[46] A. Bjorck, "Numerical Methods for Least Squares Problem," SIAM Journal of Scientific Computing, 1996.

[47] O. Hellwich, H. Ebner, "Geocoding SAR interferograms by least squares adjustment," PandRS, Vol 55, No. 4, November 2000, pp 277-288.

[48] H.A. Zebker, P.A. Rosen, R.M. Goldstein, A. Gabriel, and C.L. Werner, "On the derivation of coseismic displacement fields using differential radar interferometry: The Landers earthquake," Journal of Remote Sensing and Geophysics, Vol. 99, No. 19, 1994, pp 617-619.

[49] E.J. Fiekding, R. G. Blom, R.M. Goldstein, "Rapid subsidence over oil fields measured by SAR interferometry," Geophysical Research Letters, Vol. 25, No. 17, 1998.

[50] R. Hanssen, A. Feijt, "A first quantitative evaluation of atmospheric effects on SAR interferometry," Fringe 96, 1996.

[51] S. Sircar, D. Power, J. Youden, E. Gill, P. Han, "Lateral Movement Estimation from Space-borne Radar by Differential Interferometry," NECEC Proceedings, St. John's, Newfoundland, 2002.

Appendix A

Figures and explanations not included in text. [Validation of InSAR derived ground movement compared with GPS measured ground movement and InSAR sensitivity on the North-South direction.]

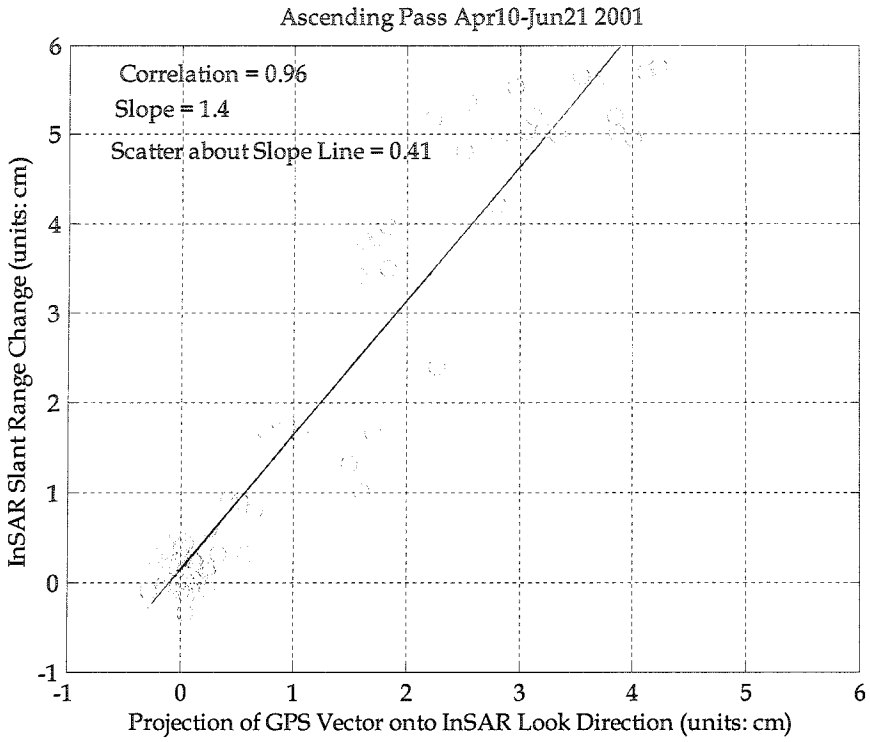

Figure A-1: InSAR SRC (cm) versus $\mathbf{G} \cdot \hat{A}$.

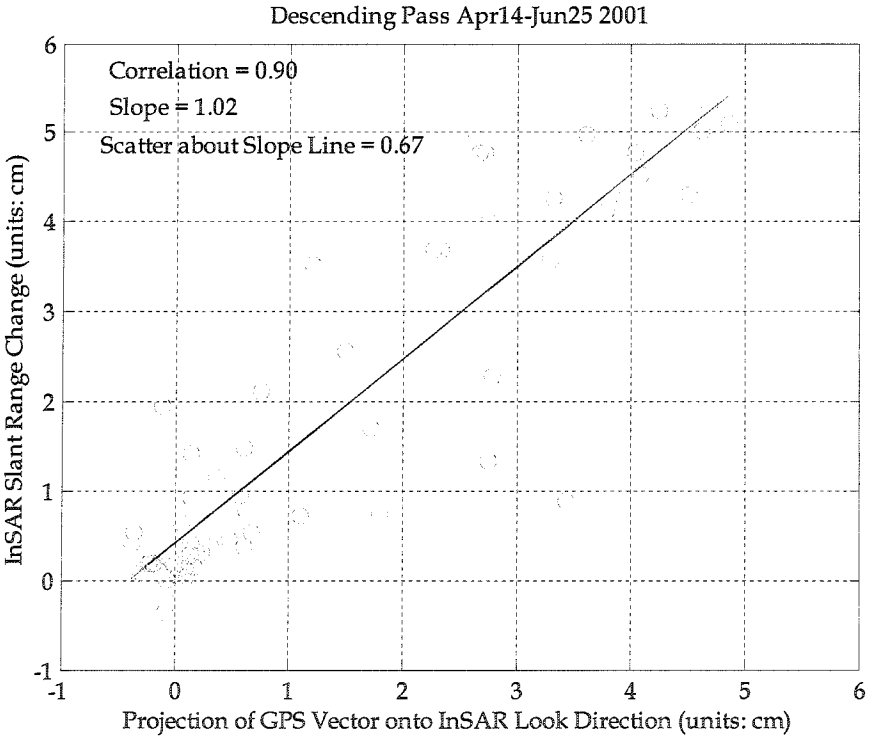

Figure A-2: InSAR SRC (cm) versus $\mathbf{G} \cdot \hat{D}$

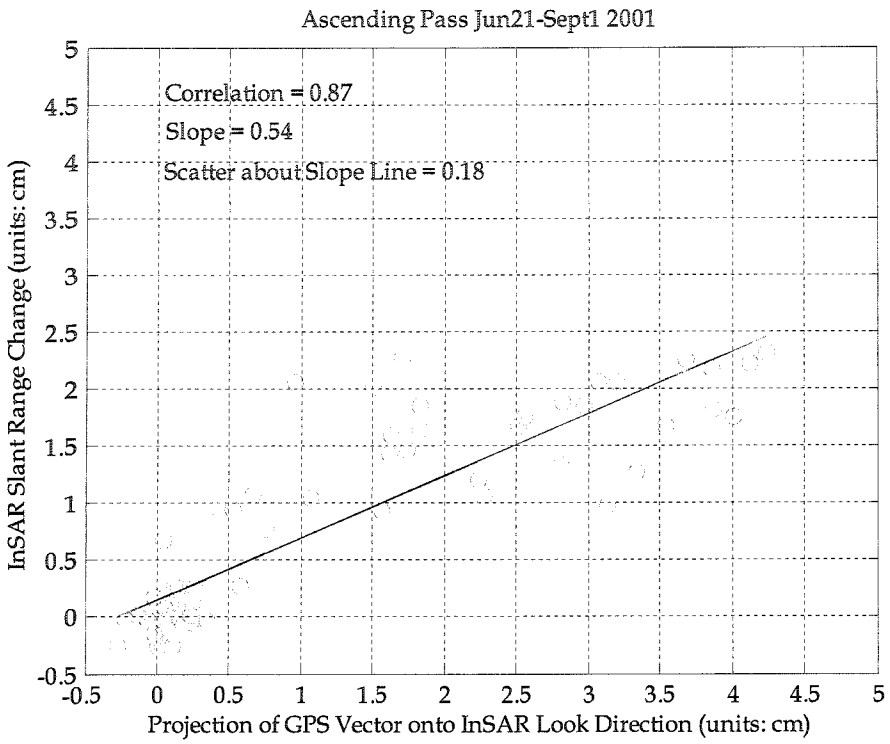

Figure A-3: InSAR SRC (cm) versus $\mathbf{G} \cdot \hat{A}$.

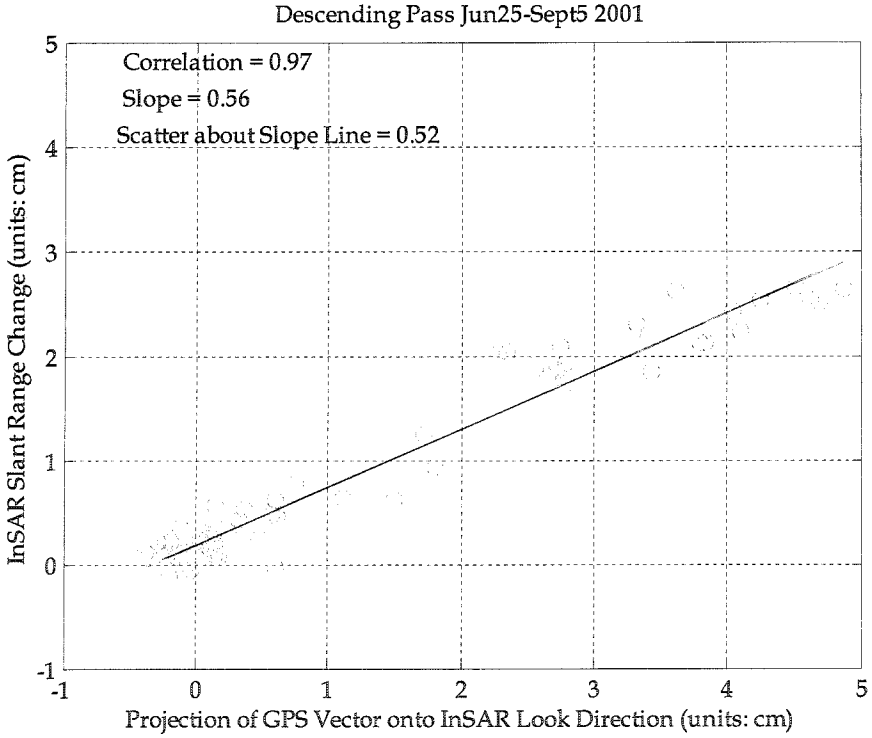

Figure A-4: InSAR SRC (cm) versus $\mathbf{G} \cdot \hat{D}$.

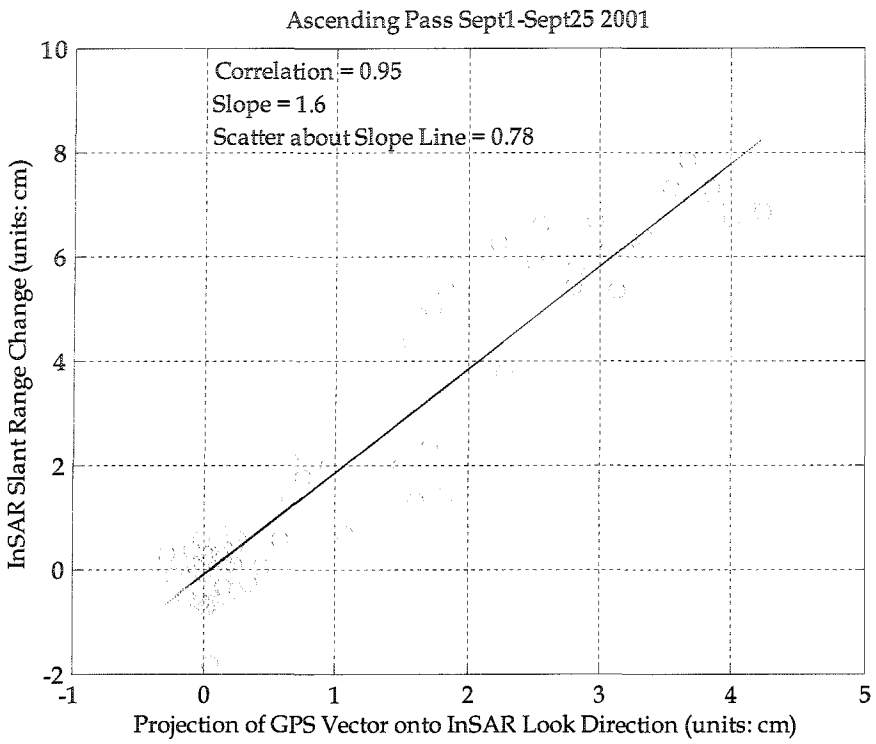

Figure A-5: InSAR SRC (cm) versus $\mathbf{G} \cdot \hat{A}$.

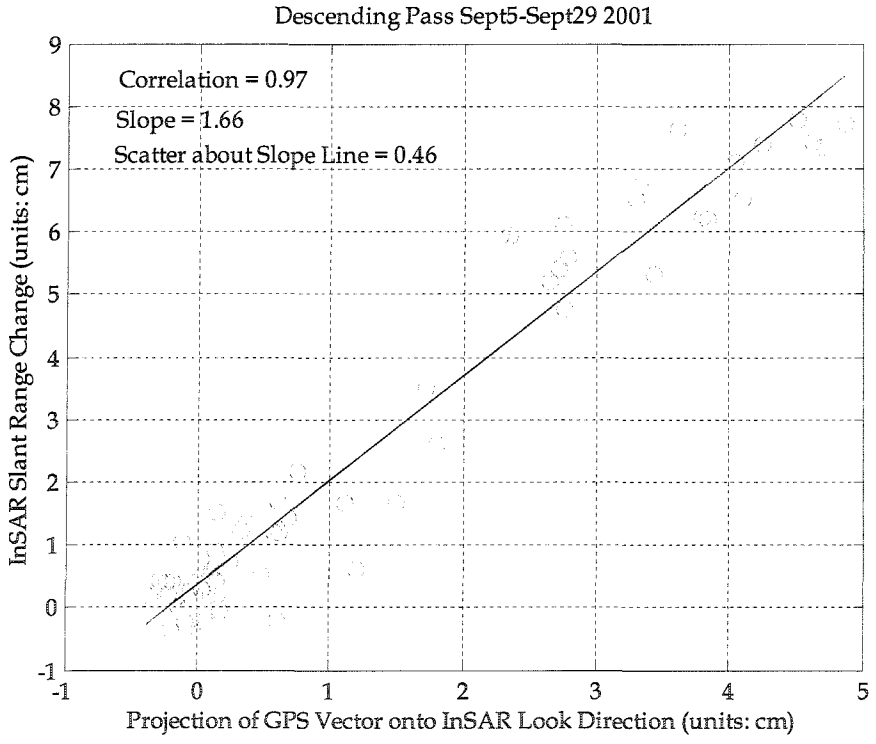

Figure A-6: InSAR SRC (cm) versus $\mathbf{G} \cdot \hat{D}$

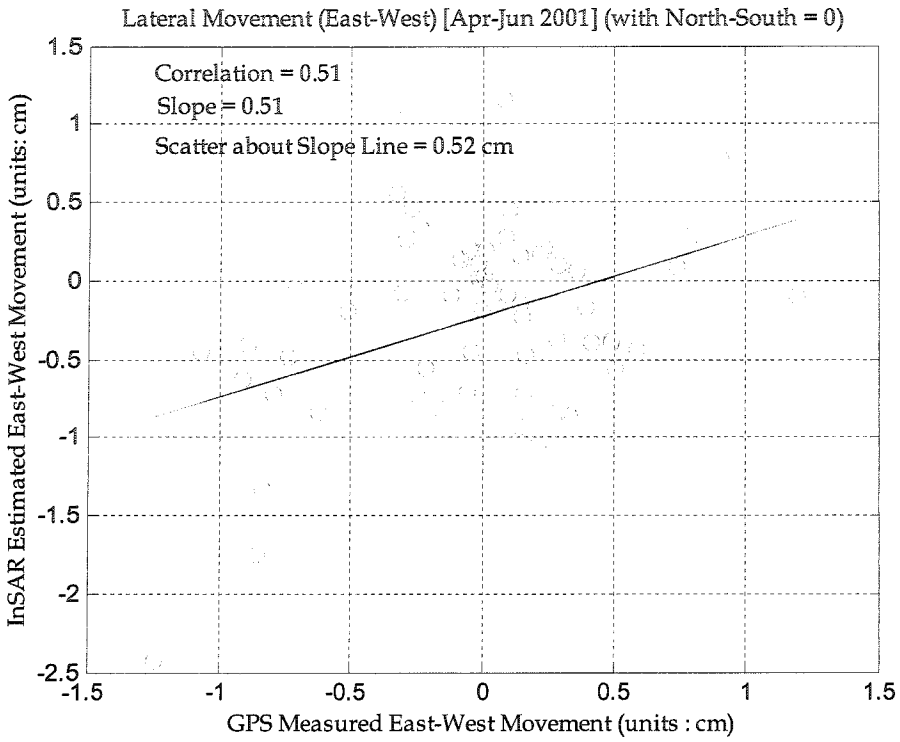

Figure A-7: InSAR versus GPS East-West normalized to 24 days from Apr-Jun 2001.

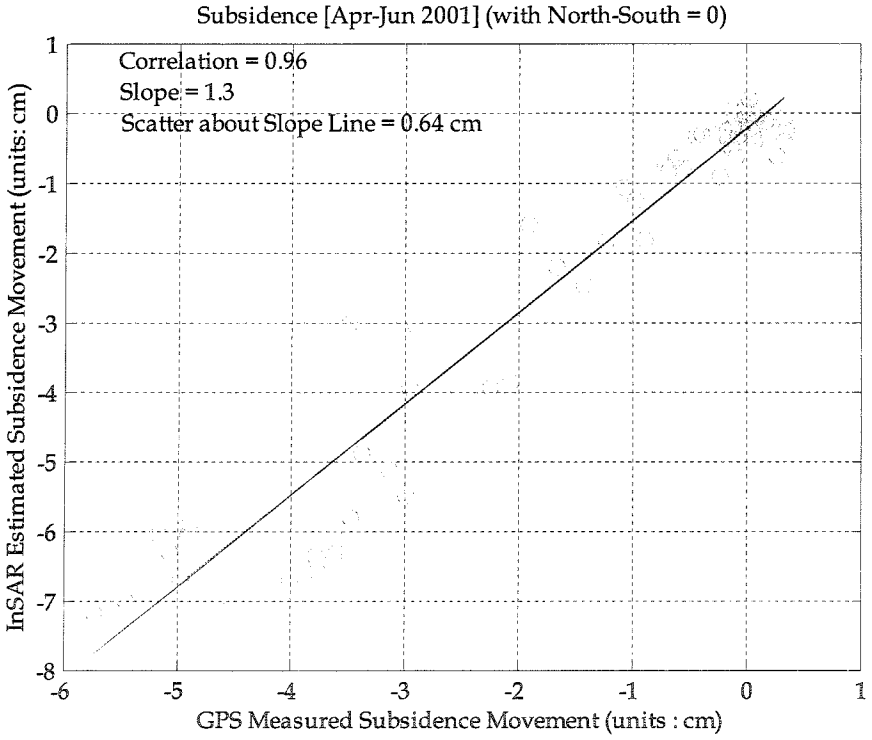

Figure A-8: InSAR versus GPS subsidence normalized to 24 days from Apr-Jun 2001.

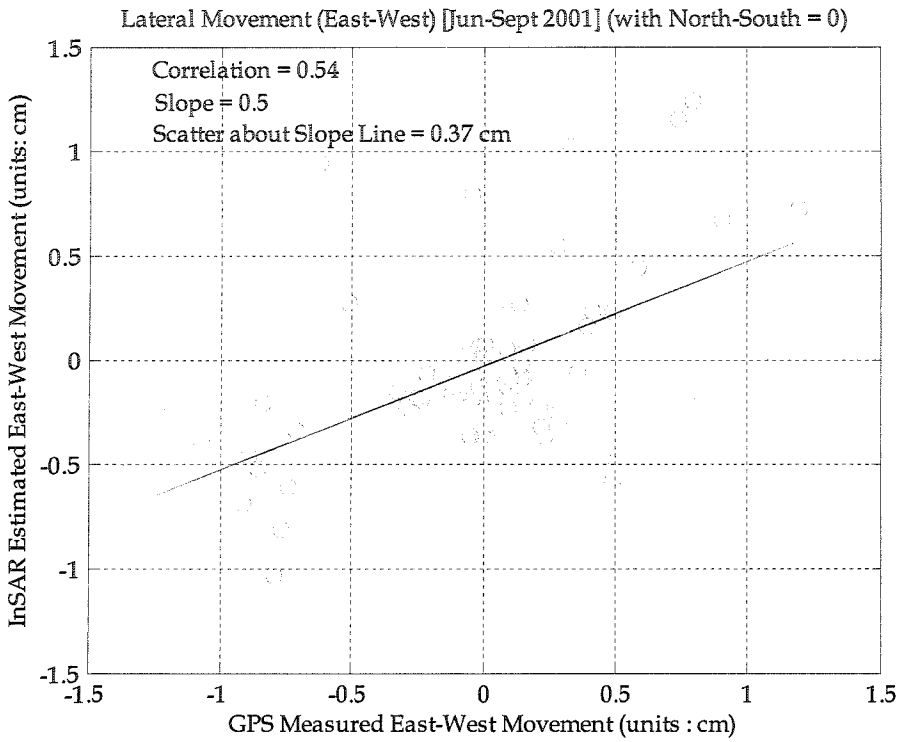

Figure A-9: InSAR versus GPS East-West normalized to 24 days from Jun-Sept[1st] 2001.

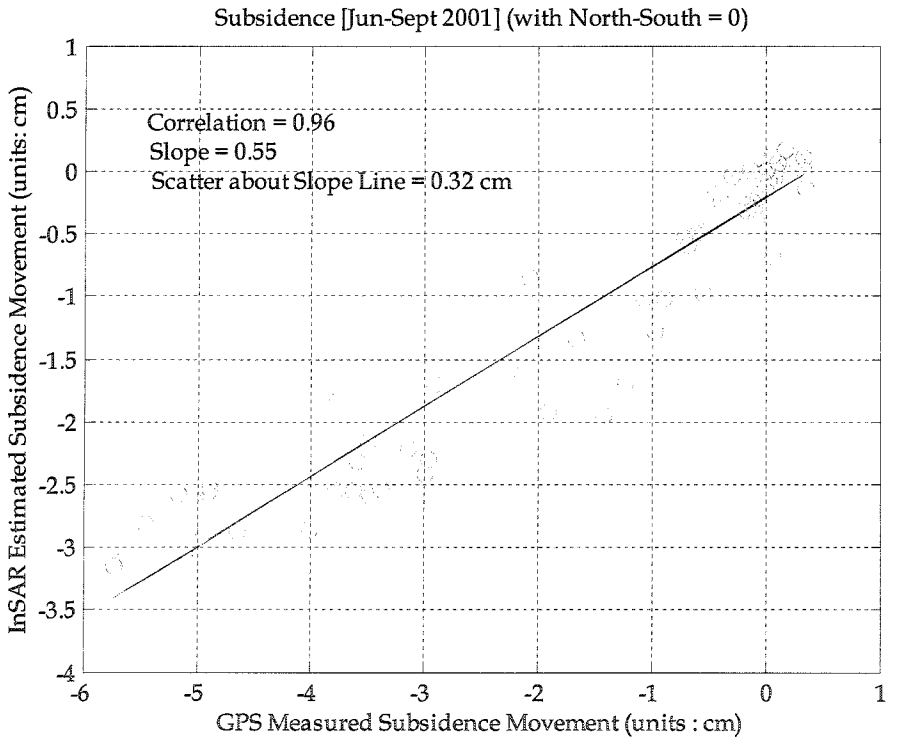

Figure A-10: InSAR versus GPS subsidence normalized to 24 days from Jun-Sept 1[st] 2001.

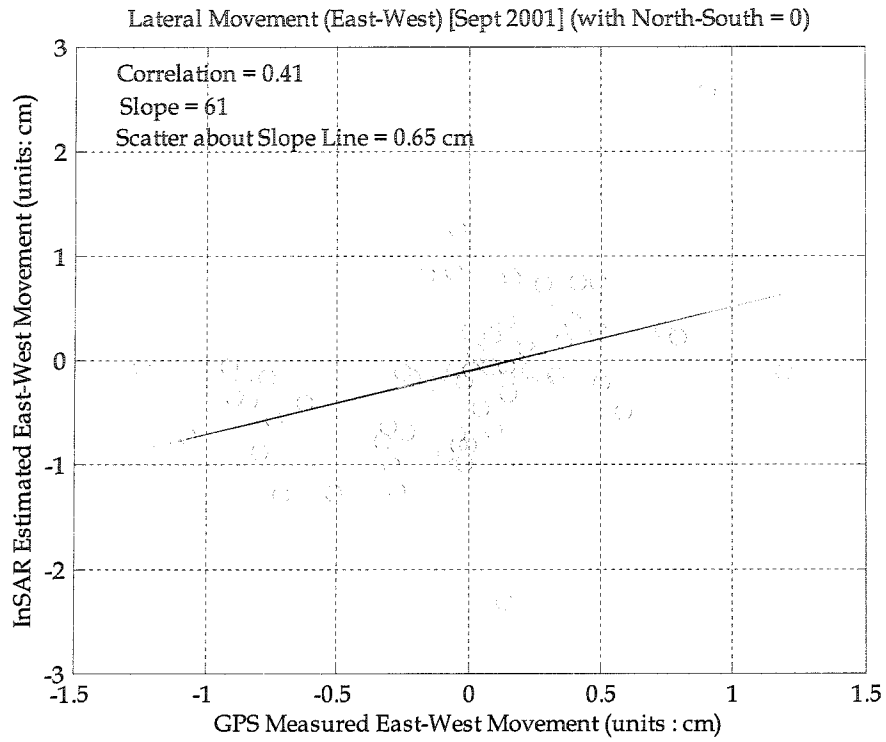

Figure A-11: InSAR versus GPS East-West normalized to 24 days from Sept 1st-Sept 25th 2001.

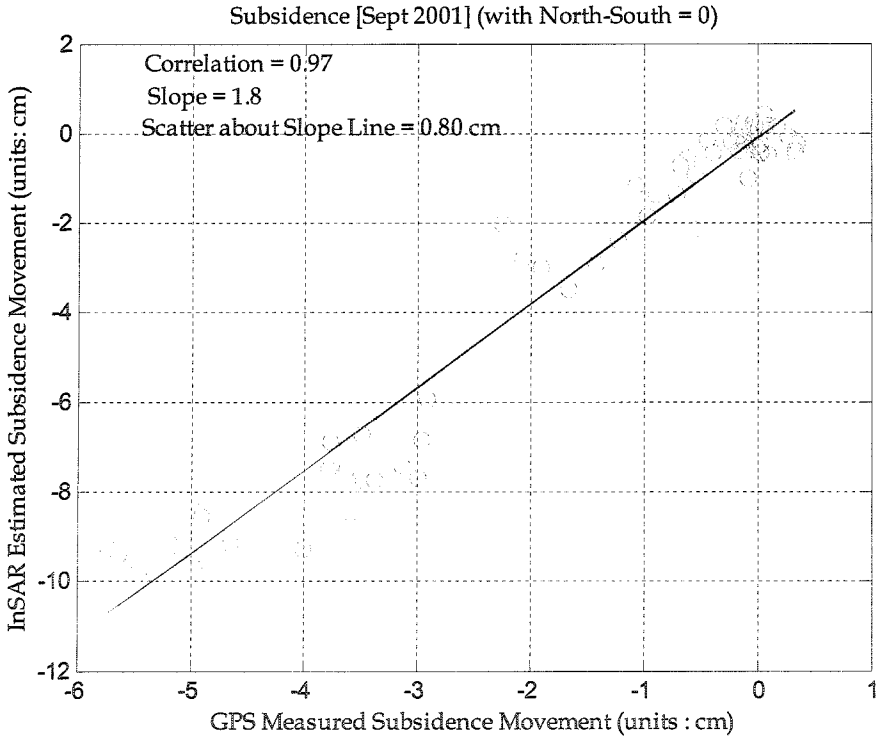

Figure A-12: InSAR versus GPS Subsidence normalized to 24 days from Sept 1st-Sept 25th 2001.

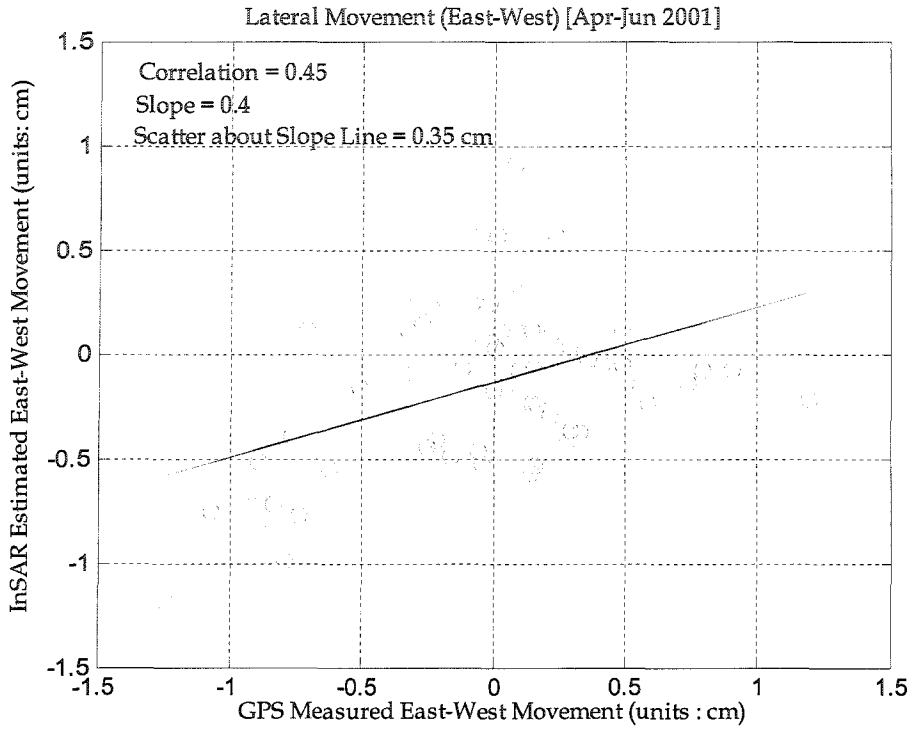

Figure A-13: InSAR versus GPS East-West normalized to 24 days from Apr-Jun 2001.

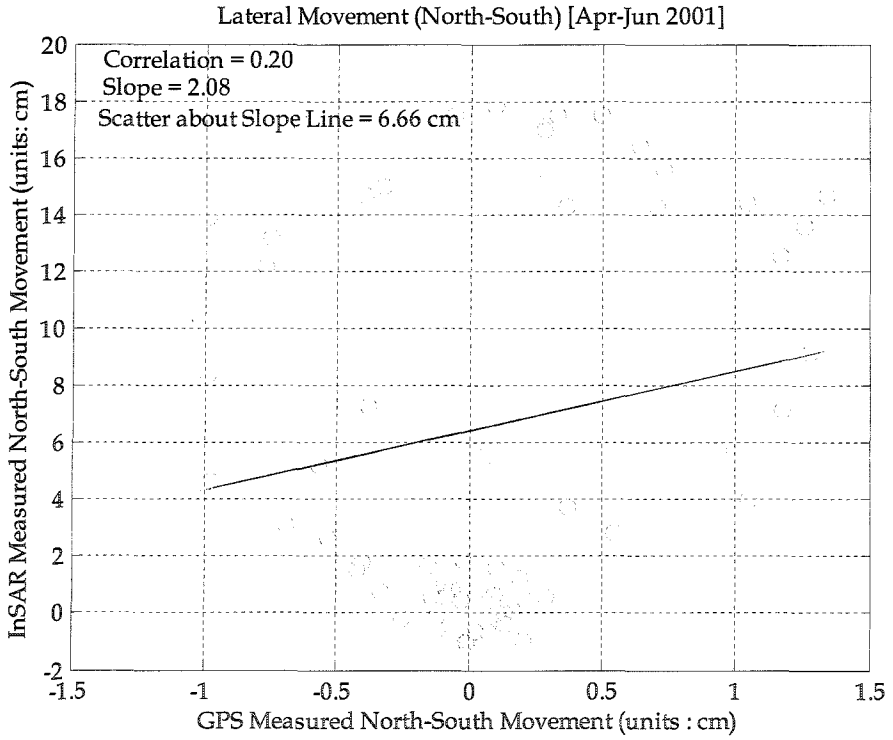

Figure A-14: InSAR versus GPS North-South normalized to 24 days from Apr-Jun 2001.

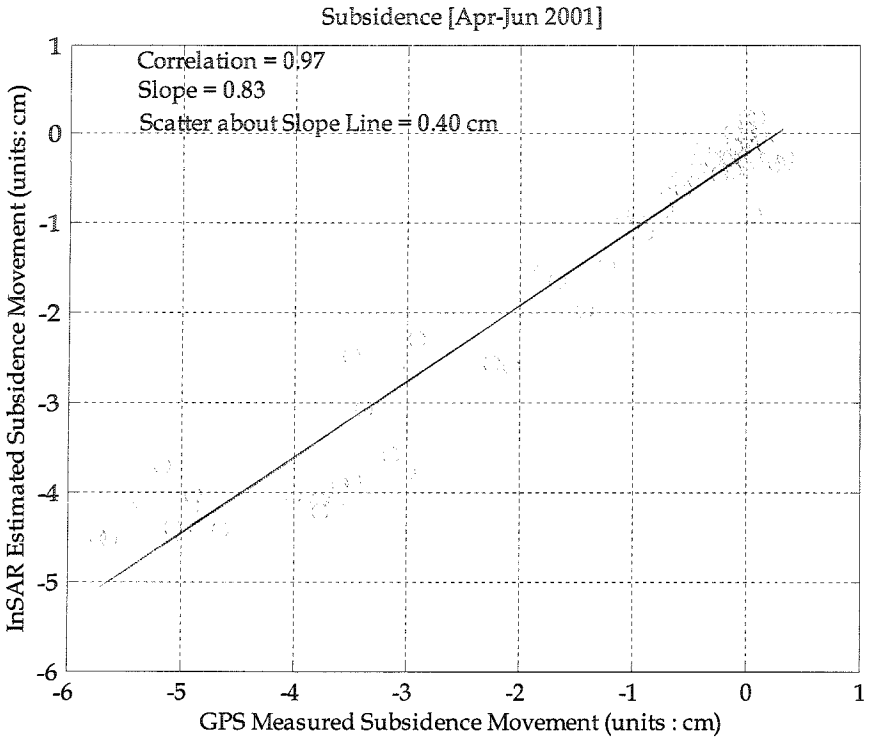

Figure A-15: InSAR versus GPS Subsidence normalized to 24 days from Apr-Jun 2001.

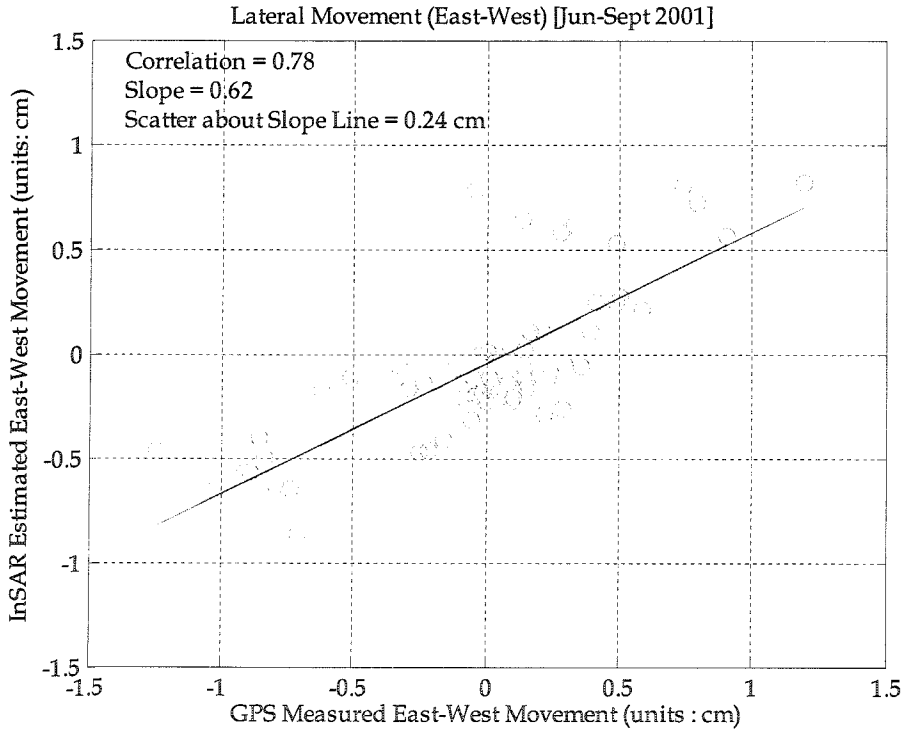

Figure A-16: InSAR versus GPS East-West normalized to 24 days from Jun- Sept 1st 2001.

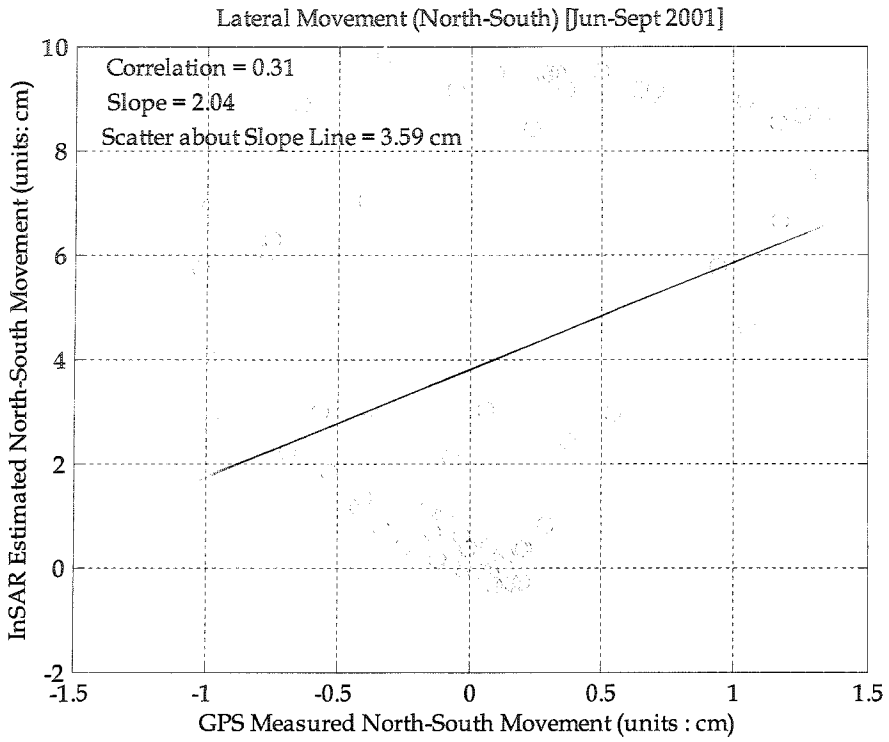

Figure A-17: InSAR versus GPS North-South normalized to 24 days from Jun- Sept 1st 2001.

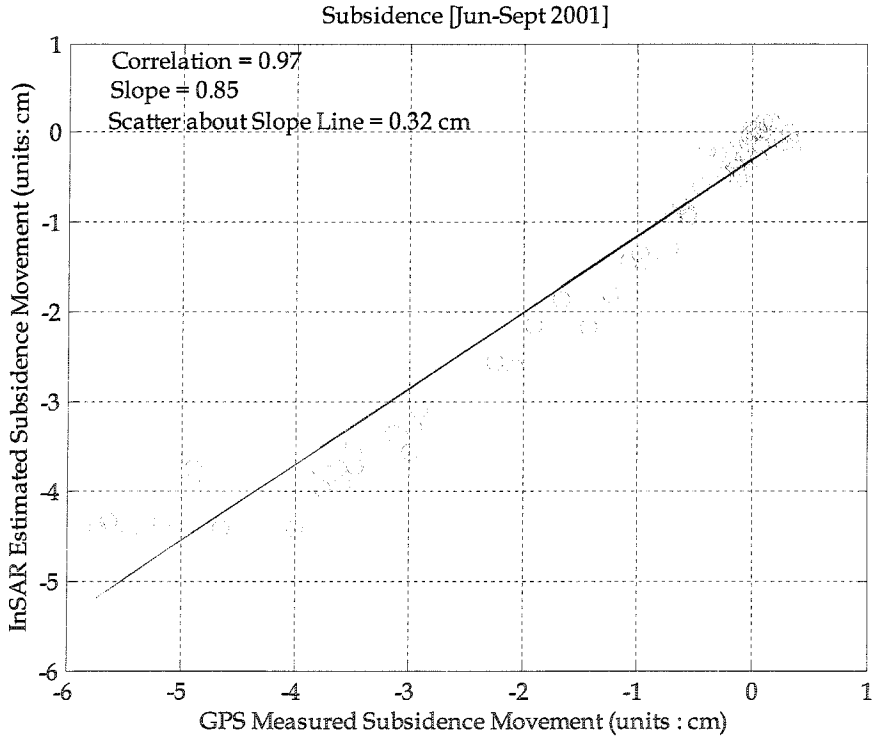

Figure A-18: InSAR versus GPS Subsidence normalized to 24 days from Jun- Sept 1st 2001.

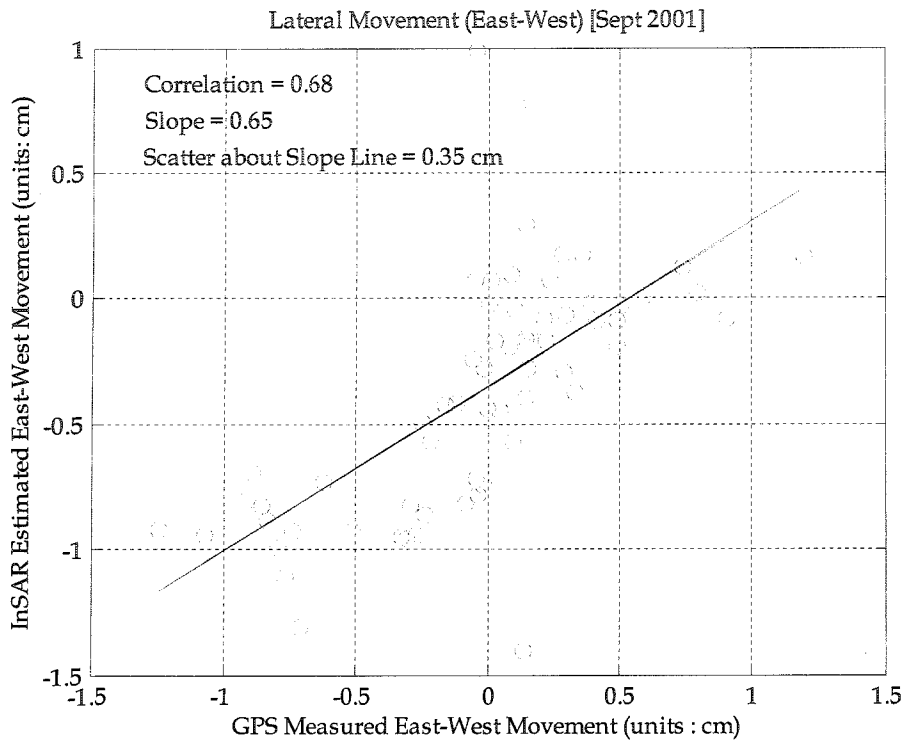

Figure A-19: InSAR versus GPS East-West normalized to 24 days from Sept 1st-Sept 25th 2001.

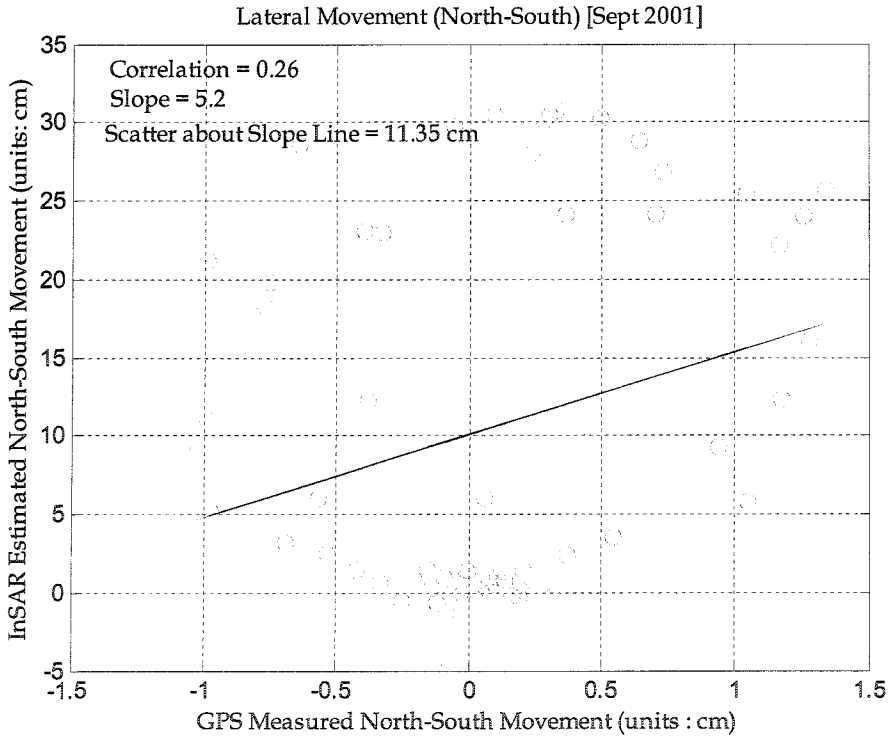

Figure A-20: InSAR versus GPS North-South normalized to 24 days from Sept 1st-Sept 25th 2001.

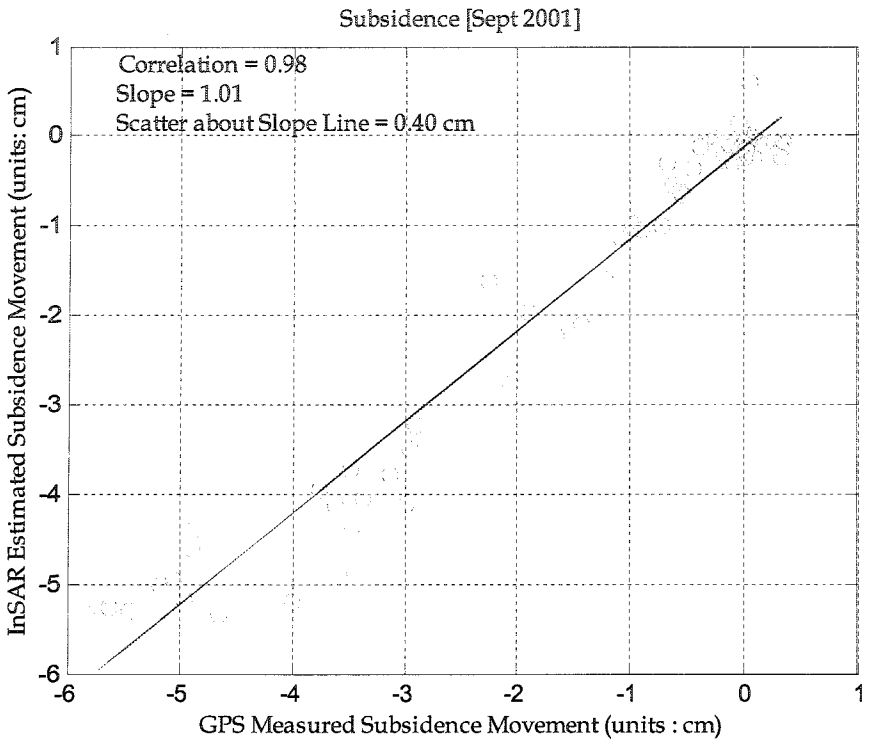

Figure A-21: InSAR versus GPS Subsidence normalized to 24 days from Sept 1st-Sept 25th 2001.

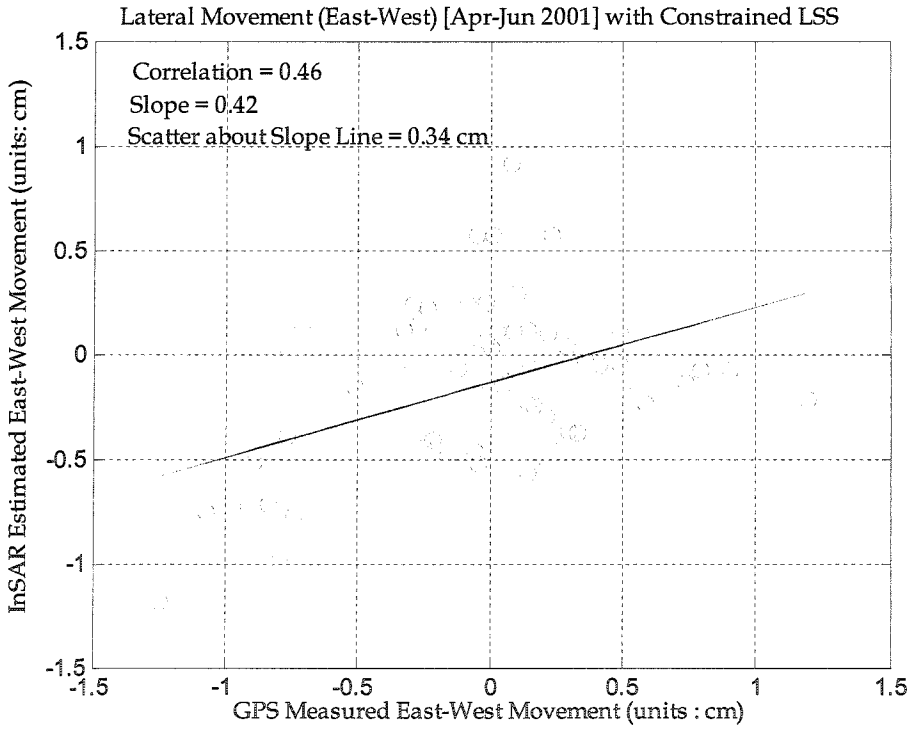

Figure A-22: InSAR versus GPS East-West normalized to 24 days from Apr-Jun 2001

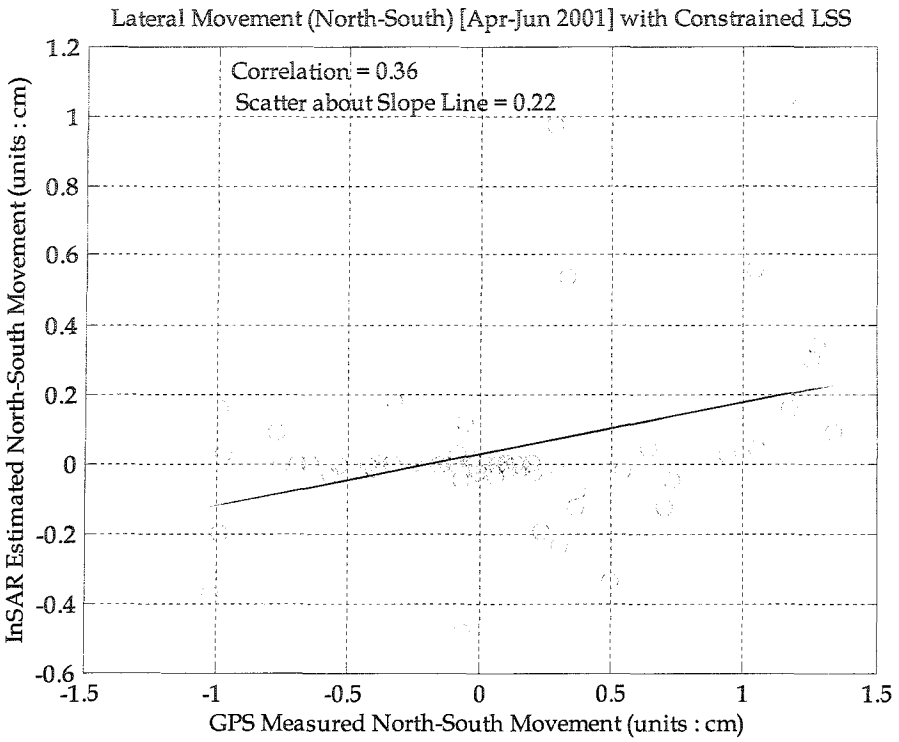

Figure A-23: InSAR versus GPS North-South normalized to 24 days from Apr-Jun 2001.

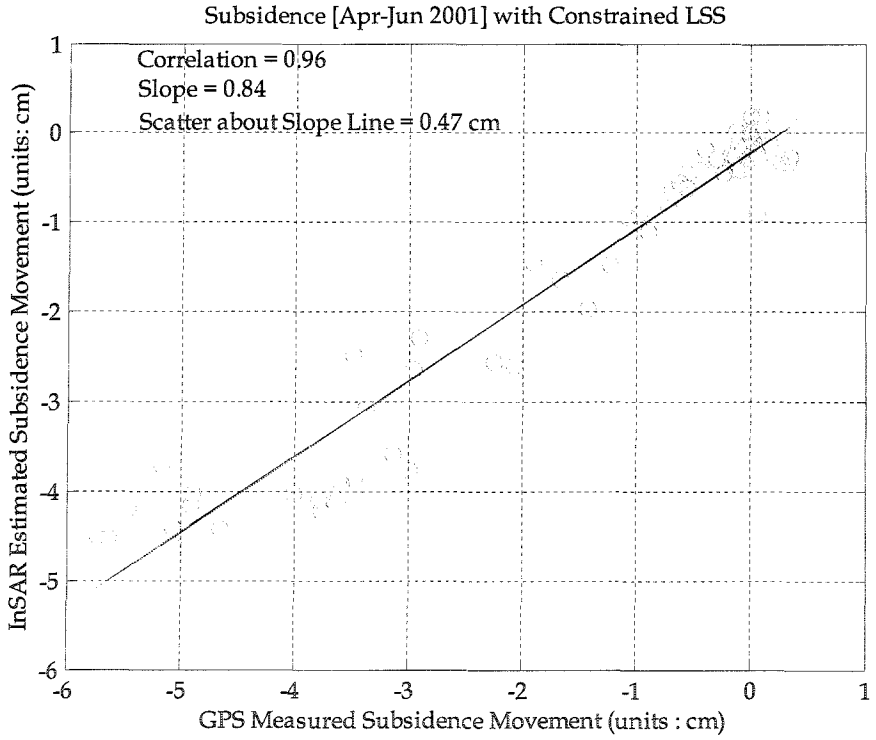

Figure A-24: InSAR versus GPS Subsidence normalized to 24 days from Apr-Jun 2001.

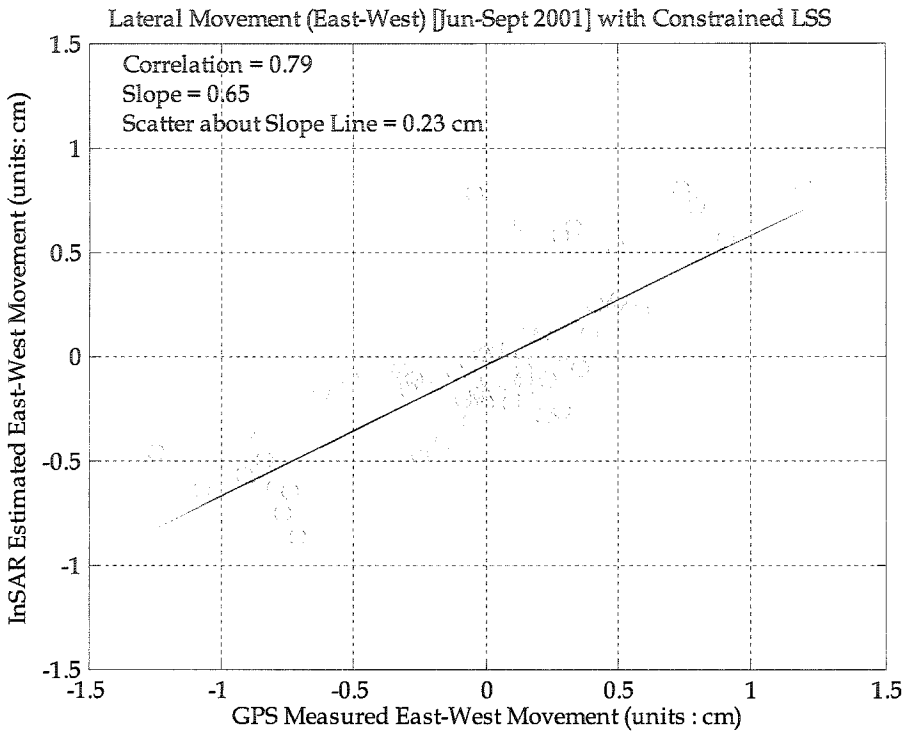

Figure A-25: InSAR versus GPS East-West normalized to 24 days from Jun- Sept 1st 2001.

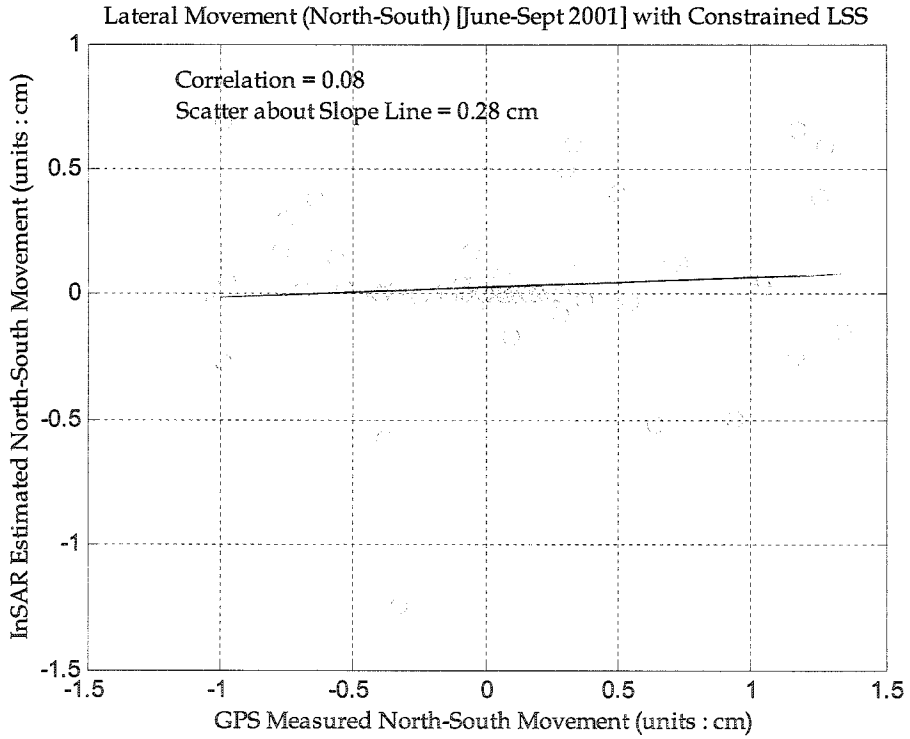

Figure A-26: InSAR versus GPS North-South normalized to 24 days from Jun- Sept 1st 2001.

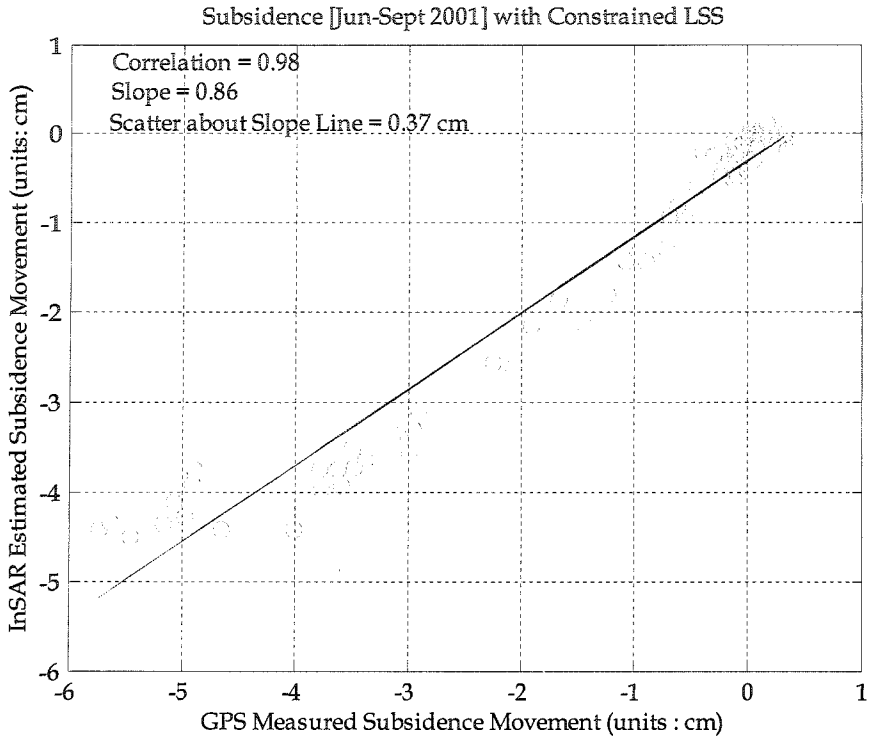

Figure A-27: InSAR versus GPS Subsidence normalized to 24 days from Jun- Sept 1st 2001.

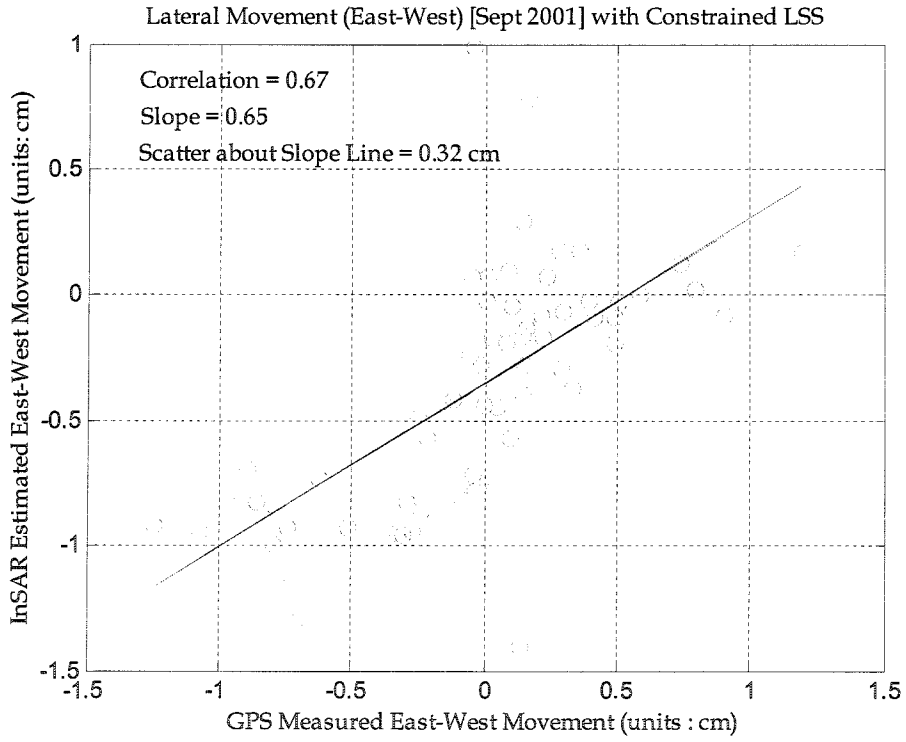

Figure A-28: InSAR versus GPS East-West normalized to 24 days from Sept 1st-Sept 25th 2001.

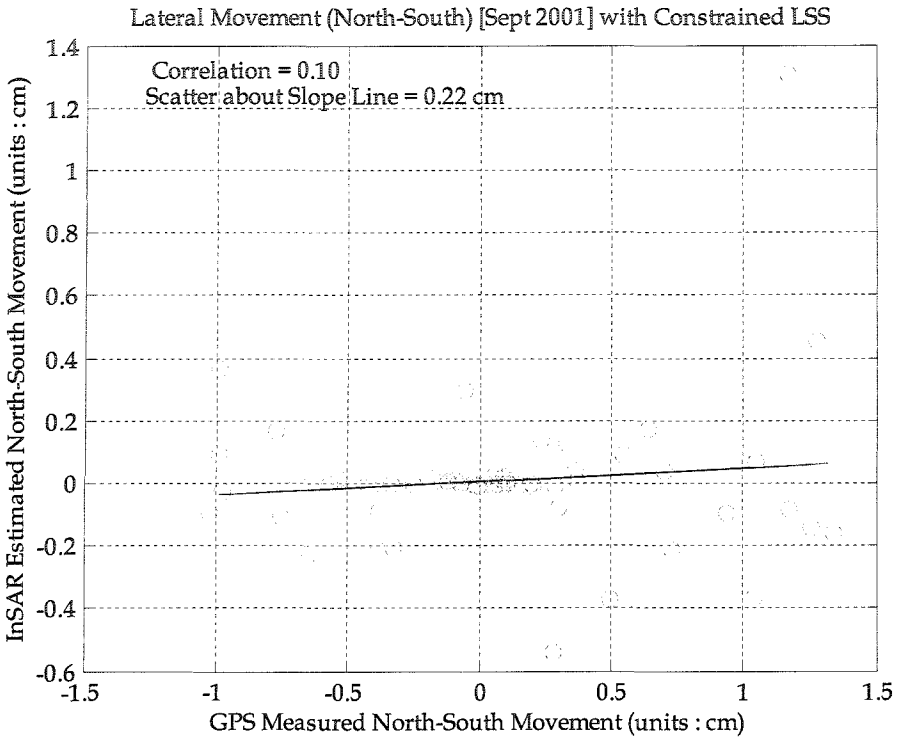

Figure A-29: InSAR versus GPS North-South normalized to 24 days from Sept 1st-Sept 25th 2001.

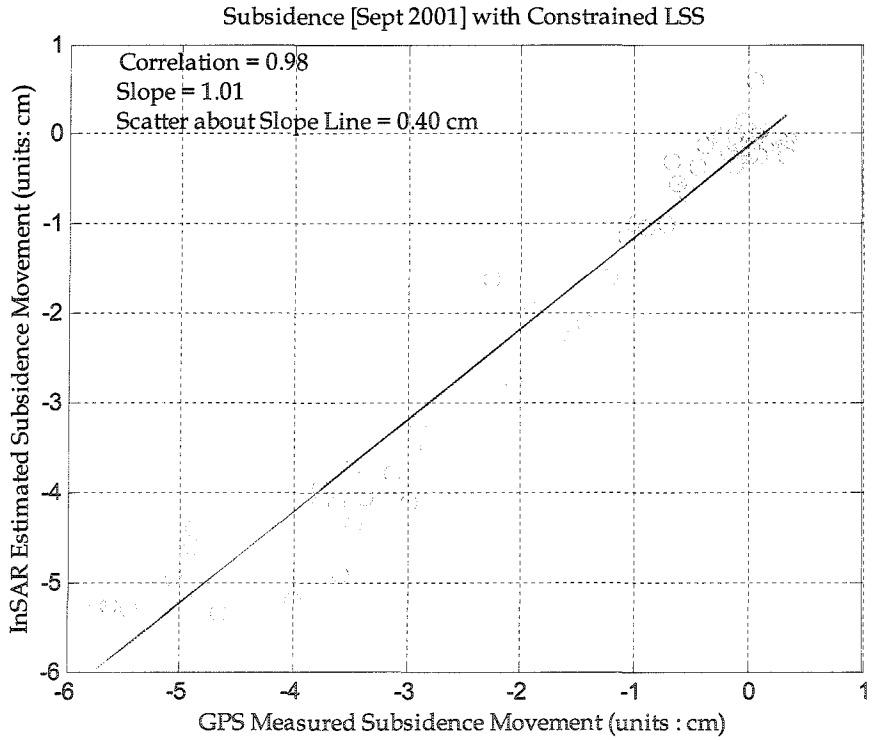

Figure A-30: InSAR versus GPS Subsidence normalized to 24 days from Sept 1st-Sept 25th 2001.

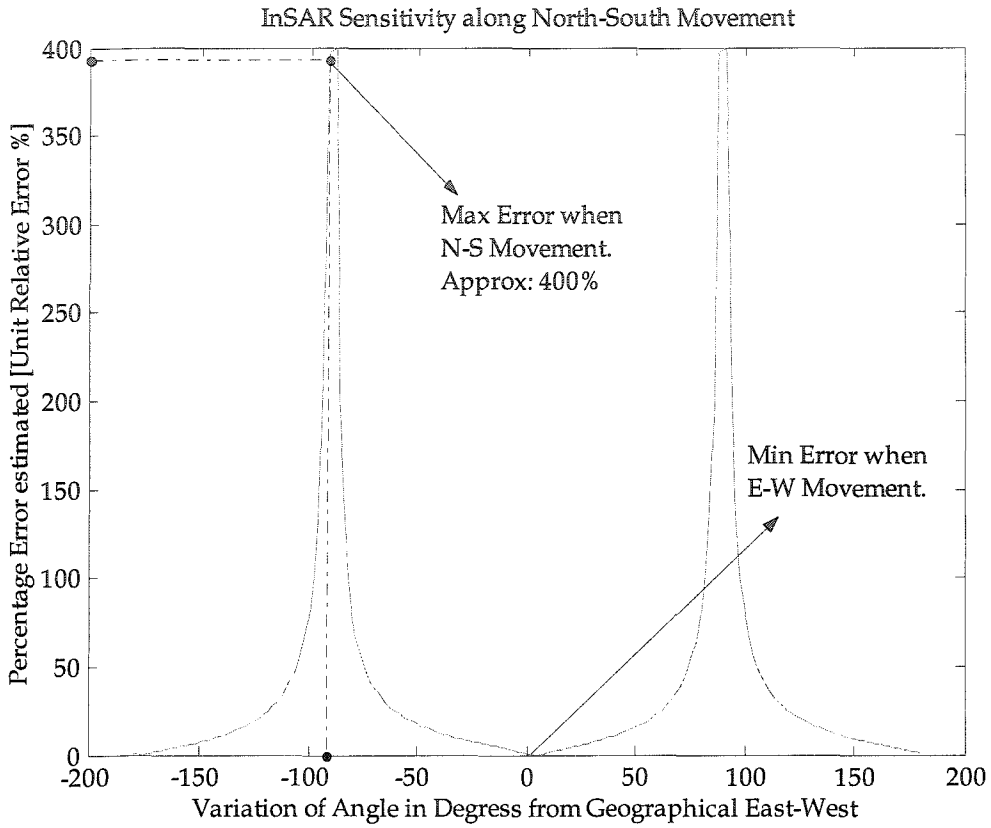

Figure A-31: InSAR Error Analysis. Estimated relative error in the North-South direction. This plot is based on satellite look direction and look angles projected to map co-ordinates.

The plot illustrates the results of sensitivity analysis of InSAR for movement vectors away from the InSAR look direction with a constant look angle of 38°. For a unit movement along the East-West direction identified as 0° in the plot, observed to have minimum error since that component of movement is along the InSAR look direction. As the movement vector deviates from the InSAR look direction to the negative maximum as complete southward movement, or to a positive maximum as complete northward movement the relative error also increases. The sensitivity drops and becomes completely insensitive to any movement along the azimuth vector that is North-South (i.e. movement is orthogonal to the look direction and SAR cannot measure it).

Appendix B

- DEM of San Joaquin Valley in Southern California
- SLC image draped over DEM showing San Joaquin Valley in Southern California
- 3-D subsidence and results not included in text

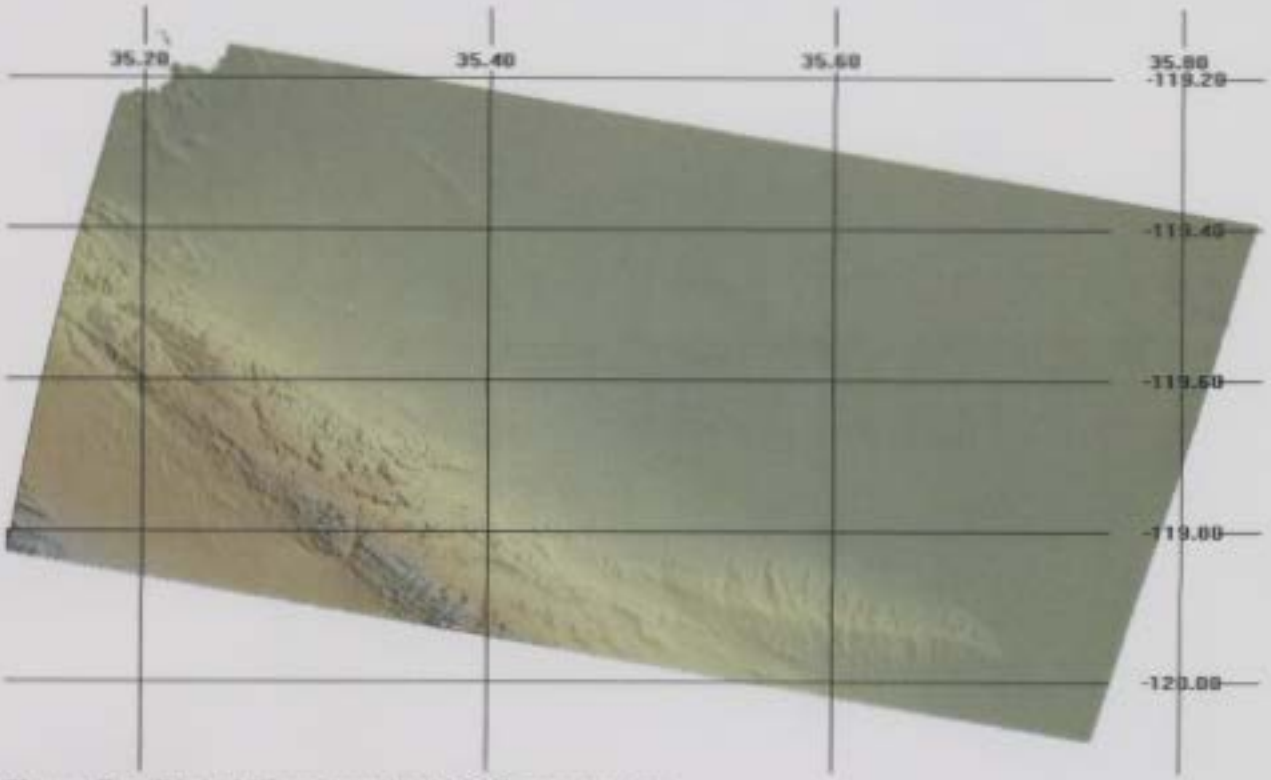

Figure B-1: Digital Elevation Model 90° perspective

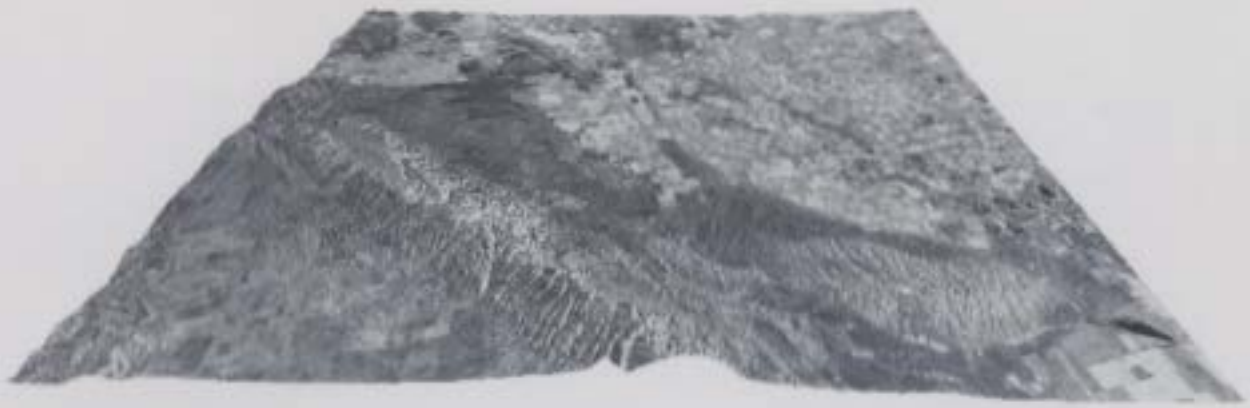

Figure B-2: Digital Elevation Model 45° perspective

Figure B-3: Digital Elevation Model 20° perspective rotated 180°

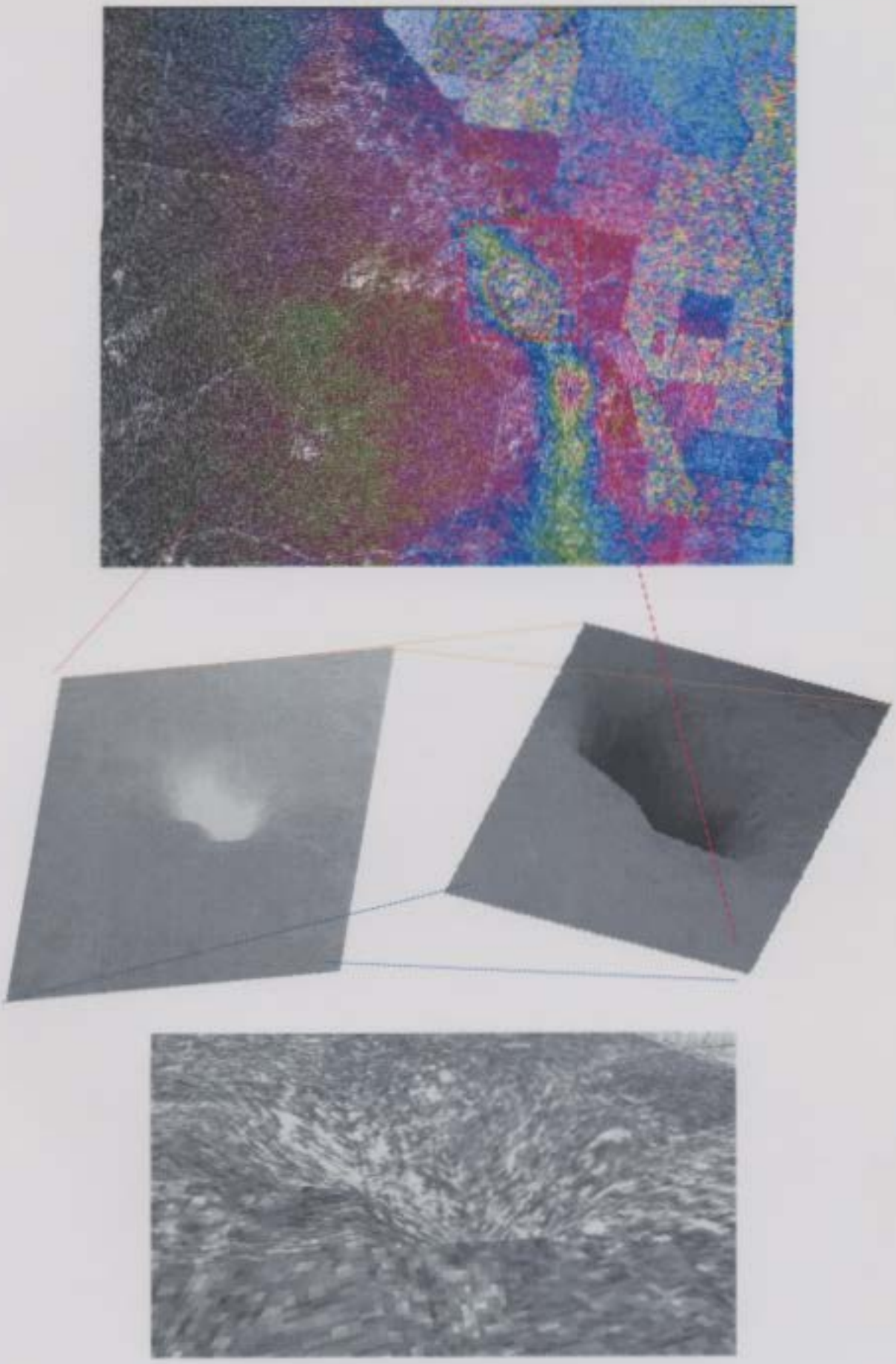

Figure B-4: 3-D subsidence as estimated by InSAR draped over SLC

Appendix C

- SAR & InSAR Processing Steps.

C. SAR & InSAR Processing Steps

Broadly, there are two main steps involved in SAR interferometry and differential interferometry. The first step is to process the raw SAR data using standard SAR processing techniques, which will be shortly discussed. The second step is the interferometric processing step. A SAR processor can be thought of as a realization of a signal compression technique in azimuth and range directions. The objective is to derive a high-resolution image from raw SAR data stored by the sensor after acquisition. In principle, a one-dimensional Fourier Transform (FT) is performed in the range direction and each range image line is multiplied by the FT of the reference function. After this, the inverse FT is taken to transform back to time domain and a range-focused image is formed, which is still defocused in azimuth. The same is done along the azimuth direction to obtain a fully focused single look complex (SLC) SAR image [31, 35]. To mathematically formalize the main steps involved for raw data processing of SAR images, azimuth and range processing are considered below.

C.1 Azimuth Processing

The received raw signal can be expressed as a function of time by

$$Z(t) = Ie^{j\varphi(t)} \tag{C-1}$$

where I is the energy of the return signal due to backscatter and $\varphi(t)$ is the received phase from the same scatterer at time t as defined in equation (2-4) in Chapter 2. In azimuth compression, multiple phase values of the same target points are adjusted to the same value of a reference function using coherent simulation [31]. This is achieved by correlating the return signal $Z(t)$ with a reference function $R(t)$ for a particular point target. The reference function is constructed such that it has the opposite phase of an ideal impulse response at every point.

$$R(t) = e^{-jkt^2} \tag{C-2}$$

where $k = \dfrac{2\pi v^2}{\lambda r_0}$ and was defined previously in equation (2-4) in chapter 2.

A weighting function $W(t)$ is used to limit the length of the reference function. In practice, this weighting function is a Kaiser-Bessel window. However, it could be any appropriate window function. For illustration, consider a rectangular window as the weighting function $W(t)$:

$$W(t) = 1 \text{ for } -\frac{t_{\max}}{2} < t < \frac{t_{\max}}{2}$$

$$W(t)=0 \text{ otherwise,}$$

where $t_{\max}$ is the illumination time and was previously defined in (chapter 2) equation (2-6). Then the reference function $R(t)$ can be expressed as

$$R(t) = W(t)e^{-jkt^2} \tag{C-3}$$

The resulting correlation of $Z(t)$ with $R(t)$ can be expressed as [5, 6, 36].

$$V(t)=\int_{-\infty}^{+\infty} Z(t)R(t+\xi)d\xi \tag{C-4}$$

$$V(t)=\int_{-\infty}^{+\infty} Ie^{jk\xi^2}e^{(-jk(t+\xi)^2)}W(t+\xi)d\xi \tag{C-5}$$

$$V(t)=Ie^{-jkt^2}\left[\int_{-\infty}^{+\infty} e^{-2jkt\xi}W(t+\xi)d\xi\right] \tag{C-6}$$

It is possible to approximate $W(t+\xi) \approx W(\xi)$ since only small times are important. Thus, the correlation result can be solved as in [5, 6 36]:

$$V(t)=Ie^{-jkt^2}\sqrt{2\pi}\int_{\frac{-t_{\max}}{2}}^{\frac{+t_{\max}}{2}} e^{-2jkt\xi}d\xi \tag{C-7}$$

$$V(t)=Ie^{-jkt^2}t_{\max}\sqrt{2\pi}\left[\frac{\sin(kt_{\max}t)}{kt_{\max}t}\right] \tag{C-8}$$

The result of this correlation is the image of a particular point target at location $Z(x,y)$.

C.2 Range Processing

The range direction is perpendicular to the flight path direction. To obtain a high-resolution image in range, short duration pulses, τ, are necessary. In general, SAR utilizes linear frequency modulation (chirp) to obtain high signal

bandwidth for better resolution and sufficient signal strength. The frequency $f(t)$ is given by

$$f(t) = \frac{B_r}{\tau} t \text{ for } -\frac{\tau}{2} < t < \frac{\tau}{2} \tag{C-9}$$

where B_r denotes the bandwidth of the emitted pulse. The chirp rate ς can be defined as

$$\varsigma = \frac{B_r \pi}{\tau} \tag{C-10}$$

To compress the signal, a new reference function is constructed similarly as described in Section C.1 for azimuth compression. Following the same steps, an expression can be derived [5, 6, 36] as

$$V_r(t) = I\tau\sqrt{2\pi}e^{jkt^2}\left[\frac{\sin(kt\tau)}{kt\tau}\right] \tag{C-11}$$

Equation (C-11) signifies the intensity distribution of a point-like target in the final SLC SAR image.

A typical SAR data processing step can now be formalized in the form of a flow chart as shown in Figure C-1. Note that the first step is to perform a FFT over all return signals of a single point scatter. The range compression step utilizes equation (C-11) over all range bins. Taking the inverse FFT of the compressed range signal will result in a focused range image and further followed by azimuth processing. Similarly, in the azimuth direction, azimuth compression is followed by inverse FFT whereby combining with the range IFFT produces a single look complex image. There are various other steps involved in

processing of SAR images and they depend on diverse sensor types. However, the basic recipe remains the same and is as shown in Figure C-1.

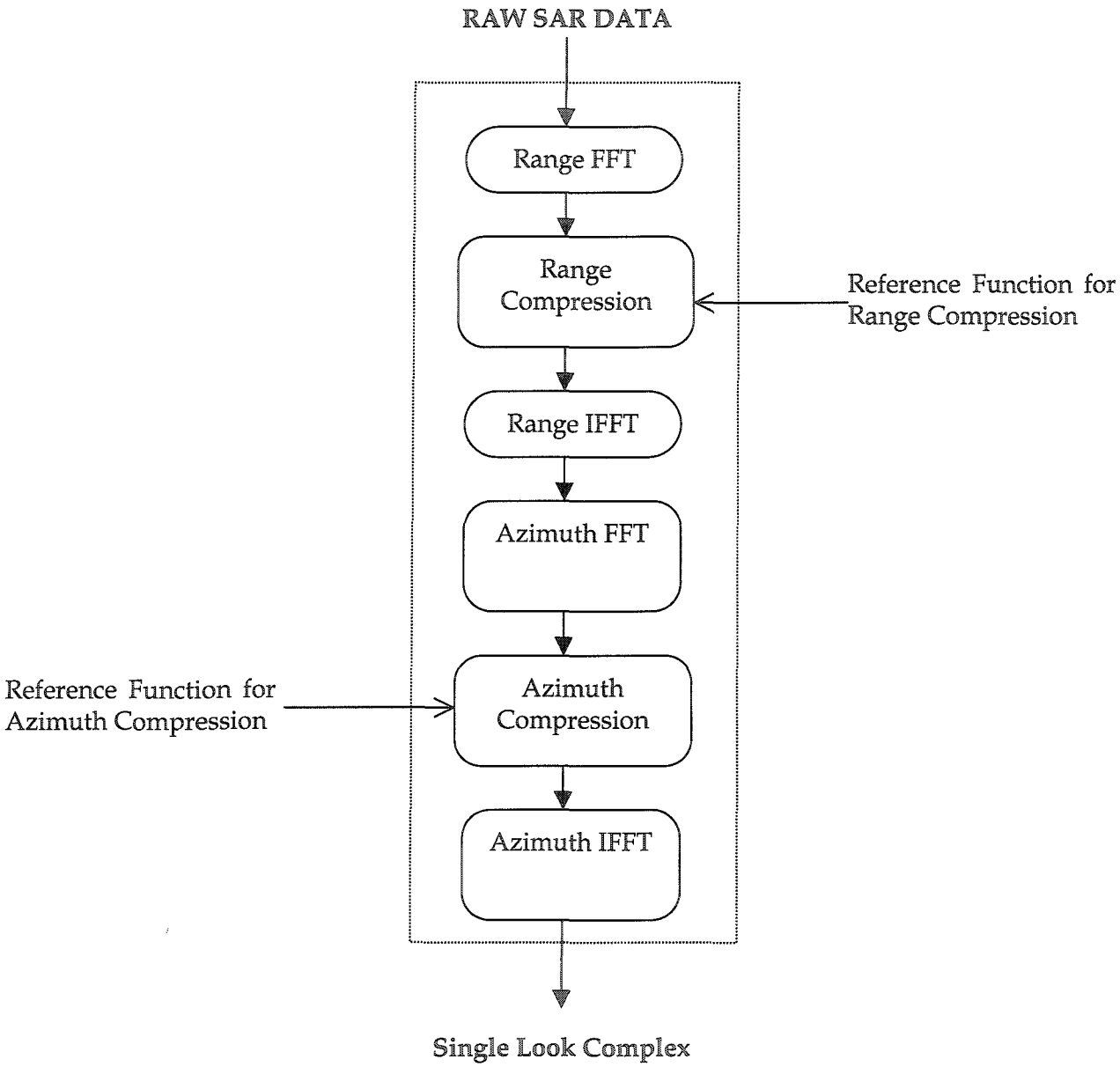

Figure C-1: Simple SAR raw data processing steps

C.3 Interferogram Processing

Figure C-2 details the processing steps required to combine the two SLC (single look complex) images (an interferometric pair) to generate an interferogram and a DEM.

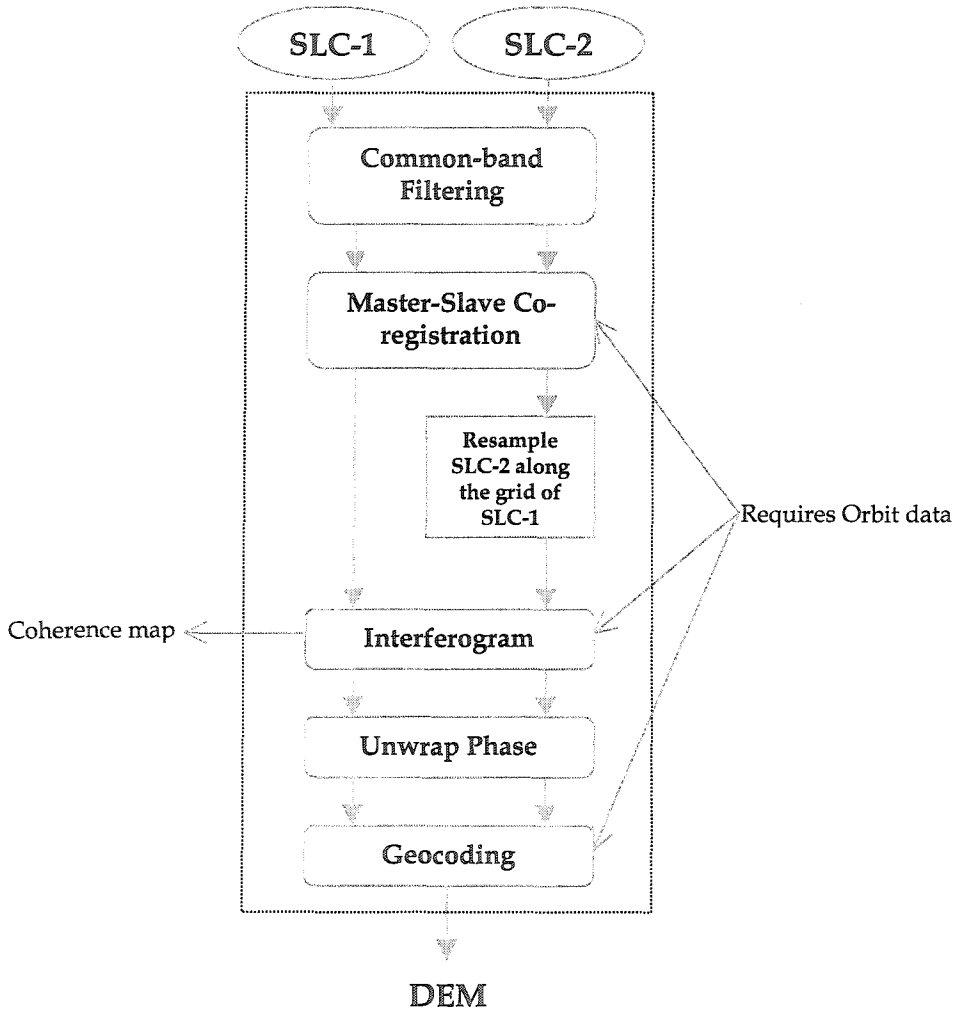

Figure C-2: Simple InSAR processing steps

The SLC images, when taken from slightly different geometries, will contain frequency regions that do not overlap. Common band filtering can eliminate this non-overlapping frequency band. Common band filtering of azimuth and range

spectra of the SLC pair optimizes interferometric correlation and minimizes the effects of the baseline geometry on the data pair [35]. After this, the image pair is co-registered to sub-pixel accuracy. Then, the second SLC (slave image) is re-sampled to the first SLC's (master image) grid. Now there are two images that are similar in geometry and contain the same overlapping information that is co-registered to a sub pixel level. An interferogram can now be computed using

$$Z_{\text{int}} = Z_1(x,y)Z_2^*(x,y). \tag{C-12}$$

The expected phase trend in the interferogram due to a smooth curved earth ellipsoid must be removed. This flattening operation is done using orbit information or state vectors coordinates. A flattened interferogram, also referred to as a normalized interferogram, is modulo 2π wrapped. As a consequence, the interpretation of interferometric phases must be preceded by phase unwrapping as detailed in Section 2.3.

The geocoding step embeds cartographic information onto the phase unwrapped interferogram, also referred to as a geocoded interferogram. This transforms the range-Doppler coordinate of the SAR to orthonormal map coordinates. The standard geocoding step requires the user to detect homologous points in a reference map and in the SLC. Using these ground control points, the image is then re-sampled to the geometry of a cartographic system. Geocoding requires experience and a considerable amount of familiarity with SAR images to identify suitable ground control points. A geocoded DEM is a perspective of the

terrain as visualized by the SAR. A SAR-derived DEM typically has height information of every latitude and longitude on the image grid.